

## ABSTRACT

Title of Dissertation: WAVE PROPAGATION IN TENSEGRITY  
AND PERIODIC STRUCTURES

Mohamed Salem Raafat,  
Doctor of Philosophy, 2017

Dissertation directed By: Professor Amr Baz,  
Department of Mechanical Engineering

This dissertation focuses on the development of the fundamental understanding of the dynamic behavior of assemblies of periodic arrays of tensegrity unit cells (along one and two directions). The ultimate aim of the dissertation is to capitalize on the attractive attributes of tensegrity structures with the unique characteristics of periodic structures, which stem from their ability to impede the propagation of disturbances that fall within certain frequency bands (known as *stop bands* or *bandgaps*). A successful implementation of such periodic/tensegrity structures is envisioned to extend the usefulness of tensegrity to vibration isolation problems, as well as to the synthesis of tunable acoustic and elastic wave filters, in both the frequency and spatial domains.

In this dissertation, numerical analysis of the statics and kinematics of icosahedron tensegrity cells are developed. The developed relationships are utilized to conceive one- and two-dimensional periodic arrays by appropriate stacking of icosahedron tensegrity cells. Alternative configurations for the periodic tensegrity arrays are considered for improved band gap characteristics, and a novel design for a periodic, tensegrity-based damper/vibration isolator is presented and demonstrated.

Particular emphasis is placed here on investigating and demonstrating some of the very interesting elastic properties of the periodic/tensegrity structures. Among these properties is the ratio of the bulk modulus to the shear modulus which are shown to be on the order of 1000. These values are two orders of magnitude higher than any naturally-occurring bulk material, suggesting that the viable potential of the periodic/tensegrity structures as suitable candidates for the synthesis of practical and realizable “*pentamode*” metamaterials, with many potential applications in the novel areas of acoustic and elastic cloaking where the proposed periodic/tensegrity structures act as liquids to ensure proper impedance matching.

**Keywords:** *icosahedron tensegrity cells, periodic/tensegrity cells, static and kinematic characteristics, the band gap characteristics, ratio of the bulk to the shear modulus*

WAVE PROPAGATION IN TENSEGRITY AND PERIODIC STRUCTURES

By

Mohamed Salem Raafat

Dissertation submitted to the Faculty of the Graduate School of the  
University of Maryland, College Park, in partial fulfillment  
of the requirements for the degree of  
Doctor of Philosophy  
2017

Advisory Committee:

Professor Amr Baz, Chair

Professor Balakumar Balachandran

Professor Miao Yu

Assistant Professor Siddhartha Das

Professor Norman Wereley (Dean's Representative)

© Copyright by  
Mohamed Salem Raafat  
2017

## **Acknowledgements**

I am infinitely grateful to my advisor, Professor Amr Baz, for his technical, professional and personal mentorship throughout this PhD journey. Leading by example through his work ethic, passion for research, teaching and learning, the latitude he grants his students and his genuine care for their development and well-being – I could not have asked for a better advisor, and I hope one day to be able to pass along to others what he has instilled in me.

I am thankful to my committee members for contributing directly to this work through insightful comments, suggestions and discussions, and indirectly through their students' work which often opened new horizons for me. I also benefited greatly from input from students and alumni of the Smart Materials and Structures Research Center (Mostafa Nouh, Jason Smoker, Yaser Alsaffar, Yaqoub Abdullah, Andrew Roshwalb, Dr. Mustafa Arafa and Dr. Wael Akl), and the undergraduate students I have supervised. More thanks are due to Mr. Majid Aroom and the machine shop staff for his time, effort and invariably constructive input, and to the Research Prototyping Lab (Caroline McCue, Nathan Young and John Fraser) for 3D printing help.

I am also grateful to the leadership, faculty and staff of the Mechanical Engineering department at UMD, as well as the ME Graduate Office and ME IT for creating and sustaining an efficient, cohesive and stress-free environment enabling us to focus on our work and academic advancement while fostering our sense of collegiality and belonging.

On the home front, I am eternally grateful to my parents and siblings, whom I could never thank enough, for their unrelenting support which has propelled thus far and keeps me going. I am thankful to my wife, (Dr.) Azza, who has been my companion for the bigger part of this journey, making it more enjoyable and making me look forward to the next one.

# Table of Contents

Acknowledgements.....	ii
Table of Contents .....	iv
List of Figures .....	vii
List of Symbols .....	ix
Chapter 1: Introduction .....	1
1.1 Overview .....	1
1.2 Scope of this Dissertation.....	2
1.3 Organization of the Dissertation .....	3
1.4 Summary .....	4
Chapter 2: Literature Review .....	5
2.1 Tensegrity Structures.....	5
2.1.1 Origins and Historical Perspective.....	5
2.1.2 Tensegrity Definition .....	8
2.1.3 Tensegrity Literature Survey .....	10
2.2 Periodic Structures .....	15
2.3 Summary .....	22
Chapter 3: Static and Kinematic Analysis of Icosahedron Tensegrity .....	23
3.1 Introduction .....	23
3.2 Unit Cell Description and Material Properties .....	23
3.3 Static and Kinematic Analysis of the Unit Cell .....	25
3.3.1 Overview of the Procedure .....	25
3.3.2 Analysis of the Icosahedron Tensegrity.....	28
3.4 Mechanical Properties of the Unit Cell.....	31
3.5 Tensegrity Prototype .....	36
3.6 Experimental Determination of Cell's Constants .....	37
3.6.1 Shear Modulus .....	37
3.6.2 Elastic Modulus .....	39
3.6.3 Analysis and Discussion .....	42
3.7 Summary .....	44

Chapter 4: Static and Dynamic Analysis of Periodic Icosahedron Tensegrity Structures	45
4.1 Introduction	45
4.2 One-dimensional Periodic Arrays	45
4.2.1 Configuration of the Periodic Array	45
4.2.2 Mechanisms and States of Self-stress	46
4.3 Static Analysis	48
4.4 Dynamic Analysis of 1D Tensegrity Array	51
4.4.1 Overview of Bloch's Theorem	51
4.4.2 Pass and Stop Bands of 1D Tensegrity Lattice	56
4.5 Experimental Verification	57
4.5.1 Prototype Description	57
4.5.2 Determination of Shear Modulus	58
4.5.3 Determination of Elastic Modulus	60
4.5.4 Impedance Tube Testing	62
4.6 Icosahedron Tensegrity Beams	65
4.6.1 Description	65
4.6.2 Mechanisms and States of Self-stress	66
4.6.3 Bending Stiffness of the Beam	66
4.7 Two-dimensional Icosahedron Tensegrity Arrays	68
4.7.1 Configuration and Description	68
4.7.2 Mechanisms and States of Self-stress	68
4.7.3 Static Analysis	69
4.8 Dynamic Analysis	72
4.9 Alternating Tensegrity Array	75
4.10 Summary	77
Chapter 5: Alternative Design for Periodic Icosahedron Tensegrity Arrays	78
5.1 Introduction	78
5.2 Description of the Unit Cell and Periodic Array	78
5.3 One-dimensional Array of Alternating Cells	80
5.3.1 Geometry and Material Properties	80
5.3.2 Mechanisms and Stats of Self-stress	81
5.3.3 Static Analysis	82

5.4	Dynamic Analysis .....	85
5.4.1	The Effect of Pre-stress.....	87
5.4.2	The Effect of Connecting Strings' Stiffness .....	88
5.5	Two-Dimensional Arrays.....	90
5.5.1	Description.....	90
5.5.2	Mechanisms and States of Self-stress .....	91
5.5.3	Static Analysis .....	91
5.5.4	Dynamic Analysis of 2D Array .....	97
5.6	Summary .....	102
Chapter 6: Design and Testing of Tensegrity Damper .....		103
6.1	Introduction .....	103
6.2	Description .....	103
6.3	Derivation of Equations of Motion .....	104
6.4	Comparison of Linear and Nonlinear Equations of Motion.....	109
6.5	Modeling Viscoelastic Flexible Elements.....	112
6.6	Steady-state Response to Harmonic Excitation .....	116
6.7	Bloch Analysis of the Periodic Structure .....	117
6.8	Prototyping and Testing .....	119
6.8.1	Design and Assembly .....	119
6.8.2	Material Characterization and Selection.....	121
6.8.3	GHM Model Parameters .....	125
6.9	Unit Cell Testing and Characterization.....	126
6.10	Vibration Testing of Periodic Array.....	129
6.11	Summary.....	133
Chapter 7: Original Contributions and Future Work .....		134
7.1	Overview .....	134
7.2	Major Contributions of the Dissertation .....	134
7.3	Future Work .....	136
Appendix A: Equilibrium Matrix of Icosahedron Tensegrity.....		138
Appendix B: Finite Element Formulation of Pre-stressed Bar and Tendon Elements ..		139
Appendix C: Derivation of Equations of Motion for Tensegrity Damper Unit Cell .....		140
Bibliography .....		146



## List of Figures

Figure 1.1 Icosahedron tensegrity .....	1
Figure 1.2 Multi-plane, high and stable shear deformations of icosahedron tensegrity .....	2
Figure 2.1 The Needle Tower by Kenneth Snelson in Washington, D.C. ....	5
Figure 2.2 The X-piece tensegrity by Kenneth Snelson [7].....	6
Figure 3.1 Icosahedron tensegrity .....	24
Figure 3.2 Stiffening effect of pre-stress .....	31
Figure 3.3 Unit cell with three end-plates.....	32
Figure 3.4 Elastic coefficients of icosahedron tensegrity .....	35
Figure 3.5 Bulk-to-shear ratio of icosahedron tensegrity .....	35
Figure 3.6 3D-printed icosahedron tensegrity .....	36
Figure 3.7 Shear testing of tensegrity cell .....	37
Figure 3.8 Sensors' output – unit cell in shear.....	38
Figure 3.9 Experimental force-displacement (cell in shear).....	39
Figure 3.10 Compression testing of tensegrity cell .....	40
Figure 3.11 Sensors' output –unit cell in compression.....	41
Figure 3.12 Experimental force-displacement (cell in compression) .....	41
Figure 4.1 1D, class-2 array of identical icosahedron tensegrity cells .....	46
Figure 4.2 Elastic modulus of 1D, class-2 tensegrity array of repeating cells.....	49
Figure 4.3 Shear modulus of 1D, class-2 tensegrity array of repeating cells .....	50
Figure 4.4 Bulk modulus of 1D, class-2 tensegrity array of repeating cells.....	50
Figure 4.5 Bulk-to-shear ratio of 1D, class-2 tensegrity array of repeating cells.....	51
Figure 4.6 (a) Lengthwise section of periodic beam and (b) unit cell .....	52
Figure 4.7 Dispersion curves of 1D, class-2 tensegrity array of repeating cells .....	57
Figure 4.8 Icosahedon 1D array.....	57
Figure 4.9 Array shear test setup .....	58
Figure 4.10 Shear force against displacement – 1D array .....	59
Figure 4.11 Array compression test setup. Front and top views.....	60
Figure 4.12 Compression test – sensors' output .....	61
Figure 4.13 Compression test – Force against deformation .....	62
Figure 4.14 Schematic drawing of acoustic test setup.....	63
Figure 4.15 Tensegrity array in impedance tube .....	63
Figure 4.16 Transmission coefficient of tensegrity array .....	64
Figure 4.17 Inter-cell connectivity strings of tensegrity beam .....	65
Figure 4.18 Bending stiffness of tensegrity beam ( $K_c = 5,000 \text{ N/m}$ ).....	67
Figure 4.19 Bending stiffness of tensegrity beam ( $K_c = 20,000 \text{ N/m}$ ).....	67
Figure 4.20 Elastic moduli of 2D, class-2 tensegrity array of repeating cells .....	70
Figure 4.21 Shear modulus, $G_{zx}$ , of 2D, class-2 tensegrity array of repeating cells.....	71
Figure 4.22 Shear modulus, $G_{zy}$ , of 2D, class-2 tensegrity array of repeating cells.....	71
Figure 4.23 Dispersion surfaces of 2D, class-2 tensegrity array of repeating cells.....	74
Figure 4.24 1D, class-2 tensegrity array of alternating cells .....	75

Figure 4.25 Top view of 2D, class-2 tensegrity array of alternating cells.....	76
Figure 4.26 Dispersion surfaces of 2D, class-2 tensegrity array of alternating cells.....	76
Figure 5.1 Inter-cell connectivity for 1D, class-1 tensegrity array.....	80
Figure 5.2 Elastic modulus of 1D, class-1 tensegrity array.....	83
Figure 5.3 Shear modulus of 1D, class-1 tensegrity array.....	83
Figure 5.4 Bulk modulus of 1D, class-1 tensegrity array.....	84
Figure 5.5 Bulk-to-shear ratio of 1D, class-1 tensegrity array.....	84
Figure 5.6 Unit cell for Bloch analysis of 1D, class-1 tensegrity array.....	85
Figure 5.7 Dispersion curves for 1D, class-1 tensegrity array ( $K_c = 5000 \text{ N/m}$ ).....	86
Figure 5.8 Frequency response of 1D, class-1 tensegrity array ( $K_c = 5000 \text{ N/m}$ ).....	87
Figure 5.9 Effect of pre-stress on stop bands ( $K_c = 5000 \text{ N/m}$ ).....	88
Figure 5.10 Dispersion curves for 1D, class-1 tensegrity array ( $K_c = 1000 \text{ N/m}$ ).....	89
Figure 5.11 Frequency response for 1D, class-1 tensegrity array ( $K_c = 1000 \text{ N/m}$ ).....	89
Figure 5.12 Top view of 2D, class-1 tensegrity array.....	90
Figure 5.13 Elastic modulus $E_{xx}$ of 2D, class-1 tensegrity array.....	93
Figure 5.14 Elastic modulus $E_{yy}$ of 2D, class-1 tensegrity array.....	93
Figure 5.15 Shear modulus $G_{zx}$ of 2D, class-1 tensegrity array.....	94
Figure 5.16 Shear modulus $G_{zy}$ of 2D, class-1 tensegrity array.....	95
Figure 5.17 Bulk modulus of 2D, class-1 tensegrity array.....	96
Figure 5.18 Unit cell for Bloch analysis of 2D class-1 tensegrity array.....	98
Figure 5.19 Layout of the 2D array.....	98
Figure 5.20 Dispersion surfaces of 2D, class-1 tensegrity array.....	99
Figure 5.21 Effect of pre-stress on pass and stop bands.....	100
Figure 5.22 Frequency response of 2D, class-1 tensegrity array.....	101
Figure 6.1 Schematic of periodic tensegrity damper.....	103
Figure 6.2 Tensegrity damper unit cell.....	104
Figure 6.3 Representative flexible element.....	105
Figure 6.4 Linear vs nonlinear forced response of tensegrity damper unit cell.....	110
Figure 6.5 CAD model of tensegrity isolator cell.....	120
Figure 6.6 Viscoelastic sample mounted in DMTA holder.....	122
Figure 6.7 Storage modulus of rubber-like materials.....	123
Figure 6.8 Loss modulus of rubber-like materials.....	123
Figure 6.9 Storage modulus of rigid material.....	124
Figure 6.10 Storage modulus and loss factor – GHM model vs experiment.....	126
Figure 6.11 Tensegrity damper prototype on UTM machine.....	127
Figure 6.12 Experimental and predicted force-deflection plot.....	128
Figure 6.13 Periodic tensegrity damper vibration test rig.....	130
Figure 6.14 Experimental transmissibility of tensegrity damper array.....	130
Figure 6.15 Dispersion curves for periodic tensegrity damper.....	132
Figure 6.16 Finite element simulation.....	132

## List of Symbols

<b>A</b>	Equilibrium matrix	[m]
$A_n$	Cross-section area on which normal force acts	[m <sup>2</sup> ]
$A_{sh}$	Cross-section area on which shear force acts	[m <sup>2</sup> ]
$B$	Bulk modulus of structure	[N/m <sup>2</sup> ]
$E$	Modulus of elasticity of structure	[N/m <sup>2</sup> ]
$E'$	Storage modulus	[N/m <sup>2</sup> ]
$E''$	Loss modulus	[N/m <sup>2</sup> ]
$E_0$	Storage modulus at $\omega = 0$	[N/m <sup>2</sup> ]
$E_b$	Modulus of elasticity of bar	[N/m <sup>2</sup> ]
$e$	Vector of members' elongation coefficients	[m <sup>2</sup> ]
$\hat{e}_x, \hat{e}_y, \hat{e}_z$	Unit vector along each of the global axes	
$\vec{e}_1, \vec{e}_2$	Direct lattice vectors	[m]
$\vec{e}_1^*, \vec{e}_2^*$	Reciprocal lattice vectors	[m <sup>-1</sup> ]
<b>F</b>	Vector of nodal forces	[N]
$F_b$	Total bending force applied on a structure	[N]
$F_n$	Total normal force applied on a structure	[N]
$F_{sh}$	Total shear force applied on a structure	[N]
$f_b$	Pre-load force density in bar	[N/m]
$f_s$	Pre-load force density in internal string	[N/m]
$G$	Shear modulus of structure	[N/m <sup>2</sup> ]
<b>H</b>	Kinematic matrix	[m]
<b>I</b>	Identity matrix	
$i$	$\sqrt{-1}$	
<b>K</b>	Stiffness matrix of structure	[N/m]
$\tilde{\mathbf{K}}, K^P$	Periodic stiffness matrix	[N/m]
$K_b$	Bending stiffness	[N/m]
$K_c, K_{c1}, K_{c2}$	Stiffness of connecting string	[N/m]
$K_s$	Stiffness of internal string	[N/m]
$\vec{k}$	Wave vector	[m <sup>-1</sup> ]
$k_1, k_2$	Components of wave vector	
$l_b$	Length of bar	[m]
$l_c, l_{c1}, l_{c2}$	Length of connecting string	[m]
$l_s$	Length of internal string	[m]
<b>M</b>	Mass matrix of structure	[kg]

$\mathbf{M}_1$	Vector of nodal displacements corresponding to inextensional mechanism	[m]
$\tilde{\mathbf{M}}, M^P$	Periodic mass matrix	[N/m]
$N$	Number of cells in an array	
$N_X, N_Y, N_Z$	Number of cells along each of the global axes for an array	
$N_1, N_2$	Number of cells separating a target cell from a reference cell, along $\vec{\mathbf{e}}_1$ and $\vec{\mathbf{e}}_2$ , respectively	
$n_{ss}$	Number of states of self-stress	
$\mathbf{q}$	Vector of nodal degrees of freedom	[m]
$\mathbf{q}_i$	Vector of nodal degrees of freedom of node $i$	[m]
$\mathbf{q}^R$	Vector of reduced nodal degrees of freedom	[m]
$\vec{\mathbf{R}}$	Position vector of a point in an array of cells	[m]
$\vec{\mathbf{r}}$	Position vector of a point local to a cell	[m]
$r_b$	Cross-section radius of bar	[m]
$r_c, r_{c1}, r_{c2}$	Cross-section radius of connecting string	[m]
$r_s$	Cross-section radius of internal string	[m]
$\mathbf{S}_1$	Vector of member loading corresponding to state of self-stress	[N/m]
$s$	Laplace operator	
$\mathbf{T}$	Transformation matrix	
$T_i$	Kinetic energy of element $i$	[J]
$T_0$	Initial tension in string	[N]
$\mathbf{t}$	Force density vector	[N/m]
$t$	Time	[s]
$V$	Initial volume of a structure	[m <sup>3</sup> ]
$V_i$	Potential energy of element $i$	[J]
$W$	Wave function	
$W_0$	Wave amplitude	[m]
$w_i$	Vertical displacement of node $i$	[m]
$x_i, y_i, z_i$	Degrees of freedom of node $i$ in global coordinates	[m]
$\alpha, \alpha_1, \alpha_2$	Attenuation constant	
$\beta, \beta_1, \beta_2$	Phase constant	
$\Delta_b$	Bending deflection of structure	[m]
$\Delta e$	Inter-cell offset	[m]
$\Delta_n$	Overall elongation of structure under normal loading	[m]
$\Delta_{sh}$	Shear displacement imposed on a structure	[m]
$\Delta P$	Hydrostatic pressure applied on a structure	[N/m <sup>2</sup> ]
$\Delta V$	Change in volume of a structure	[m <sup>3</sup> ]
$\Delta_0$	Initial string extension	[m]

$\delta_{ij}$	Kronecker delta	
$\varepsilon_0$	Initial elastic strain in string	
$\eta$	Loss factor	
$\theta_i$	Angular rotation at node $i$	[rad]
$\mu, \mu_1, \mu_2$	Propagation constant	
$\mathbf{E}$	Augmented force vector	[N]
$\rho_b$	Density of bar	[kg/m <sup>3</sup> ]
$\omega$	Angular velocity	[rad/s]

# Chapter 1: Introduction

## 1.1 Overview

Since their invention in the middle of the twentieth century, tensegrity structures as shown in Figure 1.1 have been thoroughly researched and their use as deployable structures, structural elements, and mobile robots has been explored and demonstrated. Compared to more conventional structures, they have the advantage of being lighter, foldable, reconfigurable, and easier to model and control.

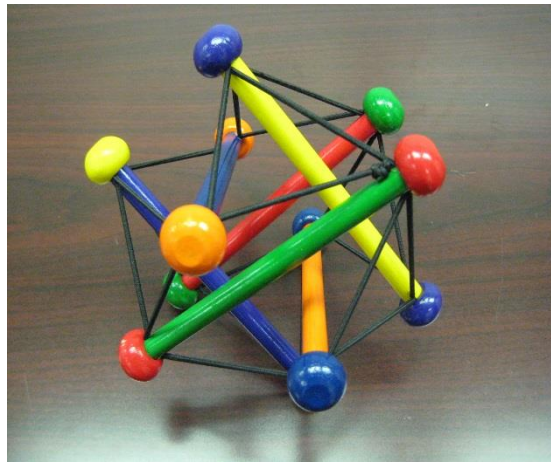


Figure 1.1 Icosahedron tensegrity

In this dissertation, we propose periodic arrays conceived by tessellating a simple tensegrity unit cell (along one and two directions) with the aim of combining the aforementioned attributes with an important characteristic of periodic structures, namely their ability to impede the propagation of disturbances that fall within certain frequency bands (known as *stop bands* or *bandgaps*). A successful implementation of such periodic tensegrity structures would extend the usefulness of tensegrity to vibration isolation

problems, as well as to the synthesis of tunable acoustic and elastic wave filters, in both the frequency and spatial domains.

Moreover, some of the periodic structures we consider exhibit some very interesting elastic properties, namely the ratio of their bulk modulus to their shear modulus is on the order of 1000, two orders of magnitude higher than any naturally-occurring bulk material, suggesting that they may be suitable candidates for the synthesis of pentamode metamaterials, with many potential applications in the novel areas of acoustic and elastic cloaking. Such unique characteristics can be seen clearly in Figure 1.2.

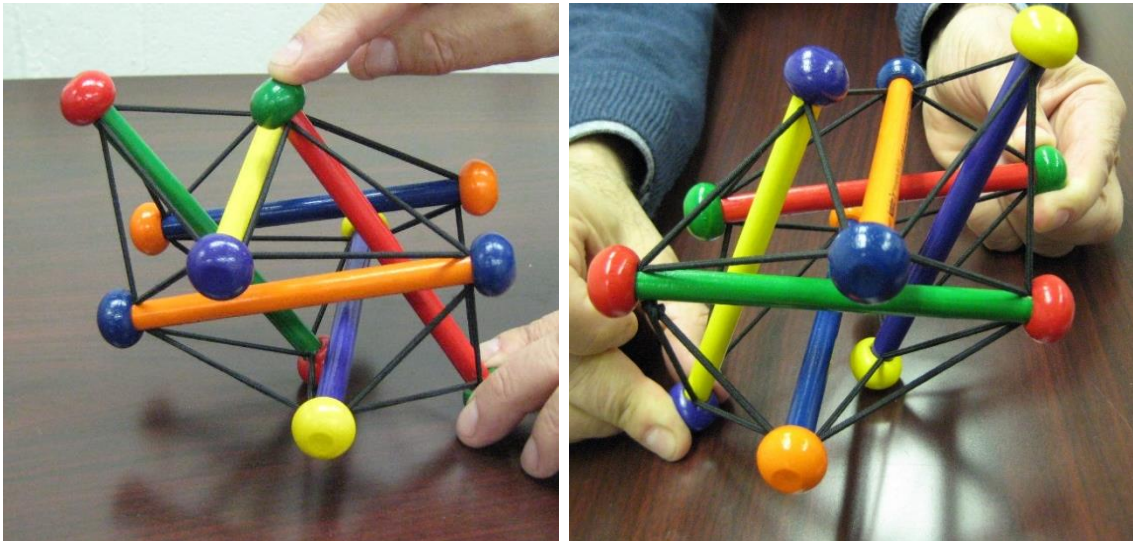


Figure 1.2 Multi-plane, high and stable shear deformations of icosahedron tensegrity

## 1.2 Scope of this Dissertation

In this dissertation, numerical analysis of the statics and kinematics of icosahedron tensegrity cells are developed. The developed relationships are utilized to conceive one- and two-dimensional periodic arrays by appropriate stacking icosahedron tensegrity cells. Alternative configurations for the periodic tensegrity arrays are considered for improved

band gap characteristics, and some of the conceived designs are manufactured using multi-material 3D printing, and the resulting tensegrity cells and arrays are experimentally tested to investigate and verify the predicted static and dynamic characteristics.

A new design for a periodic, tensegrity-based damper/vibration isolator is proposed, capitalizing on the periodicity to attenuate vibrations in the stop bands. The proposed design is 3D-printed and static and dynamic characterization experiments are carried out.

Particular emphasis is placed here on investigating and demonstrating some of the very interesting elastic properties of the periodic/tensegrity structures. Among these is the very high ratio of the bulk modulus to the shear modulus which is shown to be on the order of 1000, approximating the behavior of liquids.

### **1.3 Organization of the Dissertation**

In chapter 2 of this dissertation, we survey the available literature on the topics of tensegrity and periodic structures, along with a brief historical perspective. In Chapter 3 we perform a numerical analysis of the statics and kinematics of the tensegrity building block we consider in this dissertation – the icosahedron tensegrity, followed by prototyping and testing of the tensegrity. In Chapter 4, we conceive one- and two-dimensional periodic arrays by stacking icosahedron tensegrity cells together, numerically investigate their static and dynamic characteristics, and prototype and test a one-dimensional array. In Chapter 5, we propose an alternative configuration for the periodic tensegrity arrays, and numerically investigate their static and dynamic characteristics. In Chapter 6, we propose and test a novel design for a periodic, tensegrity-based damper, developing the equations of motions



and mathematical model, then building the prototype, perform material characterization and device testing. Chapter 7 summarizes the major contributions of this dissertation and proposes future research directions.

#### **1.4 Summary**

This chapter has presented a brief overview of the scope and organization of this dissertation with particular emphasis on the development of the fundamentals governing the operation of periodic/tensegrity structures in an attempt to investigate the effect of the topology of these structures on their wave propagation and mechanical filtering characteristics.

## Chapter 2: Literature Review

In this chapter, we survey the existing literature on tensegrity structures and periodic structures.

### 2.1 Tensegrity Structures

#### 2.1.1 Origins and Historical Perspective

The word “Tensegrity” was coined by architect and inventor Richard Buckminster Fuller [1] as a contraction of the expression “Tensional Integrity” to describe a class of structures that combine continuous tensile elements and discontinuous compressive elements, and which exist in a state of stable equilibrium without any external forces. Figure 2.1 shows a large-scale example of tensegrity – the needle tower in Washington, D.C. by artist Kenneth Snelson.



Figure 2.1 The Needle Tower by Kenneth Snelson in Washington, D.C.

The structures themselves, however, predate the term and some controversy has persisted over the years over who should be credited with their invention. The first tensegrity is now believed [2, 3] to have been created as a work of art by Latvian artist Karl Ioganson around 1920 and was displayed in an exhibition in Moscow in 1921, with photographs of the structure later reported in [4]. The structure “consists of three bars and seven cables and is handled by means of an eighth unstressed cable, the whole being deformable” [2, 5].

In the United States, and with no obvious connection to Ioganson’s earlier work, Fuller reports in the mid 1940’s [6] to have been thinking about the interplay between compressive and tensile elements in Nature and the potential of using this duality in man-made structures. However it was not until 1948 that artist Kenneth Snelson, then Fuller’s student at Black Mountain College in North Carolina, actually created the first tensegrity (the “X-piece”, shown in Figure 2.2) which conformed to Fuller’s idea of *Energetic-Synergetic Geometry* [1, 7].



Figure 2.2 The X-piece tensegrity by Kenneth Snelson [7]

In the years that followed, both Snelson and Fuller proceeded to design and create their own tensegrity structures, Snelson primarily focusing on their artistic value [8] and Fuller exploring their potential use as structural building blocks [9]. An exhibition at the New York Museum of Modern Arts in 1959 showcased Fuller's 36-foot high *Tensegrity Mast* and other works, and dedicated a (much smaller) display for Snelson to display his own tensegrity designs. The museum credited the latter with discovering the principle on which Fuller's *Mast* was based, while also acknowledging the role of Fuller's theories in leading to this discovery [10]. While Fuller himself initially recognized Snelson as the inventor of the first tensegrity [1, 11], he later dropped any mention to Snelson from his works and maintained that all his own earlier works dating back to 1927 were in fact tensegrity structures [10].

In the late 1950's and early 1960's, several patent applications about tensegrity structures were filed almost simultaneously by Fuller [12], David Emmerich in France [13], and Snelson [14]. Each of these first three patents described the same basic structure built from three compressive elements and nine tensile elements, and all emphasized the continuity of tensile elements and discontinuity of compressive elements. Despite the similarity between the patents, it is worth mentioning that Emmerich – who was influenced by Ioganson's earlier work [2, 15] – is perhaps the most explicit in his patent about the self-tensioning property of the structure's elements as a condition for its equilibrium.

Authorship controversy aside, many researchers today [5, 16] agree that all three men contributed greatly to the discovery and development of tensegrity. And if lines must be drawn, Fuller may be credited with being a visionary and a promoter of the concept of tensegrity, Snelson with bringing Fuller's theories and ideas to life with his original

creations, and Emmerich of being a pioneer in his own right and the first experimentalist in this area.

### **2.1.2 Tensegrity Definition**

While Fuller did not formally define what a tensegrity is, his writings and patent refer to structures with discontinuous compression and continuous tension, or “islands of compression in a sea of tension”. The first widely accepted definition of a tensegrity was thus given by Pugh in 1978 [17] to describe Fuller’s structures: “A Tensegrity system is established when a set of discontinuous compressive components interacts with a set of continuous tensile components to define a stable volume in space”.

After rigorous analysis of Fuller’s tensegrity structures, Calladine [18], Tarnai [19], Pellegrino [20], and Hanaor [21] observed that they were a class of pre-stressable structures that were statically and kinematically indeterminate. The kinematic indeterminacy manifests itself in the form of ‘infinitesimal mechanisms’ – mechanisms that cause small changes in the lengths of the members, which are on second or higher order of the nodal displacements – which get stiffened as a result of the pre-stress.

Motro in 1992 [15] synthesized a new definition which emphasized self-stress as a condition for stiffness, while doing away with the discontinuity of compression elements: “Tensegrity systems are systems whose rigidity is the result of a state of selfstressed equilibrium between cables under tension and compression elements and independent of all fields of action”. However, in a new definition in 2003 [5], he re-affirms the discontinuity of compression elements and does not require pre-stress as a condition for stiffness: “A tensegrity system is a system in a stable self-equilibrated state comprising a

discontinuous set of compressed components inside a continuum of tensioned components”.

Meanwhile, Skelton and his collaborators (*e.g.*, [16, 22, 23]) have generally viewed tensegrities as pre-stressed stable connections of compression and tension elements, where the tension elements are necessary to stabilize the structure. Their work has expanded the definition of a tensegrity in two ways: first, they include structures that do not feature any mechanisms, *e.g.*, [16, 23]. These are statically indeterminate but kinematically determinate structures, which were also considered by [24-26]. Second, they define a *Class k* tensegrity as a tensegrity that has at most  $k$  compression elements connected at each node. Therefore *class 1* tensegrities would include the structures conceived by Fuller and others where the compression elements are discontinuous within a continuum of tensile elements, while tensegrities of class 2 or higher would allow at least some degree of continuity of the compression elements.

Based on the differing views presented above, we can see that there are some aspects of the definition of a tensegrity on which there is a consensus, namely that they are reticulated structures where elements are uniquely loaded in tension or in compression. Tension elements cannot sustain compression, while compression elements can sustain both tension and compression but are only loaded in compression. The structures possess one or more states of self-stress, and they exist in a state of stable equilibrium in the absence of external forces. In our view, requiring the discontinuity of compression elements or the presence of infinitesimal mechanisms that get stiffened by pre-stress is unnecessarily restrictive.

### 2.1.3 Tensegrity Literature Survey

For the first thirty years of their existence, tensegrity structures were viewed as works of art and objects of mechanical and structural curiosity. It was Calladine in 1978 [18] who performed the first rigorous analysis of their kinematics and statics. He analyzed Fuller's 6-bar, 18-tendon tensegrity in light of Maxwell's rule for the stiffness of structures [27], and noted that while the tensegrity had fewer elements than necessary for stiffness according to Maxwell, expecting it to be "loose" due to the presence of mechanisms; it was nonetheless a stable structure. He showed that the tensegrity fits under an exception to the rule – which Maxwell himself had predicted – wherein the geometry and the configuration of the structure ensure that the resulting mechanisms (six in this case) are infinitesimal and that at least one state of self-stress (static indeterminacy) exists which endows the structure with a first-order stiffness (a stiffness on the order of the pre-stress).

Probing further, Tarnai [19] investigated the nature of the structures' mechanisms and the conditions under which the pre-stress will stiffen a structure. Pellegrino and Calladine [20, 28] then followed by developing a matrix approach to analyze a general pin-jointed structure from a kinematic and static determinacy viewpoint, enumerating the mechanisms and states of self-stress that it may possess, and – using a 'product-force vector' method – determine whether the state(s) of self-stress would impart stiffness to the mechanism(s) and therefore result in a stable structure.

Oppenheim and Williams [29] derived the nonlinear force-displacement relationship arising from geometric stiffening in a tensegrity subject to pre-stress. They concluded that the pre-stressed structures are quite soft in the vicinity of their equilibrium configurations, with the stiffness increasing dramatically with finite, small displacements.

Guest [30, 31] and Skelton [16] studied the stiffness of tensegrity using the a *stress matrix* formulation to derive the tangent stiffness matrix of tensegrity, which decomposes into two components: a linear stiffness matrix derived from small deformations of the elements, and a geometrical stiffness matrix induced by the pre-stress.

A significant body of literature has been devoted to the problem of form-finding for tensegrity structures, *i.e.*, finding an equilibrium configuration and the corresponding member forces for a given set of elements, or conversely, coming up with design requirements that satisfy some desired equilibrium configuration. Tibert and Pellegrino [32], and later Juan and Mirats-Tur [33], provide detailed surveys of previous form-finding methods and classify them into two categories: kinematical methods, *e.g.*, [34-36], and statical methods, *e.g.*, [37-39]. More recently, several new approaches have been developed to tackle the form-finding problem, *e.g.*, using finite element [40], Monte Carlo method [41], and genetic algorithms [42, 43].

With the aim of designing efficient structures, de Jager and Skelton [23] optimize the stiffness and stiffness-to-mass ratio of planar tensegrity truss structures by varying the topology, geometry, and material distribution of the structure, using symbolic expressions for the stiffness that they derived in [44]. Masic *et al.* [45] follow a numerical approach to tackle the same optimization problem, while imposing shape, boundary conditions, strength and buckling constraints.

The investigation of tensegrity dynamics began with Motro *et al.* [46] who derived a static and dynamic linear analytical model for the “simplex” tensegrity (three struts and nine cables) and built an experimental setup to test their model. Tests showed very good agreement between theory and experiments. Furuya [47] performed a finite element



analysis of the vibration characteristics of tensegrity masts and studied the effect of initial tension on the natural frequencies of the structures.

In a two-part paper, Murakami [26, 48] derived the nonlinear equations of motion for tensegrity structures. He linearized the equations around a pre-stressed equilibrium configuration in order to perform a finite element harmonic modal analysis and to investigate the equilibrium and stiffness of the pre-stressed structures. Independently, Oppenheim and Williams [49, 50] derived the nonlinear equations of motion for a simple tensegrity structure incorporating damping along the cables and conducted vibration experiments and numerical simulations. Concerned with damping, they observed that the decay of vibration amplitude occurs at a much slower rate than would be expected with linear damping, which would make the structures unsuitable for applications. However, they also noted that by introducing linear damping at the joints, the equations of motion became linearly damped and vibrations decayed exponentially with time.

Sultan [39] and Sultan *et al.* [51] developed nonlinear dynamic models for multi-layer tensegrity structures, then proceeded to linearize the equations of motion around equilibrium configurations to obtain linear models and investigated the resulting mass, stiffness, and damping matrices. Skelton *et al.* [52] developed a nonlinear dynamic model for a large tensegrity shell structure, and later in [53], Skelton generalized the work to any tensegrity and used matrix differential equations to express the dynamics of the problem.

In a series of paper, Arsenault and Gosselin [54-56] analyzed the kinematics, statics, and dynamics of planar tensegrity modules with one, two and three degrees of freedom, respectively, and made the observation that under certain configurations the overall stiffness of the tensegrity becomes negative.

In the area of control, Djouadi *et al.* [25] simulated an optimal control algorithm to control the oscillations of a cantilever tensegrity structure by altering the pre-tension in the cables. Sultan and Skelton [57] integrate the control system design problem with the structural design of the tensegrity by simultaneously considering the static design, linearized dynamic equations, actuator locations and required control effort. They concluded that this approach resulted in a better system performance than if the sequential approach was followed.

Chan *et al.* [58] experimentally used feedback control to control the vibration of a three-stage tensegrity structure using piezoelectric transducers. The experiments showed significant damping for the first two bending modes. De Jager and Skelton [59] developed an algorithm for the efficient placement of actuators and sensors for a planar tensegrity to achieve a desired level of performance. Bel Hadj Ali and Smith [60], building on [61, 62], conducted active vibration control simulations and experiments on a large tensegrity structure. They successfully used a multi-objective control strategy to move the structure's natural frequencies away from the excitation frequency by altering the pre-stress in the structure.

Even though tensegrity structures saw their debut in the worlds of art and architecture, it wasn't long before the engineering community started paying attention to their attractive attributes: they are lightweight compared to similar truss and frame structures, feature a large stiffness-to-mass ratio, and have the added advantage of being foldable and easy to deploy. Moreover, while a tensegrity can support bending, its individual elements are only loaded in tension or compression, which results in simpler and more precise mathematical models. Finally their components can simultaneously act

as load-bearing elements and as sensors/actuators, enabling engineers to monitor and control the structure's configuration and dynamics.

Capitalizing on these characteristics, the use of tensegrities as deployable space structures, such as antennae, masts and satellite reflectors, has been analyzed and demonstrated, *e.g.*, in [47, 63-66]. Tensegrity-based morphing wings [67], fins [68] and airfoils [69] have also been investigated, and tensegrity robots, able to crawl or slide by changing the tensions in the tendons, have been designed and built [70-74].

With regards to fabricating the structures, steel cables, wires and fishing line were among the materials used for the flexible tendons, while metallic or wooden bars and pipes have been used as the compression elements, with the assembly usually put together by hand. Amendola *et al.* [75] were the first to use additive manufacturing to partially build tensegrity prisms and columns, and more recently, Liu *et al.* [76] demonstrated active deployable tensegrity structures that are 3D-printed from thermally responsive shape-memory polymers.

In the area of biomechanics, tensegrity structures have been suggested as valid models for the study of viruses [77], the cell cytoskeleton [78], the spine [79] and the bone-muscle structure of humans and animals [80, 81]. In nanotechnology, a tensegrity architecture has been successfully used for assembling and building DNA molecules [82-84], with many potential applications in the areas of diagnostics, drug delivery and bio-sensing.

## 2.2 Periodic Structures

A periodic structure is an array of identical elements connected together in an identical manner. The periodicity may be linear or circular, and may occur along one, two, or three axes. Periodic structures are abundant in nature (*e.g.*, the molecular structure of crystalline solids, honeycombs) and in engineering applications (*e.g.*, railway tracks, skin-stringer structures in aircraft fuselage, and cellular structures). Engineered periodic structures are easier to manufacture and assemble than uniform structures and are typically characterized by a high strength-to-weight ratio and high impact and temperature resistance [85], as well as favorable dynamic characteristics making them good candidates as vibration isolators and waveguides [86].

In an excellent historical account, Brillouin [87] traces the study of the dynamics of periodic structures back to Newton and his attempt to derive a formula for the speed of sound in air, in which he modeled sound as an elastic wave propagating along a one-dimensional lattice of equally-spaced point masses connected by springs. Towards the end of the nineteenth century, Lord Kelvin, building on the work of Newton, Cauchy, and Baden-Powell, derived the dispersion curves of a two-particle lattice which exhibited the behavior of a band-pass filter. A physical model of the lattice was later constructed by Vincent [88], and his experimental results matched Kelvin's analysis. Electric analogues of the mechanical periodic arrays were investigated by Heaviside and Vaschy and were successfully realized by Pupin in 1900 and by Campbell in 1906, leading to the invention of electric filters and the telephone loading coil [87, 89-91].

During the first half of the twentieth century, a renewed interest in the problem emerged, albeit from the field of solid-state physics, to investigate the behavior of electrons

and the propagation of electromagnetic waves in crystals (*e.g.*, Born and von Karman [92], Bloch [93], and Wigner and Seitz [94]). The theorem developed by Bloch stated that for a wave propagating in an infinite lattice of identical cells, the change in the complex wave amplitude from one cell to the next does not depend on the cell's location within the medium. The theorem was based on an earlier theorem by Floquet to solve Mathieu's equation, and effectively reduced the problem of analyzing the dynamics of an infinite periodic structure to the study of the repeating unit cell. Brillouin [87] used Bloch's theorem to investigate the propagation of waves in several mechanical and electrical periodic systems, and provided detailed physical and mathematical insights of these systems.

Cremer and Leilich [95] were the first to adopt the wave approach to investigate the bending vibrations of periodic beams and were the first to show that waves can propagate without decay only in certain frequency bands, known as propagation bands or pass bands, which alternated with other frequency bands – attenuation bands or stop bands – where wave propagation was prohibited as the wave decayed as it spread. The term *bandgap* is also often used, especially in the solid state physics literature [96], to refer to the stop bands.

Miles [97] used a difference equation formulation to investigate the normal modes of vibration of a continuous beam supported on many supports. Lin [98] followed the same approach to investigate the vibration of continuous skin-stringer panels, typical of aircraft fuselage panels. They observed that the structures behaved like band-pass filters and that the natural frequencies fall within the frequency pass bands. Lin and McDaniel [99] later used the Transfer Matrix method to determine the frequency response of an Euler-Bernoulli

beam of finite length resting on many elastic supports, with and without external damping units.

Heckl [100] performed a theoretical analysis of the propagation of bending and torsional (or longitudinal) waves in beams with periodic discontinuities and in grillages. He considered successive reflections and transmissions at the discontinuities, as well as the conversion between bending and torsional (or longitudinal) waves. He concluded that the vibration patterns in all periodic sections are similar and that existed a “propagation constant” which relates the wave amplitude in one periodic cell to that in the next cell, and which does not depend on the cell’s location. He derived approximate expressions for the propagation constants in terms of the reflection and transmission coefficients, and observed that, for each type of waves, there existed frequency bands with high attenuations and others with no attenuation.

Significant contributions to this field were made by Professor Denys Mead and his students and collaborators [101]. Sen Gupta [102, 103] studied the free and forced vibration of beams, plates, and skin-rib structures by extending the wave propagation technique – originally due to Brillouin’s work – to the fourth-order differential equations governing beams and plates. He also presented methods of finding the natural frequencies of finite, supported beam structures, from the characteristic propagation constant.

In 1973, Mead [104] developed a general method based on Bloch’s theorem to investigate harmonic wave propagation in one-and two-dimensional periodic structures, with and without damping. Orris and Petyt [105] combined Mead’s method with the finite element method to obtain the propagation constants for a multi-supported beam and for a

skin-rib structure, typical of an aircraft tailplane. The numerical results of both problems converged rapidly to the exact solutions available.

Aside from the periodic structures' characteristic pass and stop bands, Hodges [106] investigated the effect that disruptions to the perfect periodicity of the lattice would have on its wave transmission characteristics in the pass bands. He concluded that introducing disorder has a *confining* effect, preventing the propagation of vibrations at large distances from the source. This phenomenon is known as "localization" and had been predicted by Anderson [107] in the context of solid-state physics. Experiments and further quantitative analyses of the localization factor were subsequently carried out, *e.g.*, in [108-110]. Gei [111] investigated the effect of quasi-periodicity on the propagation of axial and flexural waves in rods and beams.

Sigalas and Economou [112] and Kushwaha *et al.* [113] applied Bloch's theorem to investigate the propagation of acoustic and elastic waves through a periodic medium consisting of identical inclusions (spheres or cylinders) placed periodically in a homogeneous material, and demonstrated the existence of frequency band gaps and their dependence on the volume fraction and material properties of the two phases. They named such composites "phononic crystals" and saw their potential as acoustic and elastic wave filters.

Langley [114] showed that two-dimensional periodic media, in addition to exhibiting the frequency pass and stop bands characteristic of one-dimensional periodic media, also exhibit directional filtering behavior: the presence and width of pass and stop bands will depend on the considered direction of wave propagation on the structure's surface.

Baz and coworkers [115-117] introduced active periodic structures, conceived by adding either piezoelectric actuators or shape memory inserts periodically along otherwise homogeneous rods. The inserts are actively controlled (electrically or thermally) in order to tune the location and width of the stop bands of the now periodic structure. The authors also utilized the localization phenomenon to confine vibration to a specific region of the structure by selectively tuning its components, thus creating both spectral and spatial filtering effects in one-dimensional structures.

Ruzzene *et al.* [118] used Bloch's theorem to investigate out-of-plane vibration of two-dimensional honeycomb grids and the effect of changing the cells' geometry on the directional characteristics of the waves. They verified their findings numerically and concluded that the geometry can be tuned to yield a desired spatial filtering effect, making such cellular grids attractive for vibration attenuation and isolation applications. Phani *et al.* [119] followed the same approach to investigate the propagation of plane waves in two-dimensional periodic lattices with different cellular topologies. Spadoni *et al.* [120] extended the analysis to hexagonal honeycomb lattices in a chiral configuration.

Hutchinson and Fleck [121] investigated the structural mechanics (namely, states of self-stress and collapse mechanisms) of infinite periodic trusses by applying Bloch's theorem to the equilibrium and compatibility equations, extending the matrix methods developed by Pellegrino and Calladine [20] to the periodic case.

Hussein [122] and Hussein and Frazier [123] developed the "Bloch modal analysis" framework to analyze periodic materials incorporating viscous damping and investigated the effect of damping on the frequency band structure. Meanwhile, Farzbod and Leamy [86, 124] conducted a rigorous analysis of Bloch's method and its applicability to the study



of wave propagation in periodic structures. In [125], they extended the method to the study of periodic structures with general damping and investigated the resulting dispersion curves and band structures.

A different mechanism for impeding wave propagation in structures involves the introduction of locally-resonant structural units within the larger structure. The resonators are tuned to specific frequencies and act as vibration isolators at those frequencies, preventing wave propagation through the main structure. Liu *et al.* [126] realized a sonic crystal that utilized this concept and featured stop bands at wavelengths two orders of magnitude higher than would be possible using periodicity alone. The material also exhibited negative elastic constants at certain frequencies.

Several authors have since explored the use of local resonance as a mechanism to create and control stop bands, *e.g.*, in beams [127-129], plates [130, 131], solid media with rubber or vacuum cylindrical inclusions [132], or in a fluid with embedded hollow spheres or cylinders [133]. Gonella *et al.* [134] used small piezoelectric beams as the local resonators in a hexagonal honeycomb lattice, combining wave filtering with energy harvesting. The investigation of the nature of the stop bands occurring due to local resonators and how they differ from those occurring due to the more conventional Bragg scattering phenomenon of periodic structures, as well as the necessary conditions to transition from one type to the other, were investigated, *e.g.*, in [135-137].

From a design perspective, many authors have followed an optimization approach with the goal of maximizing the width of a particular stop band, *e.g.*, by finding the optimum topology of the periodic inserts [138] or the optimum magnitude and placement of locally-resonant masses [139], or by using genetic algorithms to find the optimal

geometry and mechanical properties of the periodic inclusions [140]. Hussein *et al.* [141, 142] also used genetic algorithms to maximize the number and total width of stop bands within a certain frequency range, for one- and two-dimensional periodic phononic crystals.

Research into tunable periodic and locally resonant structures has also emerged, with the goal of controlling the widths and/or center frequency of stop bands to accommodate different applications or excitation frequencies. Techniques used include the application of an electric field to change the size of periodic cylindrical inclusions [143], the use of a magnetostrictive material and applying an external magnetic field [144], mechanically rotating periodic inclusions [145], controlling the pre-stress applied to the structure [111, 146], and using piezoelectric materials as local resonators whose properties can be controlled with shunted electrical circuits [147, 148].

The pass and stop band phenomenon characteristic of periodic and locally resonant structures, combined with their directional filtering characteristics, have enabled their use as spectral and spatial filters for sonic [126, 149, 150], ultrasonic [151], and elastic [152] waves, as well as sonic waveguides [153]. Their use has also been demonstrated for vibration reduction [154] and isolation [155] in machine elements and in buildings [156, 157].

Locally resonant structures, which have also been found to exhibit negative elastic moduli in some frequency ranges, have been utilized to synthesize phononic metamaterials – materials which exhibit unconventional properties, such as negative effective density, elastic modulus, and/or index of refraction [158-161] – with applications in the novel realm of acoustic and elastic invisibility cloaks [162].

Phononic metamaterials built with periodic and locally-resonant structures have also been used to design lenses for acoustic [163, 164] and elastic [165] waves, capable of imaging with resolutions below the diffraction limit [166, 167] and of focusing high energy acoustic pulses which could be used as nonintrusive scalpels [168]. Olsson and El-Kady [169] report on microfabricated phononic crystals with applications in RF communications, medical imaging, and nondestructive testing.

### **2.3 Summary**

This chapter has presented a brief survey of the existing literature on tensegrity structures and periodic structures. In the presented survey, emphasis is placed on the individual basic dynamic and wave propagation characteristics of each of the tensegrity and periodic structures. Integration of these characteristics by treating assemblies of tensegrity unit cells as periodic structures is the main objective of this dissertation in order to demonstrate their unique wave propagation and mechanical filtering characteristics.

## Chapter 3: Static and Kinematic Analysis of Icosahedron Tensegrity

### 3.1 Introduction

In this chapter we investigate the icosahedron tensegrity, first proposed by Buckminster Fuller [170, 171]. We describe the structure then analyze its static and kinematic determinacy and what qualifies it as a tensegrity; we then determine the elastic coefficients of the tensegrity.

### 3.2 Unit Cell Description and Material Properties

The tensegrity is shown in Figure 3.1, along with its three orthographic projections. It consists of six identical compression elements (bars or struts) and twenty-four identical tension elements (tendons or strings). The bars are arranged in three pairs where each pair of parallel bars defines a plane that is orthogonal to the planes created by the other two pairs. The resulting shape has twelve vertices and twenty triangular faces (hence the prefix *icosa-*, from the Greek word for twenty).

The compression elements are chosen to be cylindrical bars of length  $l_b$ , cross-section radius  $r_b$ , density  $\rho_b$  and modulus of elasticity  $E_b$ . The flexible tensile elements are massless strings with cross-section radius  $r_s$  and stiffness  $K_s$ . The working length of any string element is calculated to be  $l_s = \sqrt{3/8} l_b$ , and pre-stress can be introduced to the structure by choosing shorter strings and pre-tensioning them. Table 3.1 lists the dimensions and material properties of the bars and strings. Table 3.2 lists the Cartesian coordinates of each vertex, assuming the origin of the coordinate system lies at the centroid

of the tensegrity, and Table 3.3 provides a numbering system for the bars and strings, which will be useful in the finite element formulation of the problem.

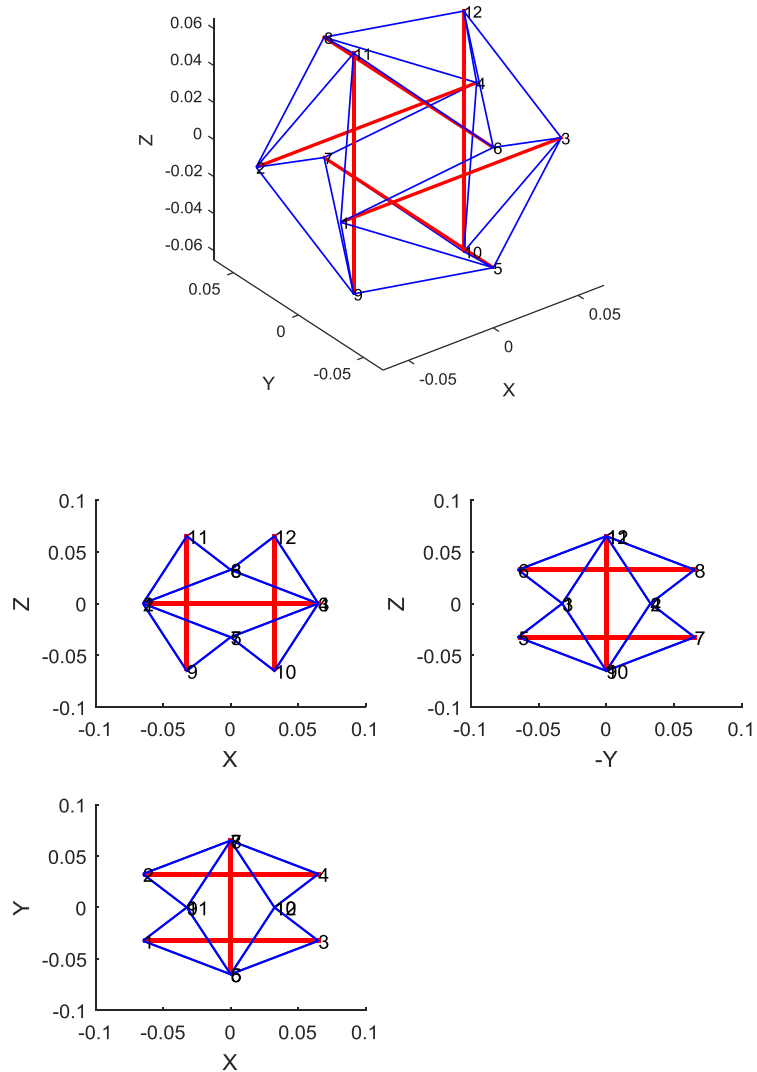


Figure 3.1 Icosahedron tensegrity

$l_b$	13 cm	$l_s$	$\sqrt{3/8} l_b$
$r_b$	5 mm	$r_s$	2.5 mm
$\rho_b$	500 kg/m <sup>3</sup>		
$E_b$	10 <sup>9</sup> N/m <sup>2</sup>	$K_s$	5000 N/m

Table 3.1 Geometric and material properties of tensegrity elements

Vertex number	X	Y	Z
1	$-l_b/2$	$-l_b/4$	0
2	$-l_b/2$	$l_b/4$	0
3	$l_b/2$	$-l_b/4$	0
4	$l_b/2$	$l_b/4$	0
5	0	$-l_b/2$	$-l_b/4$
6	0	$-l_b/2$	$l_b/4$
7	0	$l_b/2$	$-l_b/4$
8	0	$l_b/2$	$l_b/4$
9	$-l_b/4$	0	$-l_b/2$
10	$l_b/4$	0	$-l_b/2$
11	$-l_b/4$	0	$l_b/2$
12	$l_b/4$	0	$l_b/2$

Table 3.2 Coordinates of tensegrity vertices

BARS		STRINGS							
Member number	Start – end	Member number	Start – end	Member number	Start – end	Member number	Start – end	Member number	Start – end
1	1 – 3	7	1 – 5	13	2 – 11	19	4 – 8	25	6 – 11
2	2 – 4	8	1 – 6	14	2 – 8	20	4 – 7	26	6 – 12
3	5 – 7	9	1 – 11	15	3 – 5	21	4 – 10	27	7 – 9
4	6 – 8	10	1 – 9	16	3 – 6	22	4 – 12	28	7 – 10
5	9 – 11	11	2 – 7	17	3 – 10	23	5 – 9	29	8 – 11
6	10 – 12	12	2 – 9	18	3 – 12	24	5 – 10	30	8 – 12

Table 3.3 Numbering scheme for tensegrity elements

### 3.3 Static and Kinematic Analysis of the Unit Cell

#### 3.3.1 Overview of the Procedure

Given a proposed tensegrity configuration, we follow the procedure developed by Calladine and Pellegrino [18, 20, 28] to identify the mechanisms and states of self-stress that it may possess and investigate its stability.

The first step is the construction of the structure's equilibrium matrix,  $A$ , which relates the forces in the members to the applied nodal forces, according to the matrix equation

$$\mathbf{A} \cdot \mathbf{t} = \mathbf{F} \quad (3.1)$$

where  $\mathbf{t}$  and  $\mathbf{F}$  are the vector of member force densities (in units of force per length) and the vector of nodal forces, respectively.

Alternatively, one may choose to construct the structure's kinematic matrix,  $\mathbf{H}$ , which is the transpose of the equilibrium matrix [18] and which relates small nodal displacements to elongations in the members, as shown by the kinematic equation

$$\mathbf{H} \cdot \mathbf{q} = \mathbf{e} \quad (3.2)$$

where  $\mathbf{q}$  and  $\mathbf{e}$  are the vector of nodal displacements and the vector of the members' elongation coefficients (defined as the product: elongation  $\times$  length), respectively.

We compute the rank of the equilibrium matrix, and determine its left and right null spaces. Every right null vector represents a state of self-stress – a configuration of member loading that is in equilibrium under no external forces; the presence of which renders the structure statically indeterminate. Every left null vector (or, equivalently, every right null vector of the kinematic matrix) represents an inextensional mechanism – a set of nodal displacements that involve no changes in members' lengths, to first order approximation; the presence of which renders the structure kinematically indeterminate.

Any mechanisms identified in the previous step will fall into one of three categories:

- i. Finite (large displacement) mechanisms involving absolutely no changes in members' lengths.

- ii. Infinitesimal mechanisms involving small changes in members' lengths that are of second order in terms of nodal displacements.
- iii. Infinitesimal mechanisms involving small changes in members' lengths that are of third or higher order in terms of nodal displacements.

Tarnai [19] and Pellegrino and Calladine [20] show that given a statically and kinematically indeterminate structure whose mechanisms fall exclusively into the second category, pre-stressing the structure in accordance with its state(s) of self-stress will impart stiffness to those mechanisms and stabilize the entire structure. The stiffness of the structure will be on the order of the pre-stress, and they refer to such mechanisms as “first-order inextensional mechanisms”. Pre-stressing the structure will, however, have no effect on any finite mechanisms, or any mechanisms that involve deformations that are of third or higher order in the nodal displacements.

In order to identify which category the mechanisms belong to, Pellegrino and Calladine developed the “Product-Force vector” method, which, conceptually, activates one mechanism at a time, loops through the states of self-stress, and checks to see whether this new configuration (mechanism + state of self-stress) will be able to support a new set of nodal forces that was previously “forbidden” on account of the mechanism. If this is the case for all mechanisms, then the mechanisms were indeed of second order in the displacements and the pre-stressed structure will be stable. If, additionally, all members are ‘properly loaded’, *i.e.*, the struts are loaded in compression and the tendons in tension, then the structure can be classified as a tensegrity.

An alternative method for determining whether the mechanisms can be stiffened by the self-stress – which is the approach we follow in this chapter – is the calculation of the



stiffness matrix of the structure, under the various self-stress cases. If the pre-stressed stiffness matrix is positive-definite, this means that all the mechanisms have been stiffened and the entire structure is stable. Conversely, any zero eigenvalue of the stiffness matrix will correspond to an eigenvector representing a finite mechanism or an infinitesimal mechanism of third or higher order in the displacements and which could not be stiffened by the applied state of self-stress.

### 3.3.2 Analysis of the Icosahedron Tensegrity

The unconstrained icosahedron has  $j = 12$  nodes and  $m = 30$  members, yielding a nodal force vector  $\mathbf{F}$  with  $3j (= 36)$  elements, and a vector  $t$  with  $m$  elements. The equilibrium matrix (of size  $3j \times m = 36 \times 30$ ) is obtained by analyzing the external nodal forces along the members. The equilibrium matrix and the two vectors are given in Appendix A.

Using MATLAB, we compute the rank and null spaces of the equilibrium matrix. We find that the rank is 29, meaning that the structure is statically and kinematically indeterminate with seven mechanisms (left null vectors) and one state of self-stress (right null vector). Six of the mechanisms are the rigid body modes and can be eliminated by applying the appropriate boundary conditions, leaving one mechanism,  $\mathbf{M}_1$ , that needs to be analyzed. After scaling the vector,  $\mathbf{M}_1$  is given by

$$\mathbf{M}_1 = [0 \ -1 \ 0 \ 0 \ 1 \ 0 \ 0 \ -1 \ 0 \ 0 \ 1 \ 0 \ 0 \ 0 \ -1 \ 0 \ 0 \ 1 \ 0 \ 0 \ -1 \ 0 \ 0 \ 1 \ -1 \ 0 \ 0 \ 1 \ 0 \ 0 \ -1 \ 0 \ 0 \ 1 \ 0 \ 0]^T \quad (3.3)$$

The mechanism  $\mathbf{M}_1$  corresponds to the symmetric expansion of the icosahedron by moving every two parallel struts symmetrically away from each other in their plane. Therefore it is not a finite mechanism, but it remains to be seen whether it is a first-order inextensional mechanism.

The state of self-stress,  $\mathbf{S}_1$ , is given below and consists of equal compressive forces in the six struts and equal tensile forces in the twenty-four tendons:

$$\mathbf{S}_1 = \left[ -1 \ -1 \ -1 \ -1 \ -1 \ -1 \ \frac{2}{3} \ \frac{2}{3} \ \frac{2}{3} \ \frac{2}{3} \ \frac{2}{3} \ \frac{2}{3} \ \frac{2}{3} \ \frac{2}{3} \ \frac{2}{3} \ \frac{2}{3} \ \frac{2}{3} \ \frac{2}{3} \ \frac{2}{3} \ \frac{2}{3} \ \frac{2}{3} \ \frac{2}{3} \ \frac{2}{3} \ \frac{2}{3} \ \frac{2}{3} \right]^T \quad (3.4)$$

We will now verify that, in the absence of pre-stress, the structure is not stiff: using the Finite Element Method, we assemble the structure’s global stiffness matrix from the element stiffness matrices for each element, treating each member (strut or cable) as a single “bar” element subject to uni-axial loading and a general case of pre-stress. The element stiffness matrix for the three-dimensional case is given in Appendix B. In matrix form, the nodal forces and displacements of the structure are related by the equation

$$\mathbf{F} = \mathbf{K} \cdot \mathbf{q} \quad (3.5)$$

where  $\mathbf{F}$  is the vector of external nodal forces, defined in Appendix A,  $\mathbf{K}$  is the global stiffness matrix, and  $\mathbf{q}$  is the vector of degrees of freedom, defined as follows:

$$\mathbf{q} = [x_1 \ y_1 \ z_1 \ x_2 \ y_2 \ z_2 \ \dots ]^T \quad (3.6)$$

The following six boundary conditions were chosen to serve the dual purpose of eliminating the rigid body modes while not interfering with the mechanism  $\mathbf{M}_1$  (this can be verified by re-calculating the null space of the constrained equilibrium matrix):

$$\begin{aligned}
x_5 &= x_7 = 0 \\
y_9 &= y_{11} = 0 \\
z_9 &= z_{10} = 0
\end{aligned}
\tag{3.7}$$

Having computed the stiffness matrix, we set the pre-stress to zero and compute the eigenvalues of the matrix. We find that the matrix is positive semi-definite on the account of one eigenvalue equal to zero.

We then apply a pre-stress the structure that is a positive multiple of the state of self-stress  $\mathbf{S}_1$ , by subjecting every string element to an arbitrary initial extension,  $\Delta_0$ . The corresponding pre-load force density in the string,  $f_s$ , is thus

$$f_s = \frac{K_s \Delta_0}{l_s} \tag{3.8}$$

where  $K_s$  and  $l_s$  are the string's stiffness and length, respectively. The pre-load force density in the bars,  $f_b$ , is obtained from  $\mathbf{S}_1$  to be

$$f_b = -\frac{3}{2}f_s \tag{3.9}$$

Re-calculating the stiffness matrix, we observe that matrix becomes positive definite with its lowest eigenvalue proportional to the level of pre-stress. The pre-stress has effectively stabilized the structure by imparting ‘first-order stiffness’ to the mechanism. Therefore the stable pre-stressed structure can be classified as a tensegrity, even by the most stringent of definitions (a pin-jointed structure with rectilinear elements, discontinuous compression elements, continuous tensile elements, and an infinitesimal mechanism that gets stiffened by the state of self-stress). Figure 3.2 shows the change in the smallest two eigenvalues of the stiffness matrix against the level of pre-stress.

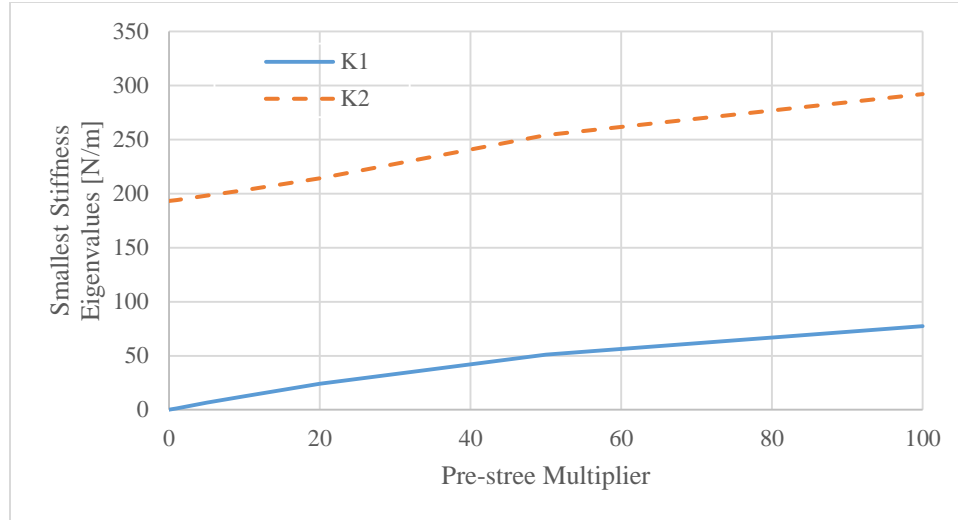


Figure 3.2 Stiffening effect of pre-stress

### 3.4 Mechanical Properties of the Unit Cell

In this section we use finite element analysis to determine the effective elastic modulus,  $E$ , shear modulus,  $G$ , and bulk modulus,  $B$ , of the icosahedron tensegrity, and investigate the effect of the pre-stress on the moduli. It will be useful to visualize six square end-plates surrounding the tensegrity – one at each end of every pair of parallel struts and normal to the struts – through which the forces and displacements are applied. This is done in order to simplify the problem of determining the areas acted upon by the forces and the volume occupied by the structure. The end-plates will not, however, be included in the finite element analysis. The entire structure can thus be visualized as a cube, albeit with disjointed faces, with the icosahedron tensegrity as its backbone. Figure 3.3 shows the structure with its “back”, “right” and “bottom” end-plates.

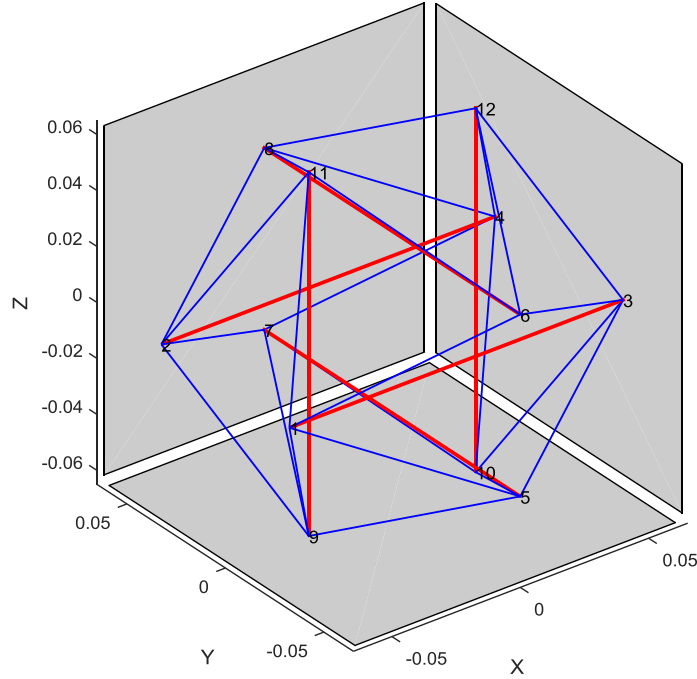


Figure 3.3 Unit cell with three end-plates

In order to determine the elastic modulus  $E$ , we apply – through the right end-plate – a force on nodes 3 and 4 pointing in the direction of the positive X axis ( $F_{3x} = F_{4x} = 1$ ), while constraining the left nodes (1 and 2) from moving along the X axis ( $x_1 = x_2 = 0$ ). Additional boundary conditions are imposed ( $y_5 = y_6 = y_7 = y_8 = z_9 = z_{10} = z_{11} = z_{12} = 0$ ) to eliminate rigid body motion and approximate real testing conditions.

After eliminating the equations and degrees of freedom corresponding to the constrained boundary conditions from the global force-displacement equation, we use MATLAB to solve for the unknown displacements:

$$x_R = K_R^{-1}F_R \quad (3.10)$$

where the subscript  $( )_R$  represents the reduced vectors and matrices. We note that in the absence of pre-stress the global stiffness matrix is still singular, which is why the no pre-stress case is not considered.

The elastic modulus is computed from the equation

$$E = \frac{F_n \cdot l_x}{\Delta_n \cdot A_n} \quad (3.11)$$

where  $F_n$  is the total applied force ( $F_n = F_{3x} + F_{4x}$ ),  $l_x$  is the length of the unit cell along the X axis, which is equal to the length of the bar,  $l_b$ ,  $A_n$  is the area of the end-plate on which the force is acting and equals  $l_b^2$ , and  $\Delta_n$  is the displacement along the X axis of the loaded nodes ( $\Delta_n = x_3 = x_4$ ).

In order to determine the shear modulus, a known shear displacement,  $\Delta_{sh}$ , is imposed on the top nodes (11 and 12) in the direction of the positive X axis ( $x_{11} = x_{12} = \Delta_{sh}$ ), while nodes 9 and 10 are completely constrained ( $x_9 = y_9 = z_9 = x_{10} = y_{10} = z_{10} = 0$ ). An additional boundary condition ( $y_5 = 0$ ) is introduced to prevent rigid body motion. The resulting nodal forces are computed and the shear modulus  $G_{zx}$ , is obtained from the equation

$$G_{zx} = \frac{F_{sh} \cdot l_z}{\Delta_{sh} \cdot A_{sh}} \quad (3.12)$$

where  $F_{sh}$  is the total shear force ( $F_{sh} = F_{x_{11}} + F_{x_{12}}$ ) resulting from the imposed deformation,  $l_z$  is the height of the unit cell along the Z axis, which is equal to the length of the bar,  $l_b$ , and  $A_{sh}$  is the area on which the force is applied, which is the area of the top end-plate, also equal to  $l_b^2$ .

Finally, in order to determine the bulk modulus, we impose symmetry boundary conditions and apply a hydrostatic pressure on the structure, which translates into nodal forces that push inwards on every node, and calculate the resulting compression in the bars and the corresponding change in volume of the cube enclosed by the six end-plates. The bulk modulus is calculated from the equation

$$B = -V \frac{\Delta P}{\Delta V} \quad (3.13)$$

where  $V$ ,  $\Delta V$ , and  $\Delta P$  are the cube's initial volume, the change in volume, and the applied pressure, respectively.

Figure 3.4 shows the elastic, shear, and bulk moduli against the level of pre-stress (represented by the initial elastic strain in the strings) against the level of pre-stress. We notice that  $E \approx 3B$ , and that the elastic and bulk moduli are not affected by the pre-stress since they primarily depend on the stiffness of the rigid compressive elements. The shear modulus initially increases with the pre-stress until it reaches a maximum at a strain value of 0.4, after which it decreases with added pre-stress.

Comparing the bulk modulus of the tensegrity to its shear modulus, we notice that the ratio  $B/G$  is around 5000, as shown in Figure 3.5. This means that it is much easier to change the shape of the structure while keeping its volume constant than it is to change its volume while keeping its shape constant. Such elastic properties approximate those of liquids, and are being sought after for the development of pentamode metamaterials, *e.g.*, for elastodynamic cloaking applications [172, 173].

This result is significant because it suggests the possibility of using the icosahedron tensegrity as a building block in the synthesis of pentamode metamaterials. The first

experimental pentamode metamaterial was fabricated in 2012 by Kadic *et al.* using laser lithography and featuring a  $B/G$  ratio of about 1000 [173, 174]. The same ratio for gold – one of the largest among naturally-occurring bulk materials – is about 13.

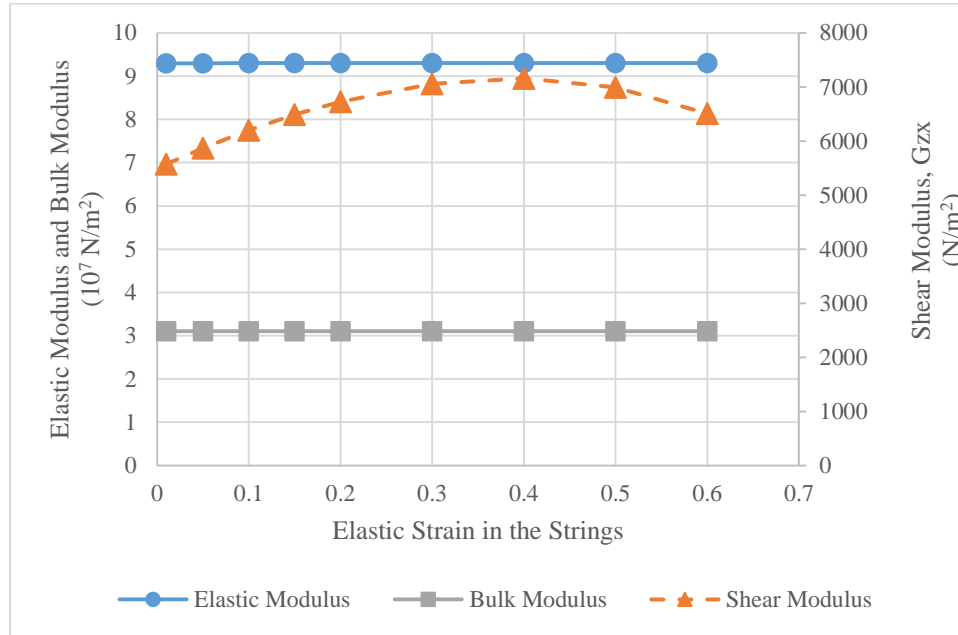


Figure 3.4 Elastic coefficients of icosahedron tensegrity

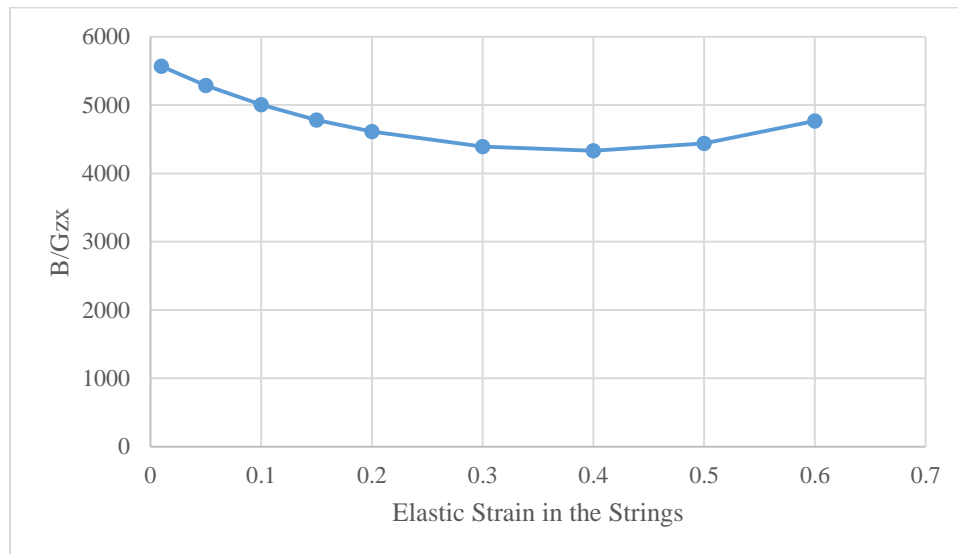


Figure 3.5 Bulk-to-shear ratio of icosahedron tensegrity



### 3.5 Tensegrity Prototype

Figure 3.6 shows a 3D-printed prototype of the icosahedron tensegrity, created from a CAD (SolidWorks) solid model using an Objet 500® Connex3™ 3D printer by Stratasys, which has the capability of printing rigid and rubber-like materials. The material chosen for the rigid links is known by the name “VeroWhite Plus” and has a reported density of  $1175 \text{ kg/m}^3$  [175], and the elastic modulus was experimentally found to be  $912 \text{ MPa}$ . The rubber-like material chosen for the flexible links has the name “FLX 9870-DM” for the strings and has a reported modulus of elasticity in the range of  $3.5 - 5 \text{ MPa}$  [176] and its density was measured to be  $1143 \text{ kg/m}^3$ .

The rigid bars are cylinders 32 mm in length and 2.5 mm in diameters, while the flexible links have a square cross-section of side 1.80 mm. The bars have spherical terminations, 3mm in radius, in order to provide a large enough gripping surface for the flexible links, while allowing the links to pivot easily on any surface, *e.g.*, when undergoing shear deformation. The dimensions of the cell were chosen for it to fit inside, or flush against, the acoustic impedance tube setup.



Figure 3.6 3D-printed icosahedron tensegrity

## 3.6 Experimental Determination of Cell's Constants

### 3.6.1 Shear Modulus

Figure 3.7 shows the icosahedron tensegrity undergoing a dynamic shear test. The cell rests on a bottom plate that is fully constrained to the foundation and which incorporates small indentations to seat the spherical bar ends, constraining their translation while allowing them to rotate. A similar plate fits on the top of the array and is attached, via a connecting link and an end-plate, to an electromagnetic shaker (LDS V408), the signal to which is generated using a signal generator/analyzer (Stanford Research SRS-780) and amplified using the LDS PA100E amplifier. A Force sensor (PCB Piezotronics, Model 208M51<sup>1</sup>) fits between the shaker and the face plate and measures the force applied by the shaker, while a laser sensor (Matsushita NAIS LM200 ANL2534A<sup>2</sup>) measures the position of the top plate. Both signals are acquired using an oscilloscope (Tektronix TDS 3014) and subsequently analyzed.

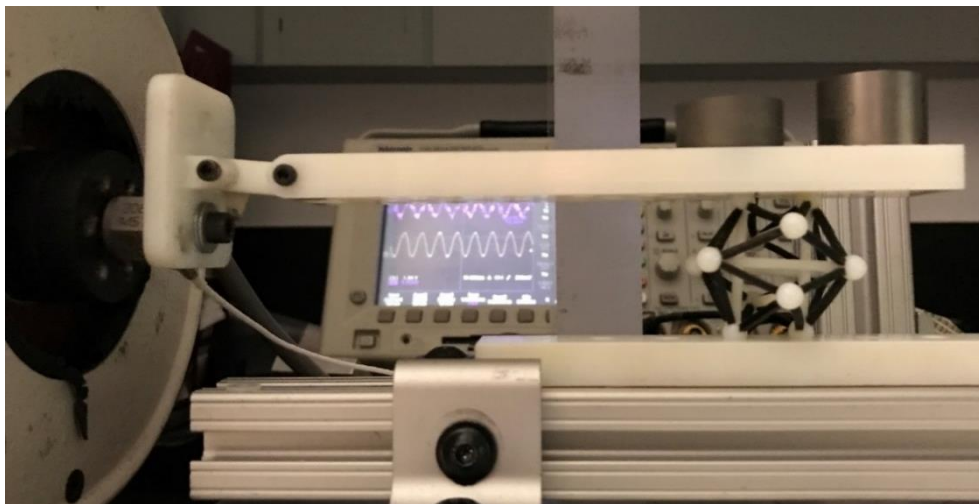


Figure 3.7 Shear testing of tensegrity cell

<sup>1</sup> S/N: 16128 – Sensitivity: 2.54 mV/N

<sup>2</sup> Sensitivity: 0.5 V/mm

Figure 3.8 shows the sensors' output signals for a sinusoidal input to the shaker at 2 Hz, which after proper conversions<sup>3</sup>, result in the force-displacement plot of Figure 3.9. The hysteresis loop indicates energy dissipation in the viscoelastic, rubber-like elements. The general slope of the curve yields the stiffness of the cell to shear deformation, found to be approximately 62 N/m, and which corresponds to an equivalent shear modulus,  $G_{zx}$ , of 1600 N/m<sup>2</sup>. The maximum deformation that was achieved during testing was 3.4 mm, corresponding to a shear strain of 0.1, and the original shape was fully recovered upon load removal/reversal.

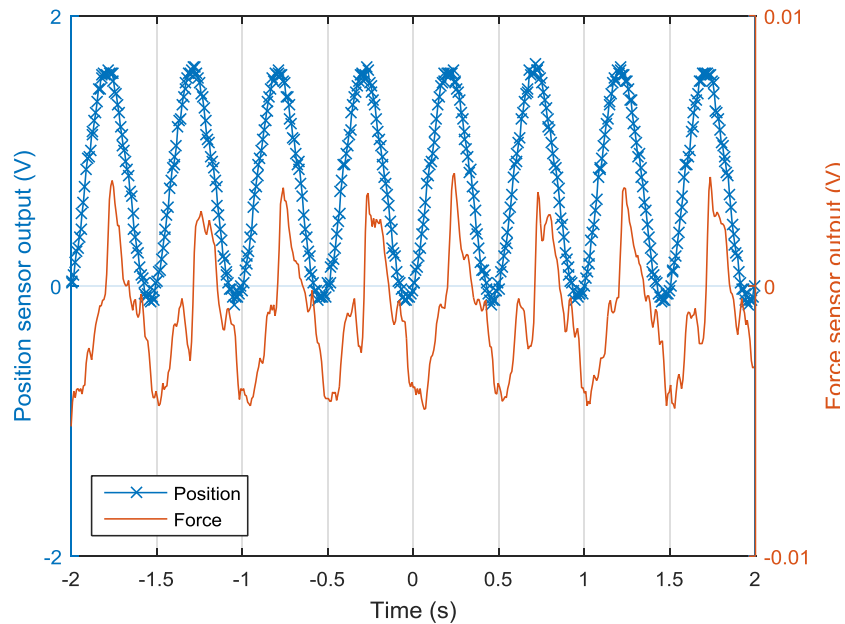


Figure 3.8 Sensors' output – unit cell in shear

<sup>3</sup> The force sensor signal is multiplied by a 10X gain

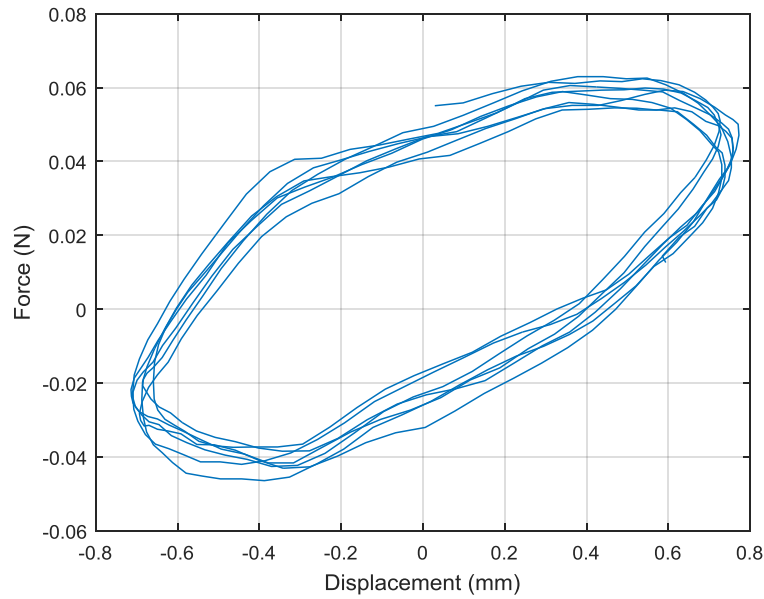


Figure 3.9 Experimental force-displacement (cell in shear)

### 3.6.2 Elastic Modulus

Figure 3.10 shows the setup used in the determination of the elastic modulus of the cell. The same equipment of the previous section was used, with the exception that all the surfaces in contact with the tensegrity were rigid, polished surfaces, allowing the bar ends to slide in their plane. The cell is dynamically loaded in compression between a plate attached to shaker (on the left in the figure) and a second, fixed plate (on the right). Before starting the experiment, the cell is manually pre-loaded in compression using the right plate to ensure that the shaker plate will not lose contact when it retracts, therefore the cell remains in compression at all times.

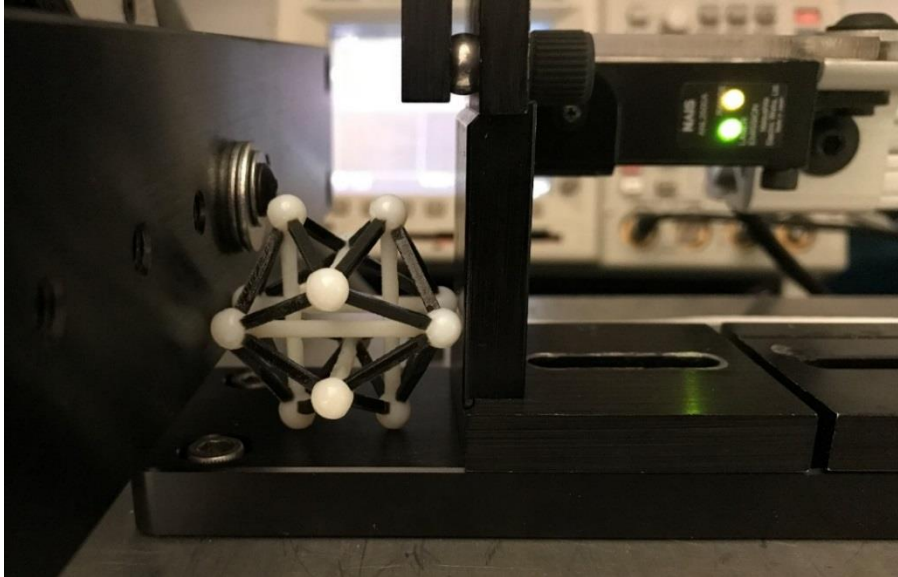


Figure 3.10 Compression testing of tensegrity cell

The outputs of the two sensors are shown in Figure 3.11 for a sinusoidal input signal at  $2\text{ Hz}$  which, after the appropriate conversions<sup>4</sup>, yields the force-displacement curve of Figure 3.12. The axial stiffness of the cell is given by the slope of the curve, which is found to be  $120\text{ kN/m}$ , with a corresponding elastic modulus,  $E_{xx}$ , of  $3.3 \times 10^6\text{ N/m}^2$ . While direct measurement of the bulk modulus,  $B$ , was not possible, by using the observation made in Section 3.4 that  $E \approx 3B$ , we can estimate the bulk modulus of the unit cell to be approximately  $1.1 \times 10^6\text{ N/m}^2$ , which we observe to be 500 times higher than the shear modulus.

---

<sup>4</sup> The force sensor signal is multiplied by a 10X gain

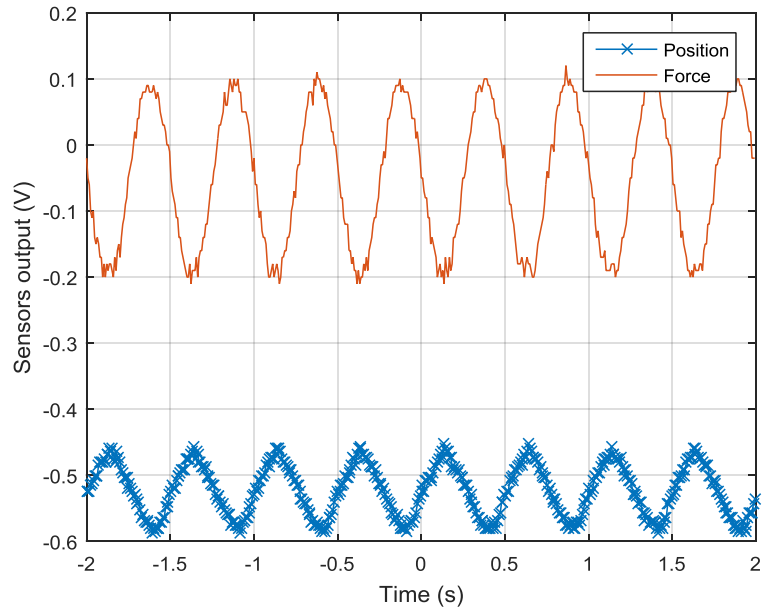


Figure 3.11 Sensors' output –unit cell in compression

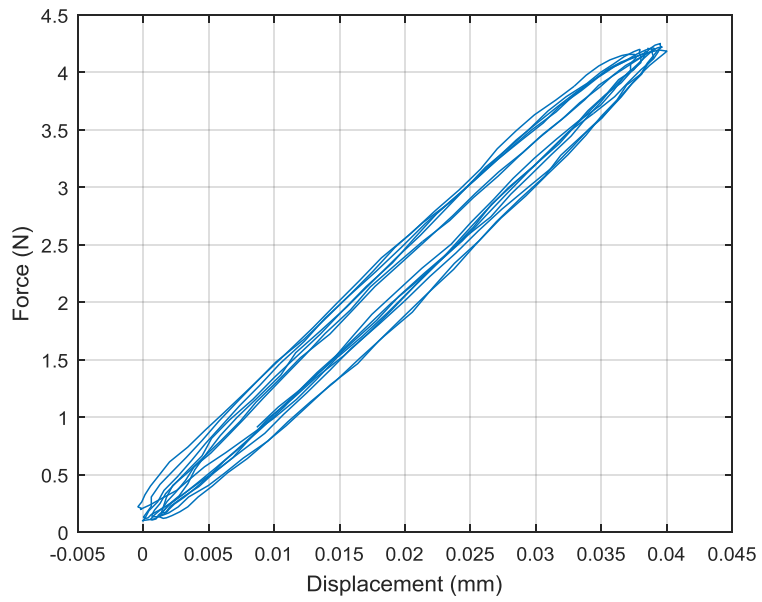


Figure 3.12 Experimental force-displacement (cell in compression)

### 3.6.3 Analysis and Discussion

With regards to shear loading, the numerical simulations, performed in the manner detailed in Section 3.4 using the material constants and dimensions given in section 3.5 and assuming an initial strain of 0.01, yield a stiffness in shear of  $72\text{ N/m}$ , or 17% higher than the experimental value. We make the following observations regarding the comparison between the experimental results and the numerical model:

- There was no mechanism to introduce or measure pre-stress/initial strain in the 3D-printed prototype. While a cell without pre-stress should not be stable (as per Section 3.3.2), the prototype was observed to be indeed stable with regards to its infinitesimal mechanism. This may suggest that the 3D-printing process and the following post-processing of the part may have caused the flexible links to shrink slightly compared to the design values, thereby generating pre-stress. Noting that the pre-stress has a strong influence on the shear modulus (as per Section 3.4), further investigations into the material properties of the elastomeric link, as well as the printing process itself, are needed in order to be able to fully characterize the prototype and ensure the validity of the model.
- The shear stiffness and, consequently, the shear modulus vary linearly with the elastic modulus of the flexible elements. An accurate material characterization, including viscoelastic effects, is therefore necessary for a representative numerical model.

With regards to the elastic modulus determination using the dynamic compression test, numerical simulations yield an equivalent stiffness of  $236\text{ kN/m}$  for the cell and a

corresponding elastic modulus of  $6.2 \times 10^6 \text{ N/m}^2$ , approximately twice the experimentally-determined values. We believe that this discrepancy is primarily due to misalignment of one or both of the rigid links relative to the cell's axis, which we investigate further below. Another source of discrepancy lies in the fact that the stiffness of the spherical bar joints and their interaction with the longitudinal bars were not accounted for in the numerical model.

With regards to the misalignment, given that the rigid element length is  $38 \text{ mm}$  (including the spherical endings), an angular misalignment of merely 2 degrees between the rigid links and the horizontal axis along which the force is applied and displacement is measured, will lead to a perceived deformation of  $0.023 \text{ mm}$ , or more than half the total displacement measured in the experiment.

Such a deviation could occur due to rotation of the links during testing, since the bar ends are free to move in the planes of their constraining end plates. A workaround would involve designing and using end plates that constrain the sliding motion of the bar ends, replacing the sliding boundary conditions with either fixed or rotating boundary conditions. Another option would be testing of the cell in tension.

Another root cause of this misalignment could be slight variations in the elements' dimensions and stresses, brought on either by the 3D printing process, *e.g.*, with either material being anisotropic, or during the post-processing the part in order to remove the support material, which is done manually and using a sonication bath and which could introduce some defects or residual stresses. Investigations of the material properties in relation to the orientation of the printed part being may shed some light on whether this is happening.



### **3.7 Summary**

In this chapter, we investigated the kinematic and static characteristics of the icosahedron tensegrity, confirming that it satisfies the most rigorous conditions to qualify as a tensegrity structure, and numerically computing its elastic coefficients, showing that it exhibits a very high bulk-to-shear ratio suggesting the possibility of using the tensegrity in the creation of pentamode metamaterials.

We designed and built a prototype of the tensegrity using bi-material 3D printing and conducted tests to determine its elastic and shear moduli, showing very good agreement with the numerical model for the shear modulus, and some discrepancy with the model for the elastic modulus. We provided some insight as to the possible root causes of this discrepancy and suggested some workarounds. The bulk modulus estimated from the experiments is still between two and three orders of magnitude higher than the measured shear modulus.

## **Chapter 4: Static and Dynamic Analysis of Periodic Icosahedron Tensegrity Structures**

### **4.1 Introduction**

Following the determination of the static properties of the icosahedron tensegrity in the previous chapter, we investigate in this chapter the static and dynamic properties of periodic structures obtained by tessellating the icosahedron tensegrity unit cell along one or more axes.

### **4.2 One-dimensional Periodic Arrays**

#### **4.2.1 Configuration of the Periodic Array**

Figure 4.1 shows a solid model of a one-dimensional (1D) array assembled from five unit cells stacked end-to-end along the X axis. Each cell is identical to the one described in Chapter 3 and every two adjacent cells have two vertices in common, where at each common vertex two bars and eight strings intersect. Consequently, the resulting structure, if deemed stable, would constitute a Class-2 tensegrity according to Skelton's definition, since some vertices join two compression elements.

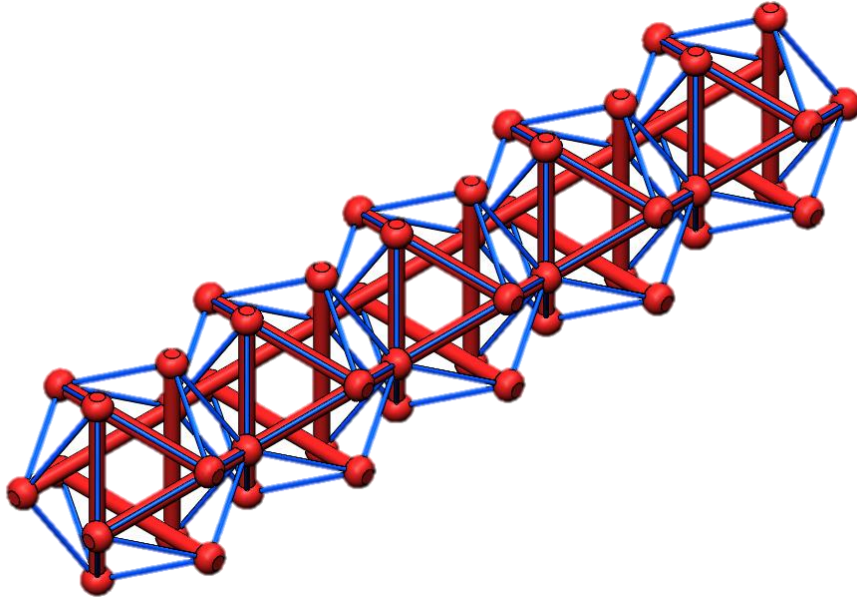


Figure 4.1 1D, class-2 array of identical icosahedron tensegrity cells

#### 4.2.2 Mechanisms and States of Self-stress

Analysis of the equilibrium matrix  $\mathbf{A}$  of a one-dimensional array of  $N$  identical tensegrity unit cells assembled end-to-end reveals that the matrix has an  $N$ -dimensional null space, indicating  $N$  states of self-stress for the structure

$$n_{ss} = N \quad (4.1)$$

A basis for the null space of  $A$  could be found in terms of the state of self-stress of the individual cell,  $\mathbf{S}_1$ , given in eq. (3.4), where each zero element is in fact a vector of thirty zeros elements:

$$\begin{bmatrix} \mathbf{S}_1 \\ \mathbf{0} \\ \mathbf{0} \\ \vdots \\ \mathbf{0} \\ \mathbf{0} \end{bmatrix}, \begin{bmatrix} \mathbf{0} \\ \mathbf{S}_1 \\ \mathbf{0} \\ \vdots \\ \mathbf{0} \\ \mathbf{0} \end{bmatrix}, \dots, \begin{bmatrix} \mathbf{0} \\ \mathbf{0} \\ \mathbf{0} \\ \vdots \\ \mathbf{0} \\ \mathbf{S}_1 \end{bmatrix}$$

The general state of self-stress can thus be thought of as a linear combination of individual cells' state of self-stress  $\mathbf{S}_1$ . This observation is important because pre-stressing the structure by loading each of its cells according to a positive multiple of  $\mathbf{S}_1$  ensures that all members of the structure are “properly” loaded, *i.e.*, compression elements in compression and tension elements in tension, which is a necessary condition in the definition of a tensegrity.

The unconstrained structure possesses  $(6 + N)$  mechanisms which, upon investigation, can be broken down into three sets:

- Six rigid body motions,
- one infinitesimal mechanism corresponding to the simultaneous expansion of every cell in the structure according to  $\mathbf{M}_1$  of eq. (3.3), and
- $(N - 1)$  finite (large displacement) mechanisms corresponding to the rotation of the second and subsequent cells about the Y axis by using their leftmost nodes as pivots.

The rigid body motions are constrained by applying the same boundary conditions of the single cell (eq. (3.7)), while the finite mechanisms are constrained by preventing the Z-displacement of either bottom node in each unit (*e.g.*, in Figure 6:  $z_{19} = z_{29} = z_{39} = 0$ ). Next, the global stiffness matrix for the structure is assembled and its eigenvalues are computed using MATLAB. We find that without pre-stress, the stiffness matrix has one eigenvalue equal to zero, confirming that the unstressed structure is not stiff due to the infinitesimal mechanism. By applying a pre-stress obtained from any linear combination of the states of self-stress, the mechanism gets stiffened and the structure becomes stable.

In conclusion, since the constrained structure admits an infinitesimal mechanism that gets stiffened under the effect of pre-stress, and since all members of the structure are properly loaded, we thus consider the resulting constrained structure to be a Class-2 tensegrity structure.

### 4.3 Static Analysis

We follow the same procedures described in Section 3.4 to compute the elastic moduli of the one-dimensional tensegrity arrays. The geometric and material properties are the same as in Table 3.1 and all cells are identically pre-stressed according to a positive multiple of  $\mathbf{S}_1$ . The same boundary conditions are used and we assume that the forces and displacements are applied to the structure through end plates, one on each of its six faces (top, bottom, left, right, front, back).

Figures 4.2-4.5 show the elastic modulus  $E$ , the shear modulus  $G_{zx}$ , the bulk modulus  $B$  and the ratio  $B/G_{zx}$ , respectively, for one-dimensional periodic arrays with different numbers of unit cells against the initial elastic strain in the strings. Figure 4.2 shows that the elastic modulus is the same as that of the individual tensegrity unit cell, which is expected since adding more units reduces the equivalent stiffness and increases the overall length by the same ratio, and that the effect of the pre-stress is negligible (less than 0.1% over the range).

Figure 4.3 shows that increasing the number of cells leads to a higher shear resistance, as evidenced by the increased shear modulus. In order to understand the effect of pre-stress on the shear modulus we compare Figure 4.3 to Figure 3.4, and note that for  $N = 2$  cells, the plot follows a similar pattern:  $G_{zx}$  increases for elastic strain values from

0.01 to 0.04, reaches a peak at 0.04 and decrease for higher strain. For  $N > 2$  cells, the shear modulus decreases monotonically, suggesting that the initial strain value corresponding to the peak shear modulus is negative.

Figure 4.4 shows that the bulk modulus is not affected by the number of cells or the pre-stress, as the resistance to compression is essentially due to the stiffness of the central bars, and we can also note that  $E \approx 3B$ . Figure 4.5 shows that the bulk-to-shear ratio has decreased compared to that of a single cell due to the increase in shear modulus, but is still very large (around 1500) compared to naturally-occurring materials.

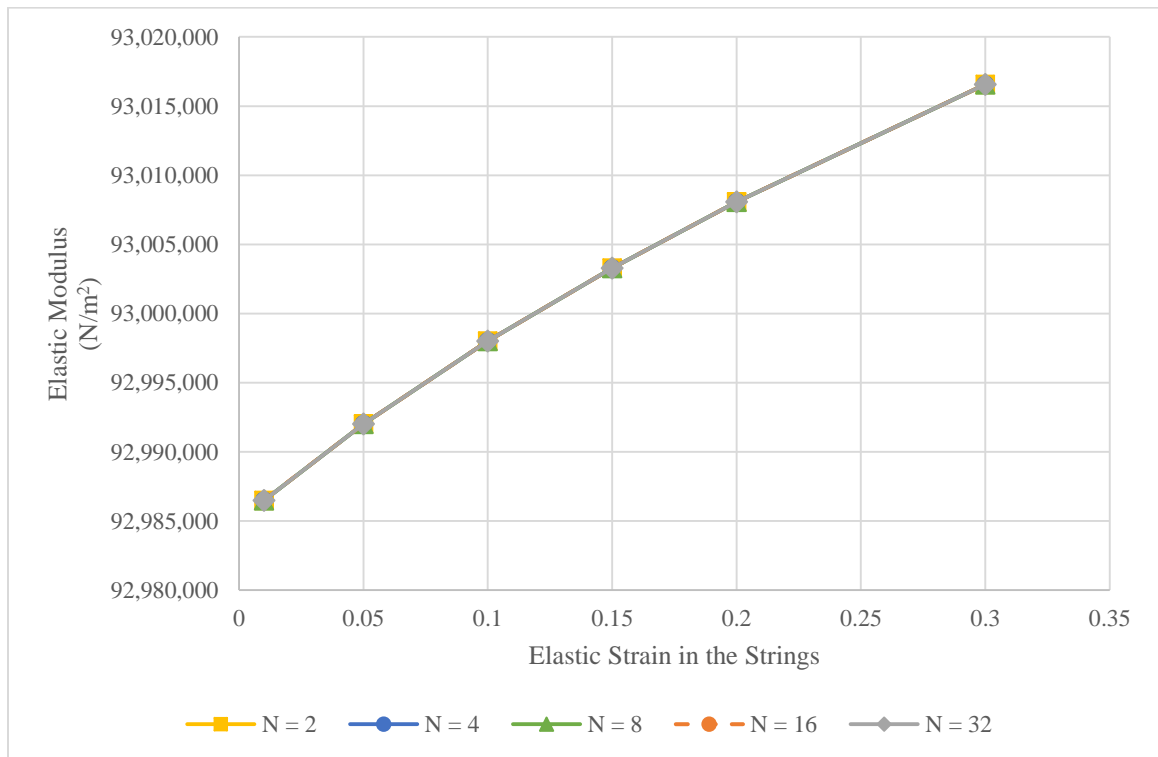


Figure 4.2 Elastic modulus of 1D, class-2 tensegrity array of repeating cells (all five lines are super-imposed)

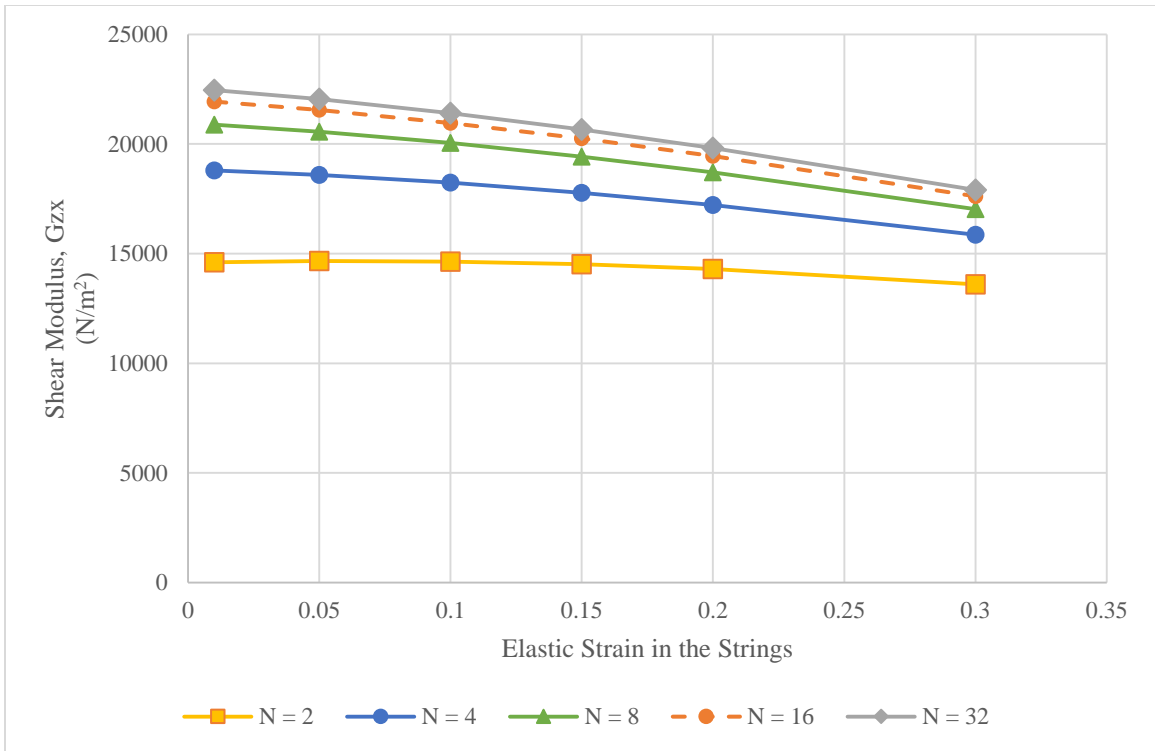


Figure 4.3 Shear modulus of 1D, class-2 tensegrity array of repeating cells

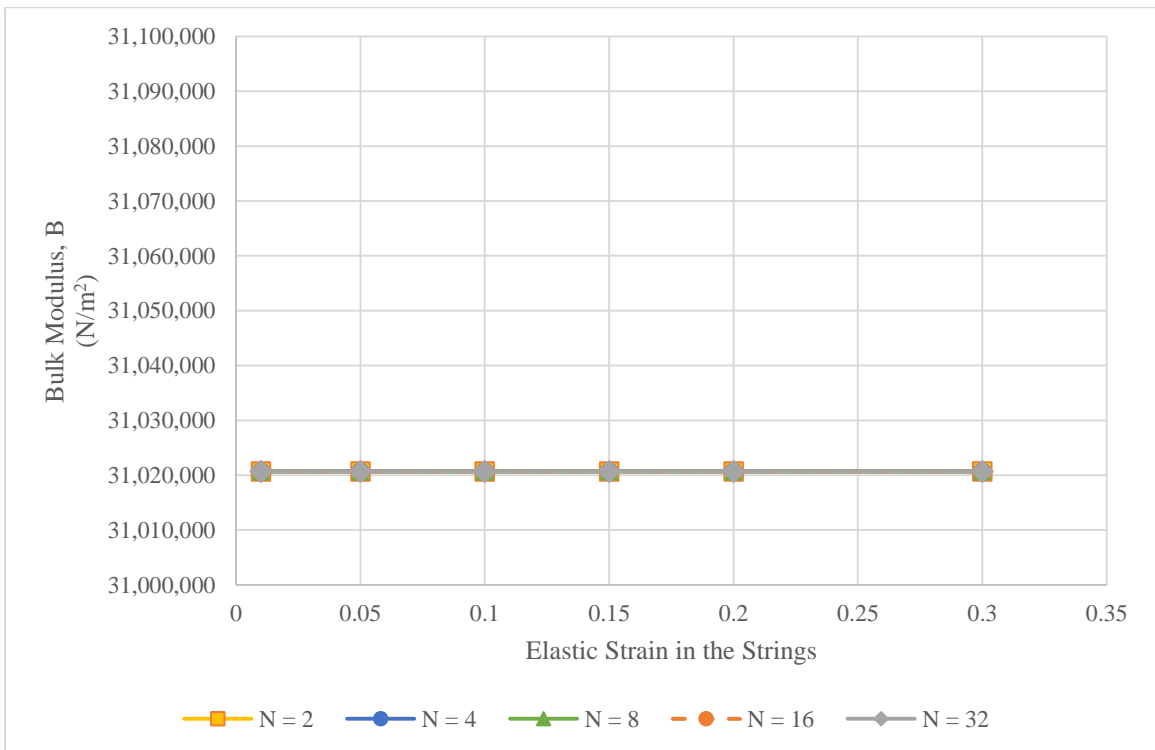


Figure 4.4 Bulk modulus of 1D, class-2 tensegrity array of repeating cells (all five lines are super-imposed)

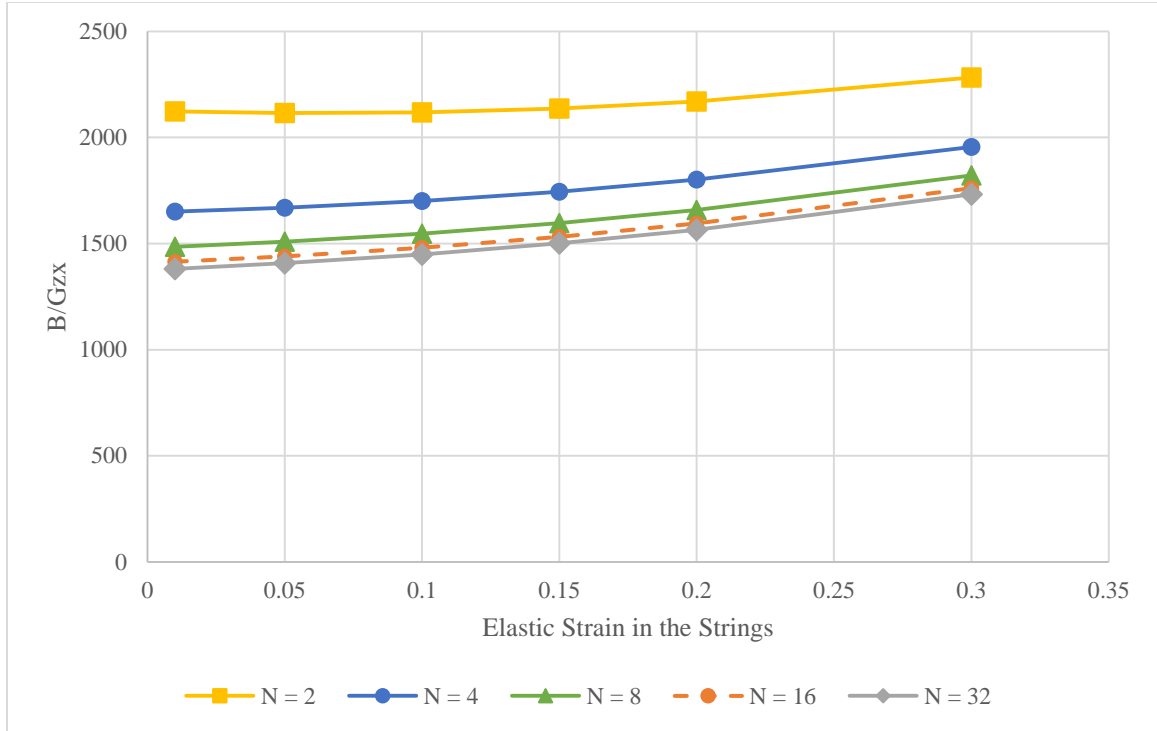


Figure 4.5 Bulk-to-shear ratio of 1D, class-2 tensegrity array of repeating cells

#### 4.4 Dynamic Analysis of 1D Tensegrity Array

We investigate the dynamics of infinite periodic tensegrity structures using the wave approach, often referred to as Bloch's theorem, by considering only the repeating unit cell. We first explain the method, then apply it to the one-dimensional array of repeating icosahedron tensegrity cells.

##### 4.4.1 Overview of Bloch's Theorem

Bloch's Theorem as applied to periodic structure, *e.g.*, by [86, 87, 104], stipulates that a wave propagating through an infinite lattice of repeating unit cells will incur a change in its amplitude as it travels from one cell to the next, and that this change is independent of the cell's location within the lattice. This makes it possible to capture the dynamics of



wave propagation in the lattice by considering the dynamic response of only one cell with the appropriate boundary conditions, which will be explained below.

Without loss of generality, we assume a beam of infinite length with periodic changes in its geometry, material properties, or both. A cross-section along the length of a portion of the beam is shown in Figure 4.6(a), where the change in size is representative of the periodicity. The repeating unit cell is shown in Figure 4.6(b).

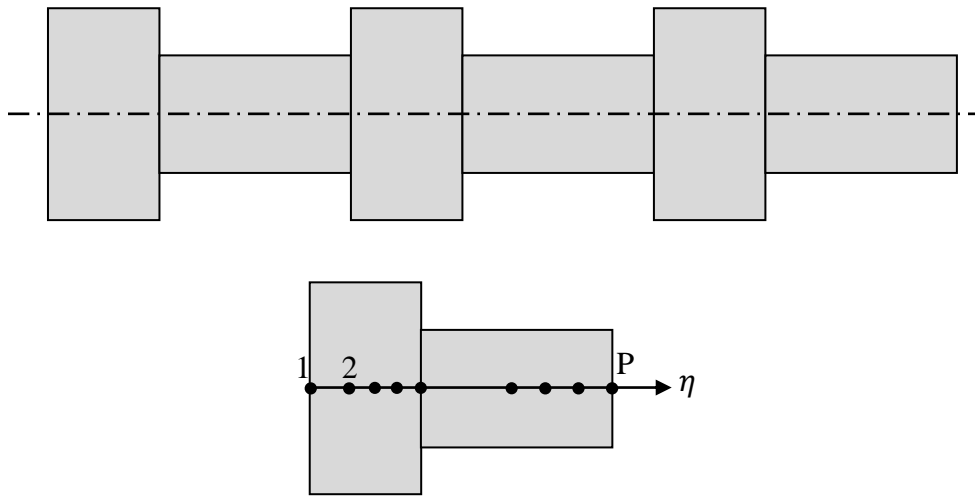


Figure 4.6 (a) Lengthwise section of periodic beam and (b) unit cell

Assuming a local coordinate  $\eta$  within each cell, then according to Bloch's theorem, a wave propagating along the beam will satisfy the relationship

$$W(\eta, N_1, \omega, t) = W(\eta, \omega, t) e^{N_1 \mu} \quad (4.2)$$

where  $W(\eta, \omega, t)$  is the wave amplitude in an arbitrarily-chosen reference unit cell,  $W(\eta, N_1, \omega, t)$  is the wave amplitude in a different cell that is offset by  $N_1$  cells from the reference cell, and  $\mu$  is the propagation constant which determines the relative change in wave amplitude from one cell to the next. The propagation constant is, in general, a complex number, *i.e.*,

$$\mu = \alpha + i\beta \quad (4.3)$$

where  $\alpha$  is the attenuation constant, while  $\beta$  is the phase constant. When the attenuation constant is zero, any incident wave on the beam will be transmitted from one cell to the next without attenuation, only undergoing a phase change (in the spatial domain). A wave with this attribute is said to lie in the pass band of the structure. When, on the other hand, the attenuation constant is nonzero, the amplitude of the wave will decay as it propagates. Such a wave is said to lie in the stop band of the structure, where waves are unable to propagate freely.

In order to investigate the dynamics of the beam, we begin by analyzing the unit cell. Using the finite element method, we discretize the unit cell into  $(P - 1)$  two-node beam elements, resulting in  $P$  nodes. Each nodes admits two degrees of freedom: translation along the vertical axis,  $w_i$ , and rotation about the out-of-plane axis,  $\theta_i$ . After assembling the mass and stiffness matrices, we can write the equation of motion of the unit cell in matrix form:

$$\mathbf{M}\ddot{\mathbf{q}} + \mathbf{K}\mathbf{q} = \mathbf{F} \quad (4.4)$$

where  $\mathbf{F}$  is the vector of nodal forces and moments,  $\mathbf{q}$  is the vector of nodal degrees of freedom of the cell, and  $\ddot{\mathbf{q}}$  is the second derivative, with respect to time, of  $\mathbf{q}$ .

$$\mathbf{q} = [\mathbf{q}_1 \quad \mathbf{q}_2 \quad \cdots \quad \mathbf{q}_P]^T \quad (4.5)$$

where each  $\mathbf{q}_i$  is the vector of degrees of freedom of the  $i^{th}$  node, which, in the case of the two-dimensional beam, is given by

$$\mathbf{q}_i = [w_i \quad \theta_i]^T \quad (4.6)$$

Assuming a harmonic wave propagating through the beam with angular velocity  $\omega$ ,  $\ddot{\mathbf{q}}$  can be replaced by  $-\omega^2\mathbf{q}$ , and the equations of motion can be re-written as

$$(\mathbf{K} - \omega^2\mathbf{M})\mathbf{q} = \mathbf{F} \quad (4.7)$$

Since the rightmost node ( $P$ ) of the cell is also the leftmost node of the following cell, Bloch's theorem requires that as the wave travels between nodes 1 and  $P$  (two similar nodes in two consecutive cells), its magnitude will undergo a change dictated by the propagation constant and can be expressed by the equation

$$\mathbf{q}_P = \mathbf{q}_1 e^{\mu} = \mathbf{q}_1 e^{\alpha+i\beta} \quad (4.8)$$

Equation (4.8) is known as the Floquet boundary condition [87] and flows from direct substitution in eq. (4.2) with  $\eta = 0$  and  $N_1 = 1$ , and with the time-dependent term simplified from the equation.

We can thus define a vector of reduced degrees of freedom,  $\mathbf{q}^R$ ,

$$\mathbf{q}^R = [\mathbf{q}_1 \quad \mathbf{q}_2 \quad \cdots \quad \mathbf{q}_{P-1}]^T \quad (4.9)$$

which is related to  $\mathbf{q}$  by the equation

$$\mathbf{q} = \mathbf{T} \mathbf{q}^R \quad (4.10)$$

where  $\mathbf{T}$  is a transformation matrix parametrized by  $\mu$ . Substituting back into the equation of motion, we get:

$$\mathbf{MT}\ddot{\mathbf{q}}^R + \mathbf{KT}\mathbf{q}^R = \mathbf{F} \quad (4.11)$$

Pre-multiplying both sides of the equation by  $\mathbf{T}^H$  (the conjugate transpose of  $\mathbf{T}$ ) yields

$$\mathbf{T}^H \mathbf{M} \mathbf{T} \dot{\mathbf{q}}^R + \mathbf{T}^H \mathbf{K} \mathbf{T} \mathbf{q}^R = \mathbf{T}^H \mathbf{F} \quad (4.12)$$

It was shown [124] that the product on the right hand side of the equation reduces to zero, which allows the equation of motion to be re-written as

$$(\tilde{\mathbf{K}} - \omega^2 \tilde{\mathbf{M}}) \mathbf{q}^R = \mathbf{0} \quad (4.13)$$

where  $\tilde{\mathbf{K}}$  and  $\tilde{\mathbf{M}}$  are both functions of the propagation constant  $\mu$ , and are given by

$$\begin{aligned} \tilde{\mathbf{K}} &= \mathbf{T}^H \mathbf{K} \mathbf{T} \\ \tilde{\mathbf{M}} &= \mathbf{T}^H \mathbf{M} \mathbf{T} \end{aligned} \quad (4.14)$$

Equation (4.13) takes the form of an eigenvalue problem parametrized by the propagation constant. A common approach in the search for stop and pass bands is to set the attenuation constant to zero, resulting in  $\mu = i\beta$ , and solve the eigenvalue problem for different values of the phase constant within the range  $0 \leq \beta \leq 2\pi$ . This results in the angular velocities  $\omega$  of the waves that would be able to propagate without attenuation for every possible propagation constant. The results are graphically presented in the form of dispersion curves: a plot of the wave frequency against the propagation constant or the phase constant. Stop bands are the frequency ranges not associated with any purely imaginary propagation constant, and will appear as empty regions on the dispersion diagram.

In the case of two-dimensional lattices obtained from the translation of a reference unit cell along two linearly independent (but not necessarily orthogonal) axes, the analysis is essentially the same, with the caveat that a propagating wave will have two independent propagation constants (*e.g.*,  $\mu_1$  and  $\mu_2$ ), resulting in dispersion *surfaces* and pass and stop bands that are a function of the propagation direction of the wave.

#### 4.4.2 Pass and Stop Bands of 1D Tensegrity Lattice

We now apply Bloch's theorem to the analysis of a one-dimensional array of repeating icosahedron tensegrity unit cells. A portion of the infinite array is shown in Figure 4.1, while the reference unit cell is the same one shown in Figure 3.1. All the cell properties are as described in Table 3.1 and all the strings are pre-stressed with an initial elastic strain of 0.05. After assembling the mass and stiffness matrices of the unit cell (each matrix has 36 rows and 36 columns), we apply the Floquet boundary conditions obtained from the periodicity of the array:

$$\begin{aligned}\mathbf{q}_3 &= \mathbf{q}_1 e^{\mu} = \mathbf{q}_1 e^{\alpha+i\beta} \\ \mathbf{q}_4 &= \mathbf{q}_2 e^{\mu} = \mathbf{q}_2 e^{\alpha+i\beta}\end{aligned}\tag{4.15}$$

where  $\mathbf{q}_i$  is the vector of degrees of freedom at node  $i$ , given by  $\mathbf{q}_i = [x_i \ y_i \ z_i]^T$ . The reduced set of degrees of freedom,  $\mathbf{q}^R$ , thus consists of 30 elements.

Setting the attenuation constant  $\alpha$  equal to zero, and solving the eigenvalue problem (eq. (4.13)) for the angular velocities  $\omega$  corresponding to phase constants in the range  $0 - 2\pi$  yields the dispersion curves of the structure, the first six of which are shown in Figure 4.7. From the plot we can see that for any given frequency, there correspond waves with purely imaginary propagation constants which will propagate at that frequency without attenuation. There are no stop bands – frequency ranges that are not associated with waves. Intuitively, this is to be expected, due to the continuity and uniformity of the center two struts along the array, which seem to provide a continuous medium for a disturbance of any given frequency to propagate unimpeded along the structure.

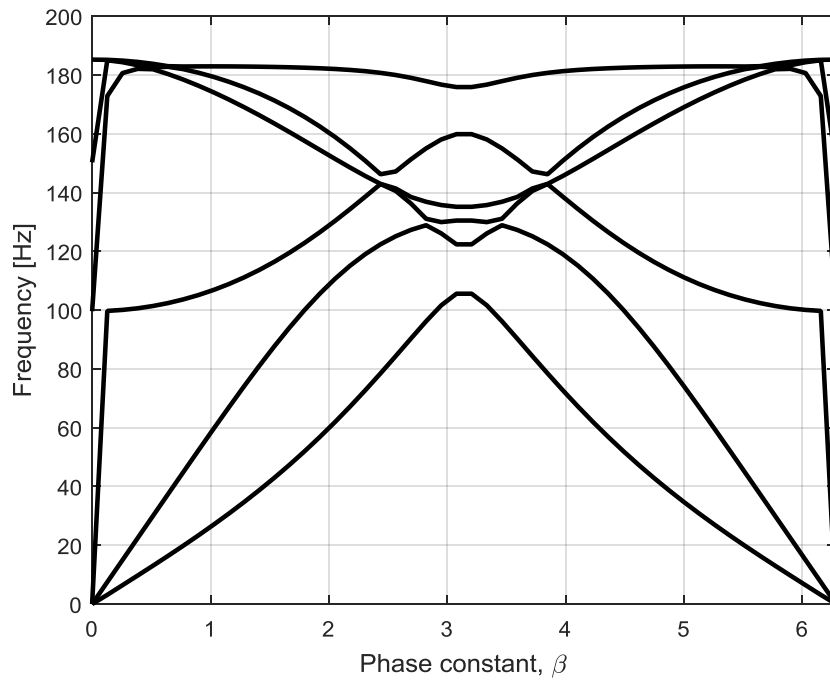


Figure 4.7 Dispersion curves of 1D, class-2 tensegrity array of repeating cells

## 4.5 Experimental Verification

### 4.5.1 Prototype Description

Figure 4.8 shows a 3D-printed prototype of the 1D array consisting of four icosahedron tensegrity cells stacked end-to-end. The structure was built as one part from a solid model file on the same 3D printer and using the same materials (VeroWhite Plus and FLX 9870-DM) and dimensions as the unit cell in Section 3.5.

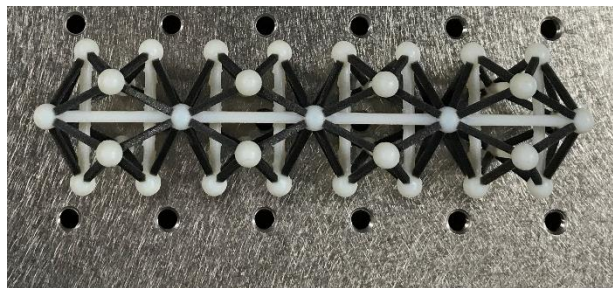


Figure 4.8 Icosahedon 1D array

#### 4.5.2 Determination of Shear Modulus

Figure 4.9 depicts the experimental setup used in the determination of the shear modulus. The array rests on a bottom plate that is fully constrained to the foundation and which incorporates small indentations to seat the spherical bar ends, constraining their translation while allowing them to rotate. A similar plate fits on the top of the array and is attached, via a connecting link and an end-plate, to an electromagnetic shaker (LDS V408), the signal to which is generated using signal generator/analyzer (Stanford Research SRS-780) and amplified using the LDS PA100E amplifier. A Force sensor (PCB Piezotronics, Model 208M51<sup>5</sup>) fits between the shaker and the face plate and measures the force applied by the shaker, while a laser sensor (Matsushita NAIS LM200 ANL2534A<sup>6</sup>) measures the position of the top plate.

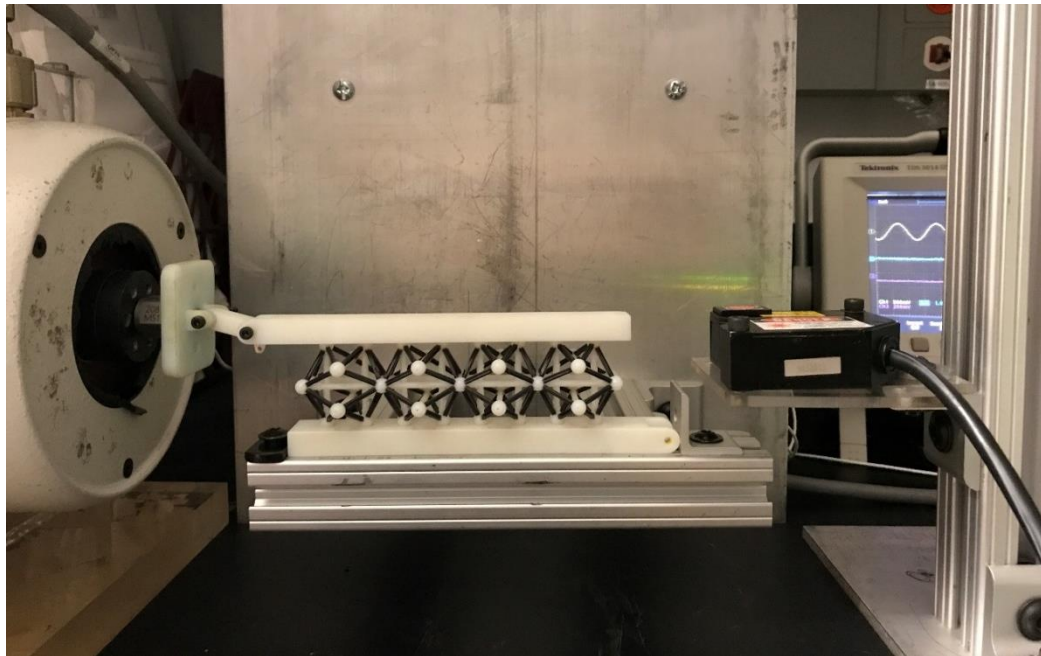


Figure 4.9 Array shear test setup

<sup>5</sup> S/N: 16128 – Sensitivity: 2.54 mV/N

<sup>6</sup> Sensitivity: 0.5 V/mm

In order to determine the shear modulus, we apply a shear displacement and measure the shear force. To that end, a sinusoidal input signal is supplied to the shaker, rocking the top plate back and forth and causing shearing of the tensegrity array. Figure 4.10 shows the measured force against the displacement of the top plate, indicating a shear stiffness of approximately  $1,040 \text{ N/m}$ , consequently, and with knowledge of the area the force is acting on and the initial length of the array, we can compute the shear modulus to be  $8,145 \text{ N/m}^2$ . The hysteresis is representative of the energy dissipated as a result of the viscoelastic nature of the flexible, rubber-like material. A finite element model of the array predicts a shear stiffness of  $993 \text{ N/m}$  and a corresponding shear modulus of  $7,773 \text{ N/m}^2$ , which suggests a very good agreement (within 5%) between the model and the experiment.

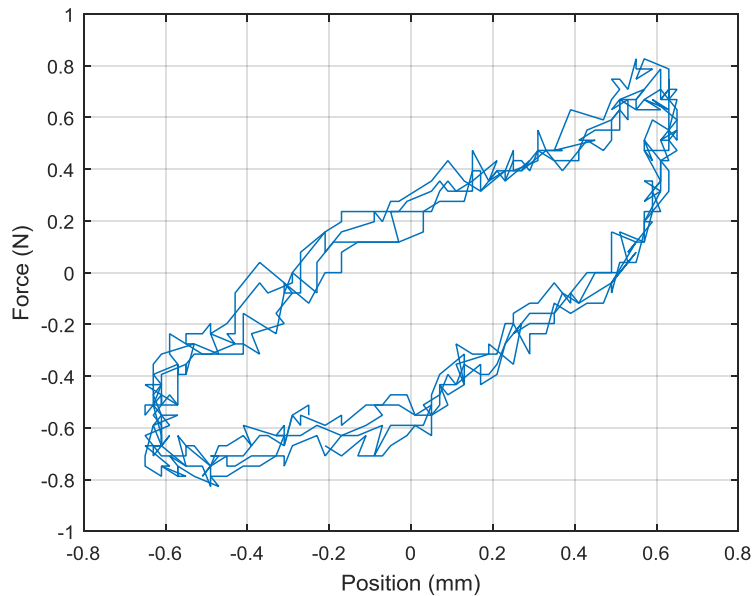


Figure 4.10 Shear force against displacement – 1D array



### 4.5.3 Determination of Elastic Modulus

The elastic modulus is determined by means of a compression test carried out using the experimental setup shown in Figure 4.11. The array is located on a base plate secured to the foundation and rests from the left against an end-plate attached to the shaker. A stationary end-plate on the right side constrains the axial translation of the structure. All plates are made by Newport Corporation, and additional plates (not shown) are added on the top, front and back of the array to constrain lateral deformation of the structure. Each plate prevents “outward” motion normal to its plane, while allowing rotation and in-plane translation.

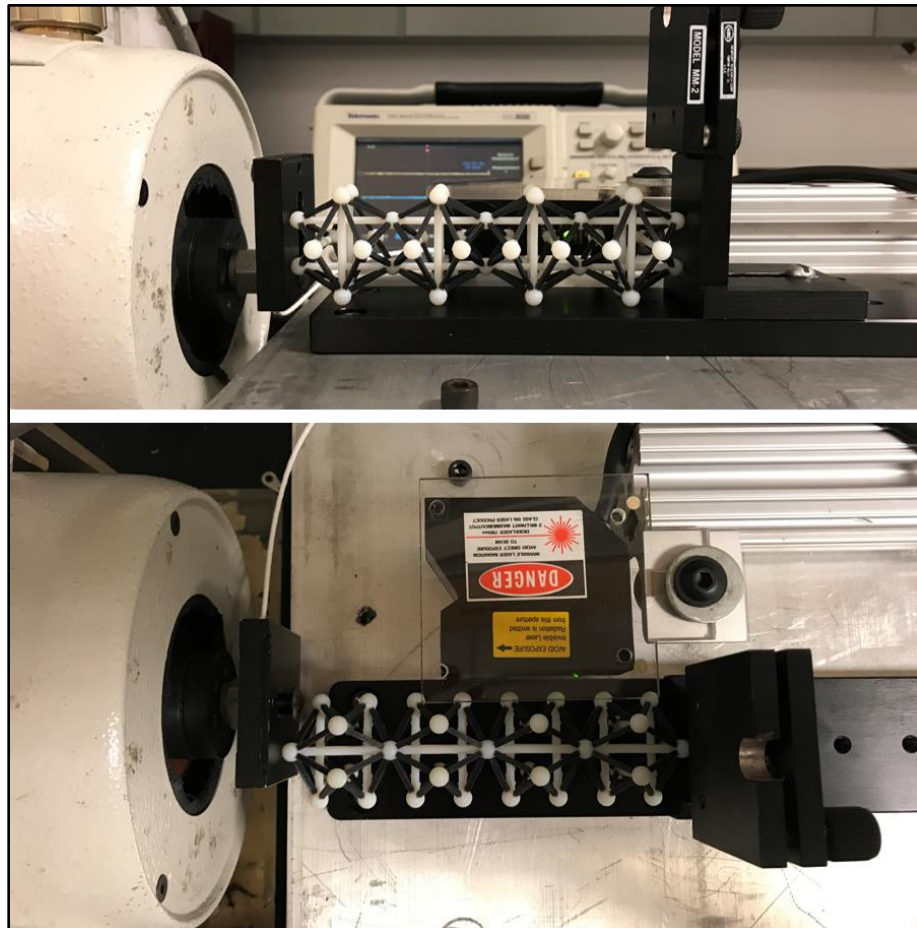


Figure 4.11 Array compression test setup. Front and top views

As the shaker and the end-plate attached to it compress the structure, the force sensor, located between the shaker and the end-plate, measures the force exerted on it while the laser sensor measures the position of the moving end-plate. Figure 4.12 shows the raw output of both sensors showing a peak in the force as the structure is compressed (a higher voltage signifies higher compression for the force sensor and the shaker moving away from the structure for the position sensor). As the shaker moves away from and loses contact with the structure, the force drops to its baseline value.

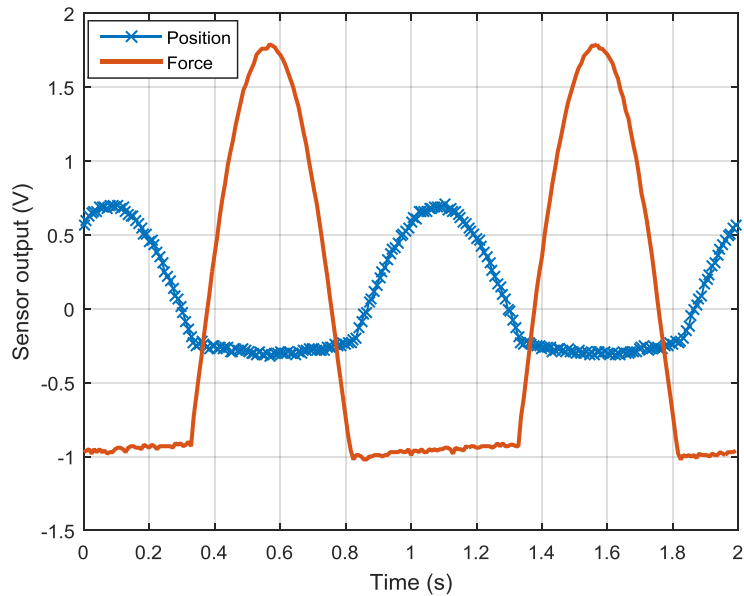


Figure 4.12 Compression test – sensors' output

Figure 4.13 shows the compressive force against the position of the end-plate, from which we can extract the equivalent stiffness of the structure as the slope of the curve (of the right portion, corresponding to the half-cycles where the shaker is compressing with the structure), which we calculate to be approximately  $60,000 \text{ N/m}$  and which corresponds to an elastic modulus of  $E_{xx} = 7.5 \text{ MPa}$ . The curve does not show any hysteresis, which is expected since the stiffness is primarily due to the longitudinal rigid

bars and not the viscoelastic flexible elements. The corresponding finite element model predicts a stiffness of  $66,000\text{ N/m}$ , indicating good agreement with the experimental result. Deviations between the modelled and experimental results – as discussed in Section 3.6.3 – may be due to misalignment or rotation of the long bars during loading, and/or production imperfections.

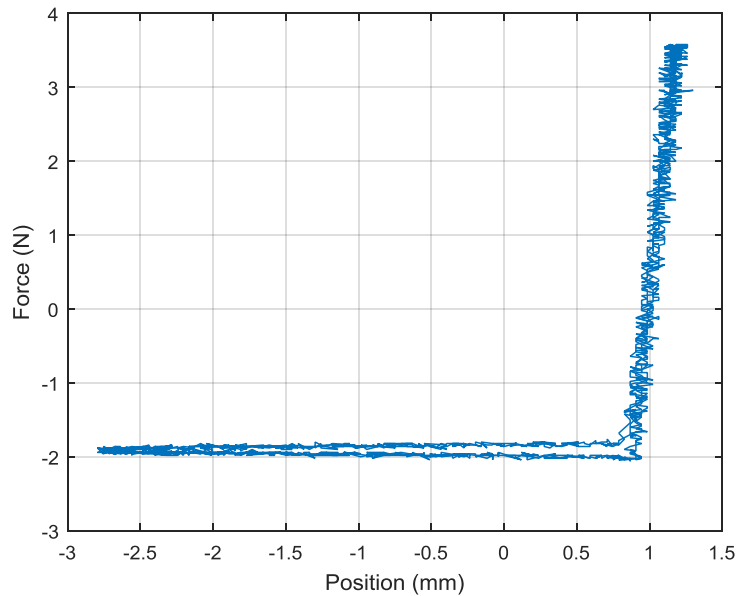


Figure 4.13 Compression test – Force against deformation

#### 4.5.4 Impedance Tube Testing

The interaction of the tensegrity array with incident sound waves is investigated using the acoustic transfer matrix method [177] using the ACUPRO Measurement System from Spectronics, Inc. which consists of an impedance tube coupled to a transmission loss tube, with the attached speaker and microphones, shown schematically in Figure 4.14 (the numbers indicate microphone placements).

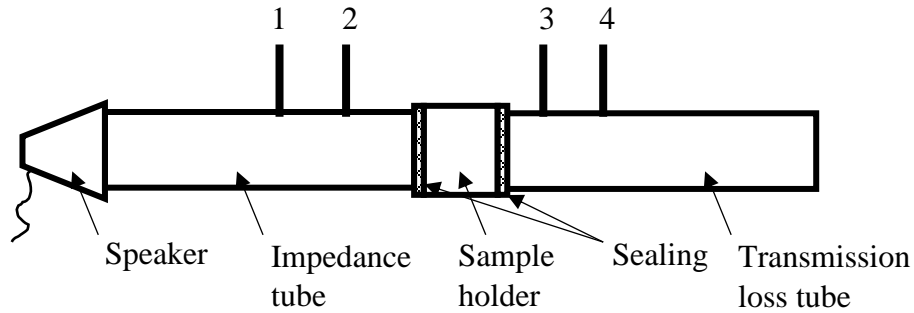


Figure 4.14 Schematic drawing of acoustic test setup

With the test sample mounted in the sample holder (Figure 4.15), a sound wave is generated at one end of the dense, rigid tube using the speaker (JBL 2126J), while two microphones (Larson Davis PRM908) measure – interchangeably – the sound levels at four locations along the tube, two on each side of the sample. A MATLAB program was created to calculate the acoustic transfer matrix from the measured signals and transfer functions according to the ASTM E2611 standard procedure [178], from which the transmission coefficient, transmission loss, and other acoustic properties of the sample may be extracted.

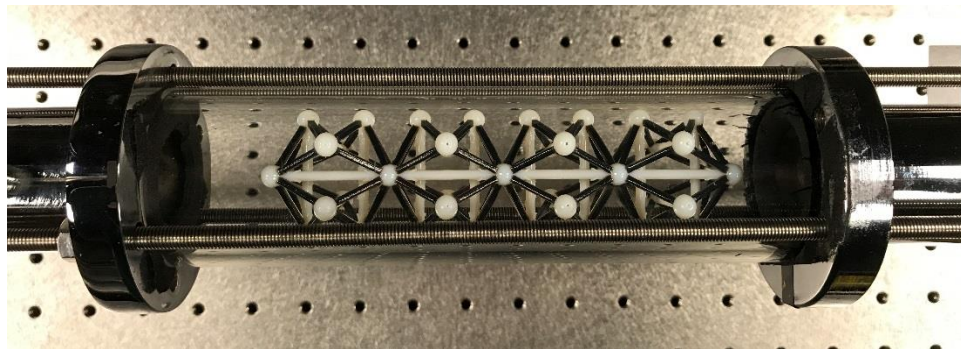


Figure 4.15 Tensegrity array in impedance tube

Figure 4.16 shows the calculated transmission coefficient,  $t$ , defined as the ratio of the sound pressure level transmitted by the specimen to that incident on it, comparing the one for the array to that of an empty portion of the tube. It can be seen that the two plots

are very similar, indicating that the structure does not play any role in attenuating the sound waves incident on it, which was expected from the Bloch analysis yielding no frequency stop bands.

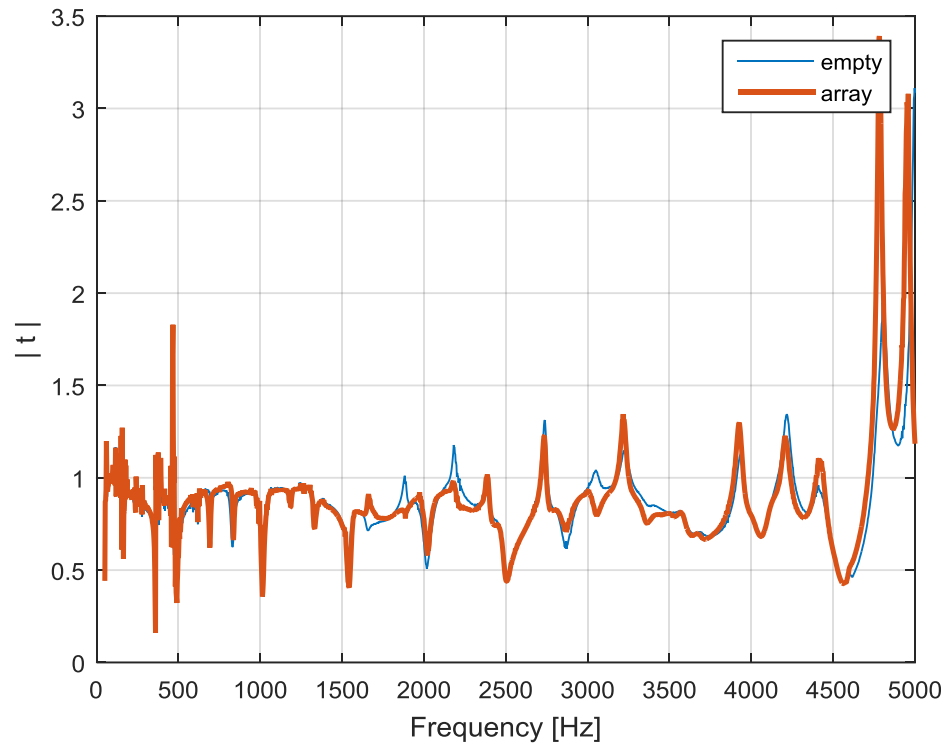


Figure 4.16 Transmission coefficient of tensegrity array

## 4.6 Icosahedron Tensegrity Beams

A potential application for one-dimensional tensegrity arrays is their use as beams to support bending loads. For the simplest configuration examined in the previous section, this would be impossible due to the finite mechanisms that had to be constrained. However, by providing additional connecting elements, it may be possible to eliminate the mechanisms and for the array to withstand transverse loading.

### 4.6.1 Description

The beam is created by joining the tensegrity cells end-to-end and using two additional massless strings – one at the top and the other at the bottom – to connect every two adjacent cells, thus providing the bending stiffness. The connecting strings have a length  $l_c \left( = \frac{l_b}{2} \right)$  and a stiffness  $K_c$ . Figure 4.17 shows an array of four tensegrity cells, with only the bars and the connecting strings drawn.

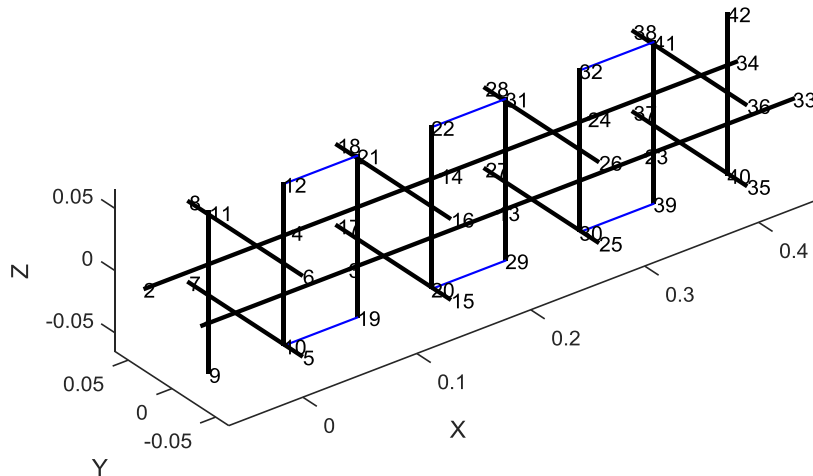


Figure 4.17 Inter-cell connectivity strings of tensegrity beam

### 4.6.2 Mechanisms and States of Self-stress

Analyzing the rank and nullspaces of the equilibrium matrix of the resulting structures, we find that a one-dimensional array of  $N$  cells has six mechanisms, namely the rigid body motions, and  $(2N - 2)$  independent states of self-stress.  $N$  of those states correspond to each cell being loaded according to  $\mathbf{S}_1$  with the connecting strings unloaded. While pre-stressing the structure according to any of the  $N$  states of self-stress will increase its stiffness, we note that the structure is always stable (with or without pre-stress). This class of kinematically determinate and statically indeterminate structures were named *redundant structures* by Murakami and Nishimura [48], and were classified as tensegrity structures by Motro (*e.g.*, [25]) and Skelton (*e.g.*, [23]). Therefore, we classify the structure as a Class-2 tensegrity.

### 4.6.3 Bending Stiffness of the Beam

We conceive cantilever tensegrity beams of different lengths by connecting the cells as described above along the X-axis, fixing all but the two rightmost nodes of the first (leftmost) cell and apply a downward force  $F_b$  on the top-right node of the rightmost cell. The downward deflection  $\Delta_b$  of the same node is calculated numerically using MATLAB and the bending stiffness  $K_b$  is computed from

$$K_b = \frac{F_b}{\Delta_b} \quad (4.16)$$

We investigate the effect of the number of cells, the stiffness of the connecting strings and the pre-tension in the internal strings of the tensegrity on the bending stiffness. The results are shown in Figure 4.18 for  $K_c = 5,000$  N/m, and Figure 4.19 for  $K_c = 20,000$  N/m.

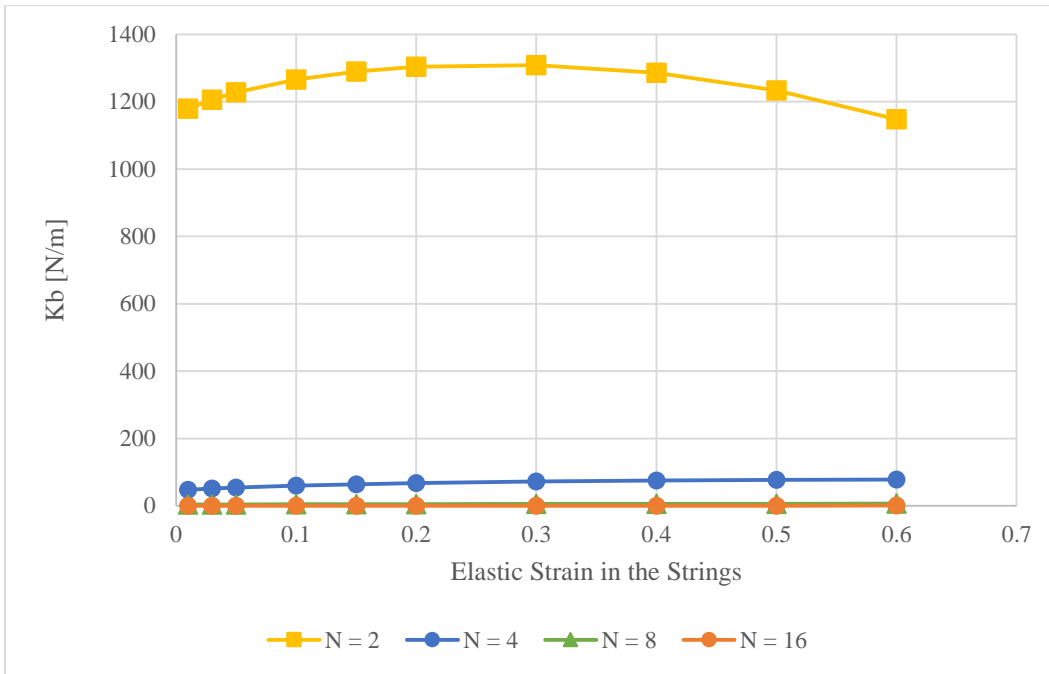


Figure 4.18 Bending stiffness of tensegrity beam ( $K_c = 5,000 \text{ N/m}$ )

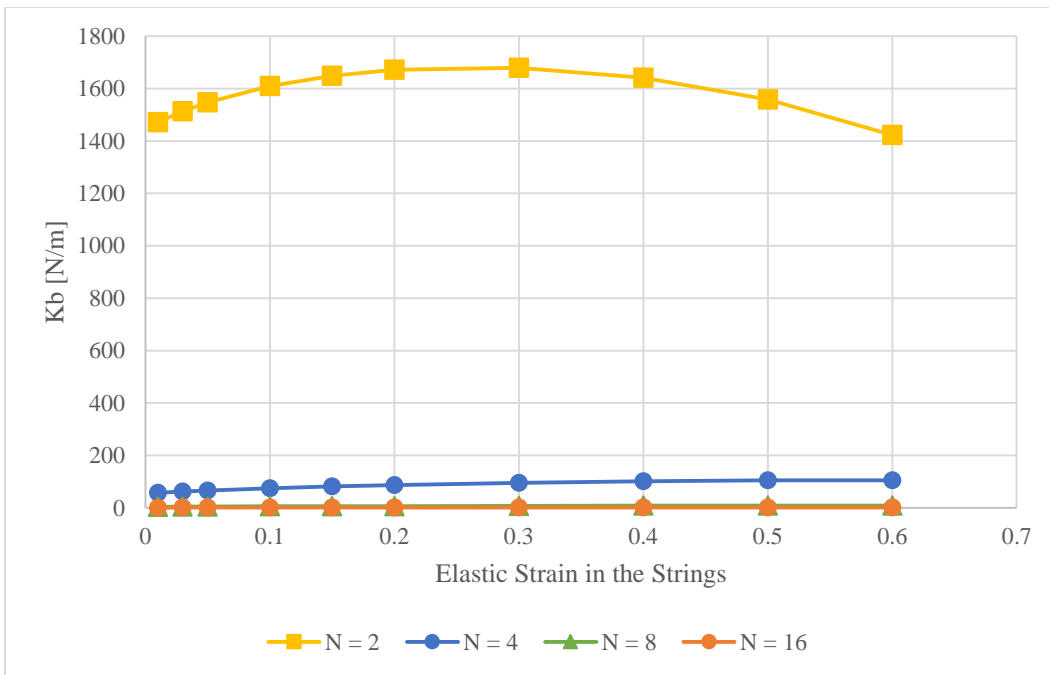


Figure 4.19 Bending stiffness of tensegrity beam ( $K_c = 20,000 \text{ N/m}$ )



## 4.7 Two-dimensional Icosahedron Tensegrity Arrays

### 4.7.1 Configuration and Description

We assume a two-dimensional array created by tessellating the icosahedron tensegrity unit cell along the global X and Y axes. The array consists of  $N_X$  cells along the X-axis and  $N_Y$  cells along the Y-axis. All the cells are identical and as described in Chapter 3 (Table 3.1).

### 4.7.2 Mechanisms and States of Self-stress

Investigating the rank and null spaces of the equilibrium matrix  $A$  of the two-dimensional periodic array reveals that, similar to the one-dimensional array, the structure has  $(6 + N_X)$  mechanisms, classified as follows:

- Six rigid body motions,
- one infinitesimal mechanism corresponding to the simultaneous expansion of every cell in the structure according to  $M_1$  (eq. (3.3)), and
- $(N_X - 1)$  finite (large displacement) mechanisms corresponding to the rotation of the second and subsequent columns of cells about the Y axis by using their leftmost nodes as pivots.

The number of states of self-stress,  $n_{SS}$ , is found to satisfy the empirical relationship

$$n_{SS} = 6N_XN_Y - 5N_X - 6N_Y + 6 \quad (4.17)$$

where  $N_X, N_Y \geq 1$ . Of those  $n_{SS}$  states,  $N_XN_Y$  states correspond to each cell being stressed in accordance with state  $S_1$ , with the bars in equal compression and the strings in equal tension.

Assembling the global stiffness matrix of a two-dimensional array reveals that the unstressed structure is not stiff (one eigenvalue is zero). However, while applying any linear combination of the aforementioned  $N_X N_Y$  states of self-stress leads to a stiff structure. We hence conclude that the array is a Type-2 tensegrity structure.

### 4.7.3 Static Analysis

We proceed to analyze the elastic moduli for the two-dimensional array following the same procedure outlined in the previous chapter. For all simulations, the geometric and material constants are as given in Table 3.1. The structure is pre-stressed such that all strings have the same initial tension ( $T_0 = f_s l_s = K_s \varepsilon_0 l_s$ ) and, according to the state of self-stress  $\mathbf{S}_1$ , all bars have the same initial compression  $-\frac{3}{2}T_0$ . The initial strain in the string is varied to investigate its effect on the elastic moduli.

#### 4.7.3.1 Modulus of Elasticity

The modulus of elasticity is calculated by applying uni-axial tensile loading conditions along the corresponding axis and calculating the resulting elongation of the structure using Finite Element analysis, followed by calculating the modulus using equation (3.11). The moduli are computed for different array sizes and pre-tension values of the internal strings. The first observation we make is that for a given pre-stress value, all three moduli of elasticity ( $E_{xx}, E_{yy}, E_{zz}$ ) are equal. Figure 4.20 additionally shows that the stiffening effect of the initial pre-stress is very small, which is to be expected since the stiffness is primarily due to the rigidity of the bars. Moreover, the modulus of elasticity does not change with the array size, and its value of approximately  $9.3 \times 10^7 N/m^2$  is in fact very close to those of the single cell and the one-dimensional array.

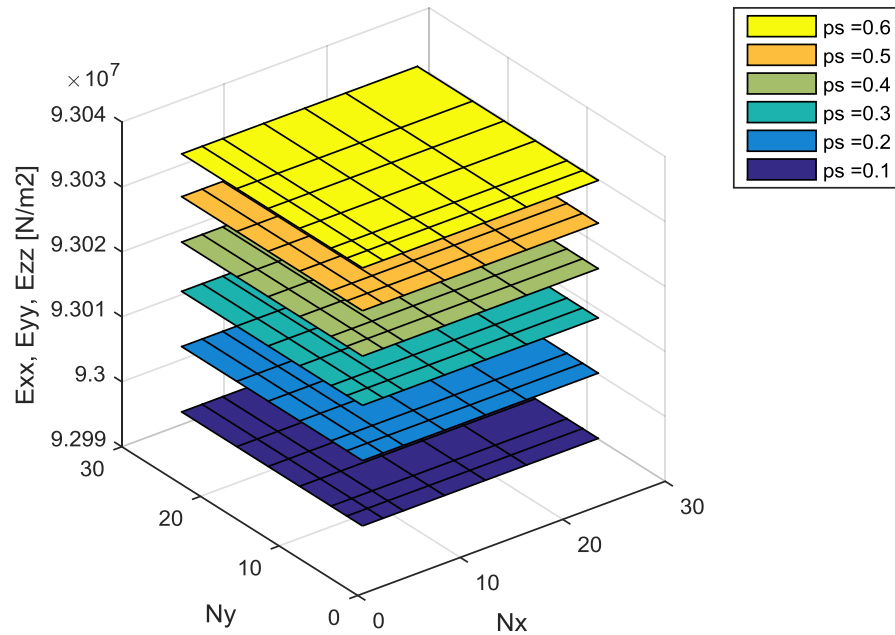


Figure 4.20 Elastic moduli of 2D, class-2 tensegrity array of repeating cells

#### 4.7.3.2 Shear Moduli $G_{zx}$ and $G_{zy}$

The shear moduli are calculated in the same way as in Section 3.4: imposing a prescribed displacement on the top nodes (along the X-axis and the Y-axis, respectively), and calculating the resulting forces and the corresponding shear modulus. Figure 4.21 and Figure 4.22 show  $G_{zx}$  and  $G_{zy}$ , respectively, for different array sizes and pre-tension values. It can be seen that the shear modulus increases as the number of units along the shearing direction increases. Moreover, increasing the pre-stress reduces the shear moduli, which is generally consistent with the results of the one-dimensional arrays. Both shear moduli are on the order of  $10^4 \text{ N/m}^2$ . The figures also demonstrate the anisotropy of the two-dimensional arrays.

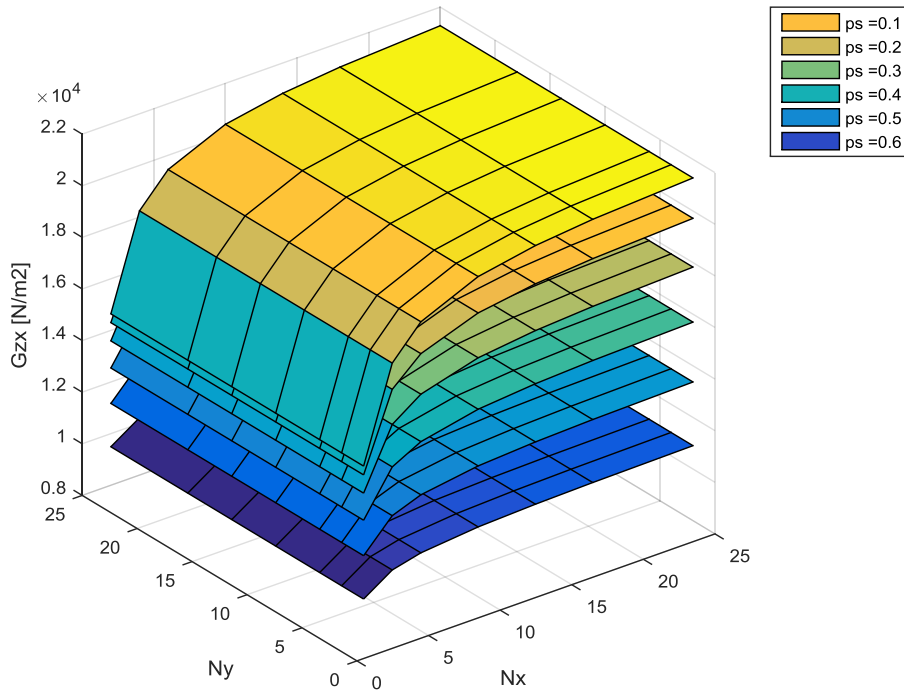


Figure 4.21 Shear modulus,  $G_{zx}$ , of 2D, class-2 tensegrity array of repeating cells

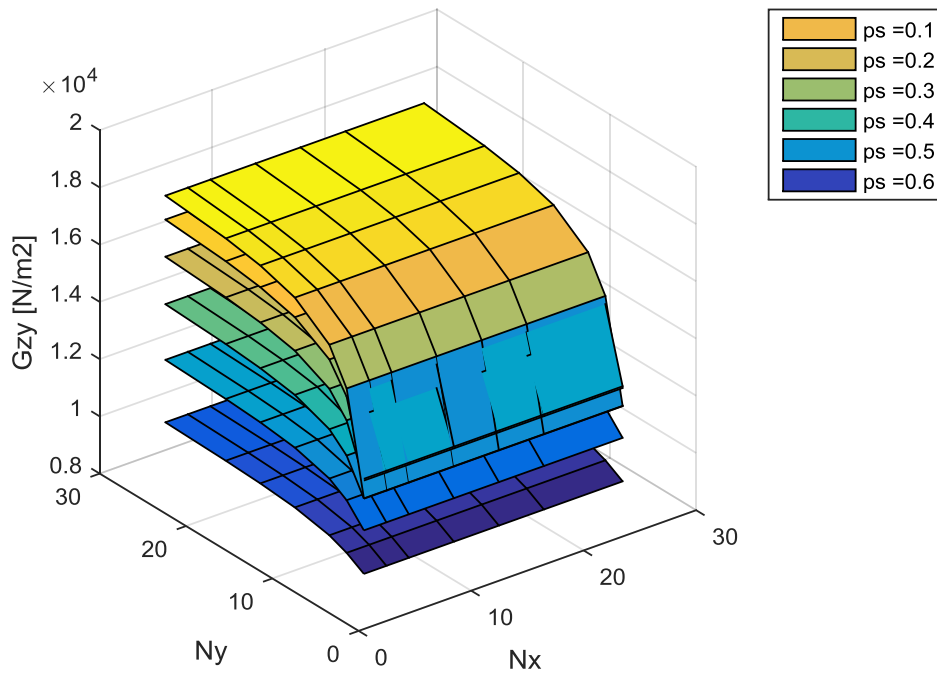


Figure 4.22 Shear modulus,  $G_{zy}$ , of 2D, class-2 tensegrity array of repeating cells

### 4.7.3.3 The Bulk Modulus (B)

The bulk modulus is calculated in the same way as in Section 3.4: applying a hydrostatic pressure on all faces of the two-dimensional array and numerically calculating the resulting change in volume of the structure and the corresponding bulk modulus. The bulk modulus was found to be independent of both the array size and the pre-stress multiplier, with an approximate value of  $3.1 \times 10^7 N/m^2$ .

Finally, we observe that the bulk-to-shear ratio is on the order of  $10^3$ , similar to that of the individual tensegrity, which seems promising for the potential use of two-dimensional structures as pentamode metamaterials.

## 4.8 Dynamic Analysis

In this section we apply Bloch's theorem to investigate the propagation of waves through infinite two-dimensional tensegrity arrays and determine the location and width of stop bands, if they exist.

The unit cell is the same one shown in Figure 3.1. The array is obtained by tessellating the unit cell by a distance  $l_b$  along the X and Y axes. The origin of the coordinate system is assumed to lie at the centroid of an arbitrarily chosen reference cell. Therefore, the position vector of any point in the lattice,  $\vec{\mathbf{R}}$ , can be expressed as:

$$\vec{\mathbf{R}} = \vec{\mathbf{r}} + N_1 \vec{\mathbf{e}}_1 + N_2 \vec{\mathbf{e}}_2 \quad (4.18)$$

where  $\vec{\mathbf{r}}$  is the position vector of the equivalent point in the reference unit cell,  $\vec{\mathbf{e}}_1$  and  $\vec{\mathbf{e}}_2$  are the (direct) lattice vectors (which, in this case, are:  $\vec{\mathbf{e}}_1 = l_b \hat{\mathbf{e}}_X$  and  $\vec{\mathbf{e}}_2 = l_b \hat{\mathbf{e}}_Y$ ), and  $N_1$

and  $N_2$  are the offset (in number of cells) between the reference cell and the cell in question along  $\vec{\mathbf{e}}_1$  and  $\vec{\mathbf{e}}_2$ , respectively.

According to Bloch's theorem, a disturbance will propagate through the structure in the form of a plane wave with a two-dimensional wave vector  $\vec{\mathbf{k}} = k_1 \vec{\mathbf{e}}_1^* + k_2 \vec{\mathbf{e}}_2^*$ , where  $\vec{\mathbf{e}}_1^*$  and  $\vec{\mathbf{e}}_2^*$  are the basis vectors of the *reciprocal* lattice, which are related to the direct lattice vectors by the identity [87]:

$$\vec{\mathbf{e}}_i \cdot \vec{\mathbf{e}}_j^* = \delta_{ij} \quad (4.19)$$

where  $\delta_{ij} = 1$  for  $i = j$ , 0 otherwise. The plane wave vector is given by:

$$\begin{aligned} W(\vec{\mathbf{R}}, t) &= W_0 e^{i\omega t} e^{i\vec{\mathbf{k}} \cdot \vec{\mathbf{R}}} \\ &= W_0 e^{i\omega t} e^{i\vec{\mathbf{k}} \cdot (\vec{\mathbf{r}} + N_1 \vec{\mathbf{e}}_1 + N_2 \vec{\mathbf{e}}_2)} \\ &= W_0 e^{i\omega t} e^{i\vec{\mathbf{k}} \cdot \vec{\mathbf{r}}} e^{N_1 \mu_1 + N_2 \mu_2} \\ &= W(\vec{\mathbf{r}}, t) e^{N_1 \mu_1 + N_2 \mu_2} \end{aligned} \quad (4.20)$$

where the propagation constants are  $\mu_1 = ik_1$  and  $\mu_2 = ik_2$ , each of which consisting of an attenuation constant and a phase constant. The Floquet boundary conditions are thus given by:

$$\begin{aligned} \mathbf{q}_3 &= \mathbf{q}_1 e^{\mu_1} = \mathbf{q}_1 e^{\alpha_1 + i\beta_1} \\ \mathbf{q}_4 &= \mathbf{q}_2 e^{\mu_1} = \mathbf{q}_2 e^{\alpha_1 + i\beta_1} \\ \mathbf{q}_7 &= \mathbf{q}_5 e^{\mu_2} = \mathbf{q}_5 e^{\alpha_2 + i\beta_2} \\ \mathbf{q}_8 &= \mathbf{q}_6 e^{\mu_2} = \mathbf{q}_6 e^{\alpha_2 + i\beta_2} \end{aligned} \quad (4.21)$$

While the unit cell had twelve nodes with a total of thirty-six degrees of freedom, equations (4.21) show that the vector of reduced degrees of freedom,  $\mathbf{q}^{\mathbf{R}}$ , will consist of

only twenty-four elements. Using the appropriate transformation matrix,  $\mathbf{T}$ , which will be a function of  $(\alpha_1, \beta_1, \alpha_2, \beta_2)$ , the reduced equations of motion for the unit cell can be cast in the form of the parametrized eigenvalue problem of equation (4.13).

By setting the attenuation constants to zero ( $\alpha_1 = \alpha_2 = 0$ ) and varying each of the phase constants  $\beta_1$  and  $\beta_2$  between 0 and  $2\pi$ , the excitation frequencies corresponding to each  $(\beta_1, \beta_2)$  pair can be computed by solving equation (4.13). Figure 4.23 shows the first twelve dispersion surfaces, demonstrating that the two-dimensional lattice does not exhibit any stop bands, *i.e.*, an incident excitation of any frequency will propagate through the structure without attenuation.

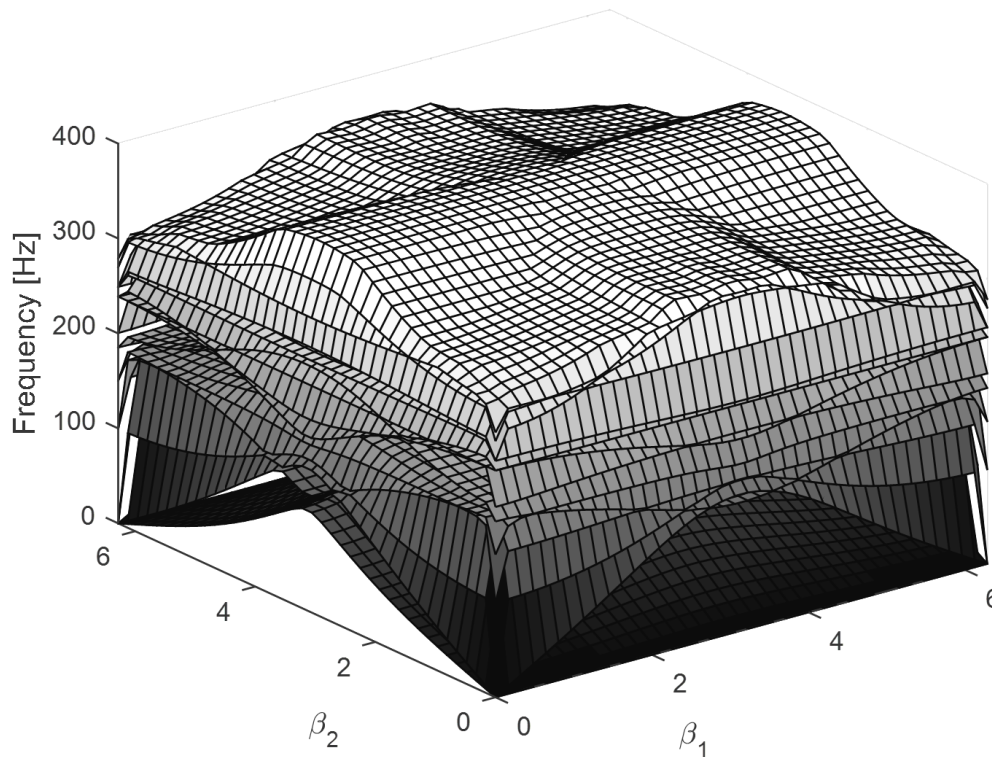


Figure 4.23 Dispersion surfaces of 2D, class-2 tensegrity array of repeating cells

## 4.9 Alternating Tensegrity Array

With the goal of combining the very high elastic modulus and bulk-to-shear ratio already observed for tensegrity arrays with the wave filtering characteristics of periodic structures, we modify the previous array design by introducing an impedance mismatch at the cell boundaries in the form of alternating material properties from one cell to the next. Specifically, for every other cell in the structure, we use bars with an elastic modulus equal to one half that in Table 3.1. When performing Bloch analysis of the new array, the repeating unit cell thus becomes the set of two individual cells with different bar modulus. Figure 4.24 shows a portion of the alternating one-dimensional array, while Figure 4.25 shows the top view of a portion of the two-dimensional one. Different bar colors signify different elastic moduli.

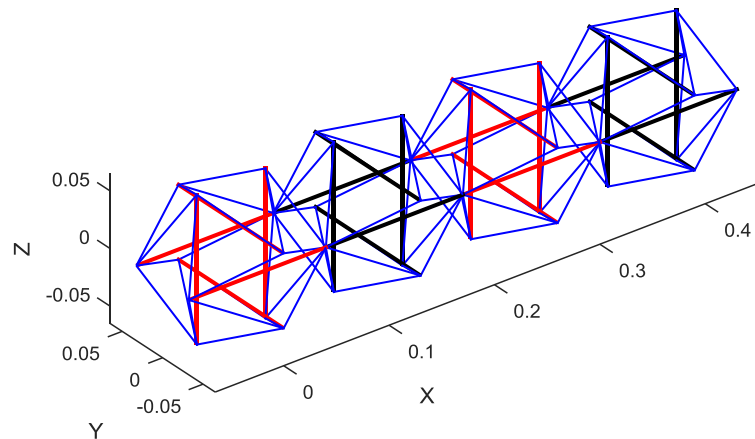


Figure 4.24 1D, class-2 tensegrity array of alternating cells



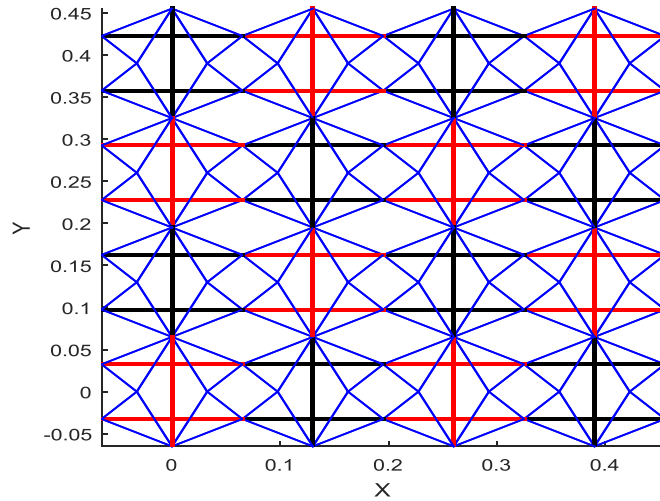


Figure 4.25 Top view of 2D, class-2 tensegrity array of alternating cells

Figure 4.26 shows the dispersion surfaces for the two-dimensional alternating array, clearly showing a wide stop band extending from 6,500 Hz to 9,500 Hz and a second one from 16,500 Hz to 19,000 Hz. The dispersion curves of the one-dimensional case (not shown) feature similar stop bands.

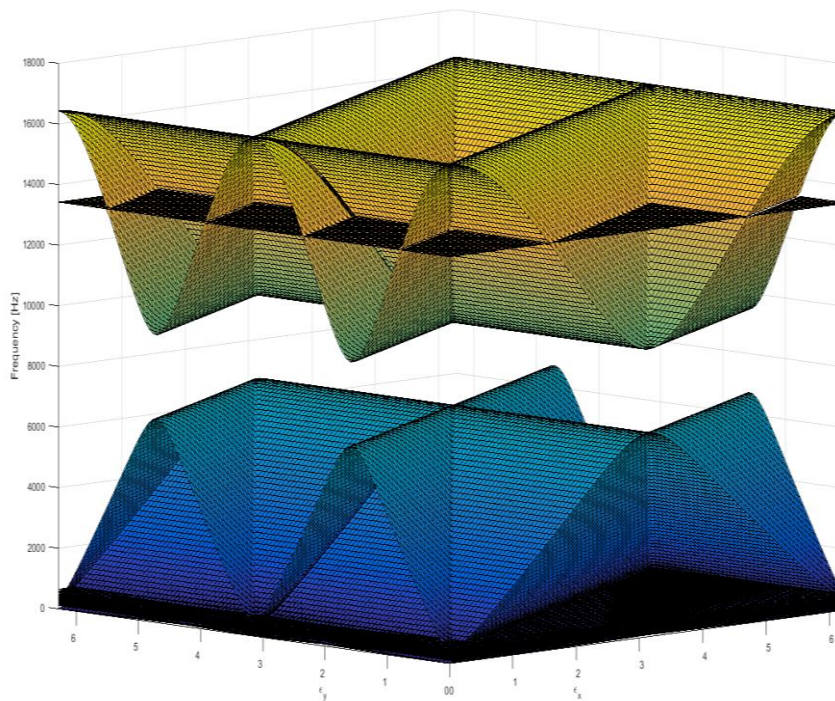


Figure 4.26 Dispersion surfaces of 2D, class-2 tensegrity array of alternating cells

#### 4.10 Summary

In this chapter, we conceived one- and two-dimensional arrays of repeating icosahedron tensegrity units, and numerically investigated their kinematic and static characteristics. The resulting structures were found to be Class-2 tensegrity structures, and had a very high bulk-to-shear ratio, again suggesting the possibility of using these structures as pentamode metamaterials. The designs were subsequently manufactured by 3D printing and the resulting structures were tested for their elastic moduli and acoustic wave propagation characteristics, which were found to be in line with the numerical simulations.

While the individual tensegrity elements (bars and strings) cannot withstand bending loads, icosahedron tensegrity cells were arranged to create a cantilever beam able to withstand bending. The bending stiffness of such beams, however, was on the lower end (on the order 100 N/m), which may not be very useful for practical applications.

We also investigated the wave propagation characteristics in the structures using Bloch's theorem and noted that the structures created using identical tensegrity units do not feature any stop bands. By introducing a periodicity in the material properties of the constitutive units, stop bands do appear. This may open the door to using periodic tensegrity lattices for vibration isolation applications.

## **Chapter 5: Alternative Design for Periodic Icosahedron Tensegrity Arrays**

### **5.1 Introduction**

The previous chapter has demonstrated that while the periodic arrays assembled from identical icosahedron tensegrity unit cells have very good static characteristics, Bloch analysis of their dynamic properties revealed that they do not exhibit any stop bands. In this chapter we explore alternative configurations of assembling the same tensegrity unit cells into periodic arrays that would achieve wave filtering characteristics.

The proposed configuration is first described, and the resulting structure is statically and kinematically analyzed to demonstrate its stability, then Bloch's theorem is applied to investigate the presence (and width and location, if applicable) of stop bands in their dispersion diagrams.

### **5.2 Description of the Unit Cell and Periodic Array**

Starting with the same icosahedron tensegrity described in Chapter 3, periodic arrays in one and two dimensions are conceived by rotating every other cell by ninety degrees about its own X, Y or Z axis, resulting in a structure with two alternating cell configurations (we will call them A and B). Under this configuration, neighboring cells will not have any vertices in common, and therefore additional members will be required to connect the units and provide stiffness to the assembly.

The simplest way to connect two adjacent cells is using four strings, *e.g.*, connecting each of the two right-most nodes of one cell to each of the two left-most nodes

of another cell. However, if neighboring cells are “touching”, *i.e.*, one cell ends exactly where the next cell begins, this leads to the four connecting strings being coplanar (forming the sides of a square). To first order approximation, this assembly will have no stiffness in the direction normal to the plane of connecting strings. Therefore, further consideration is necessary to the manner in which cells are connected to their neighbors.

We begin by introducing an offset, which may be positive or negative, between adjacent cells so that the strings can provide first order stiffness against tension along any of the three axes. Additionally, since the strings can only resist tension, then for the structure to be stable we would need to provide an additional set of strings that becomes “active” when the first set is not, and vice versa. Therefore, by setting the offset to be negative causing the cells to have a small overlap, and one set of four strings will be able resist compressive loading (tending to close the cells together), while the other set of four strings (which will be named “mast” strings) will be able to resist tensile loading (attempting to separate the cells from one another). Figure 5.1 shows only the bars and the 8 strings that connect every two neighboring cells, for an array of three tensegrity cells having a negative offset of 1 cm. In the Figure, the strings connecting nodes 3-13, 3-14, 4-13, and 4-14 can resist compressive loading on the cells (along the X axis), while the strings connecting nodes 3-21, 4-23, 10-14, and 12-13 can resist tensile loading on the cells (along the X axis).

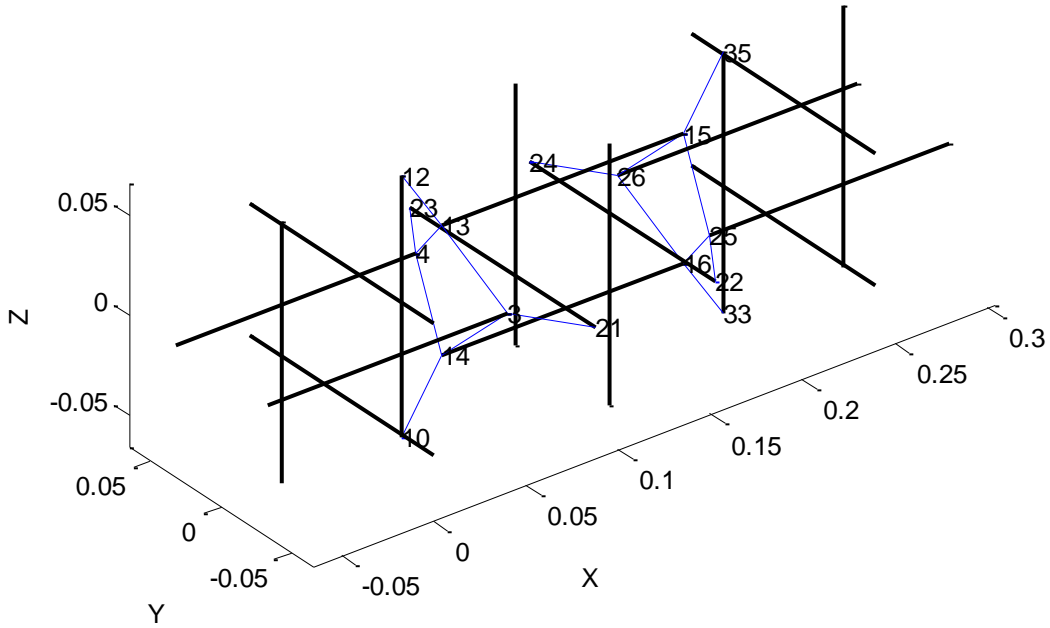


Figure 5.1 Inter-cell connectivity for 1D, class-1 tensegrity array

### 5.3 One-dimensional Array of Alternating Cells

#### 5.3.1 Geometry and Material Properties

A one-dimensional array of three tensegrity units is shown in Figure 5.1. Each cell is identical to the one described in Chapter 3. The inter-cell offset,  $\Delta e$ , is negative, leading to a small overlap between adjacent cells. The overlap must be less than  $l_b/4$  to avoid collision of the struts of neighboring cells. Adjacent cells are connected by eight massless strings: the four ‘side’ strings (*e.g.*, the strings connecting nodes 3-13, 3-14, 4-13, and 4-14) of stiffness  $K_{c1}$ , cross-section radius  $r_{c1}$ , and length  $l_{c1}$ ; and four ‘mast’ strings (*e.g.*, the strings connecting nodes 3-21, 4-23, 10-14, and 12-13) of stiffness  $K_{c2}$ , cross-section

radius  $r_{c2}$ , and length  $l_{c2}$ . The working lengths of the connecting strings will depend on the value of the offset. The parameter values for the baseline simulations are given in Table 5.1.

$l_b$	13 cm	$l_s$	$\sqrt{3/8} l_b$	$l_{c1}$	$\sqrt{\frac{l_b^2}{8} + e^2}$	$l_{c2}$	$\sqrt{\frac{l_b^2}{16} + e^2}$
$r_b$	5 mm	$r_s$	2.5 mm	$r_{c1}$	5 mm	$r_{c2}$	5 mm
$\rho_b$	500 kg/m <sup>3</sup>						
$E_b$	10 <sup>9</sup> N/m <sup>2</sup>	$K_s$	5,000 N/m	$K_{c1}$	5,000 N/m	$K_{c2}$	5,000 N/m

Table 5.1 Geometric and material properties for class-1 tensegrity array

### 5.3.2 Mechanisms and Stats of Self-stress

By computing the nullspaces of the equilibrium matrix of a one-dimensional array of  $N$  cells ( $N \geq 2$ ), it is revealed that the structure has  $n_{ss} = 2N - 2$  possible states of self-stress, of which  $N$  states correspond to each cell being loaded according to  $\mathbf{S}_1$  with the connecting strings unloaded. The array has only six mechanisms – the rigid body modes – which, once constrained, leave the structure kinematically determinate. While pre-stressing the structure according to any of the  $N$  states of self-stress will increase its stiffness, we note that the structure is always stable (with or without pre-stress). This class of kinematically determinate and statically indeterminate structures were named *redundant structures* by Murakami and Nishimura [48], and were classified as tensegrity structures by Motro (*e.g.*, [25]) and Skelton (*e.g.*, [23]). Since no two bars ever meet, and all the compression elements are loaded in compression, and the tension elements loaded in tension, we classify the structure as a Class-1 tensegrity.

### 5.3.3 Static Analysis

The elastic, shear and bulk moduli for arrays of different lengths and configurations were numerically calculated in the same way as in Chapter 4. Figures 5.2-5.5 show, respectively, the modulus of elasticity  $E_{xx}$ , the modulus of rigidity  $G_{zx}$ , the bulk modulus  $B$ , and the ratio  $B/G_{zx}$  against the level of pre-stress, for five array lengths. We first note that the elastic modulus of a 2-unit array (four cells in total) is approximately four orders of magnitude smaller than that of the single icosahedron tensegrity. This is to be expected since the overall stiffness of the array will now be determined by the stiffness of its weakest link: the connecting strings, which is much lower than that of the bars. We can also see that the pre-stress has a significant effect on the elastic modulus: increasing the pre-stress leads to a parabolic increase in the elastic modulus. Finally, increasing the number of cells leads to a decrease in the elastic modulus, which can be approximated by the expected outcome of adding springs in series.

The shear modulus, on the other hand, increases as the number of cells increases, and tends to stabilize for large numbers of cells. The pre-stress has the same effect observed in Section 4.3: initially the shear modulus increases with the pre-stress, but beyond a certain threshold, the modulus starts to decrease. The initial pre-stress corresponding to the peak shear modulus decreases as the number of units increases.

The bulk modulus decreased significantly compared to the single cell and to the one-dimensional array in Section 4.3, and in fact approximates the elastic modulus. This is due to the lower stiffness along the axis of the array relative to its transverse axes. The bulk-to-shear ratio has similarly dropped to around unity.

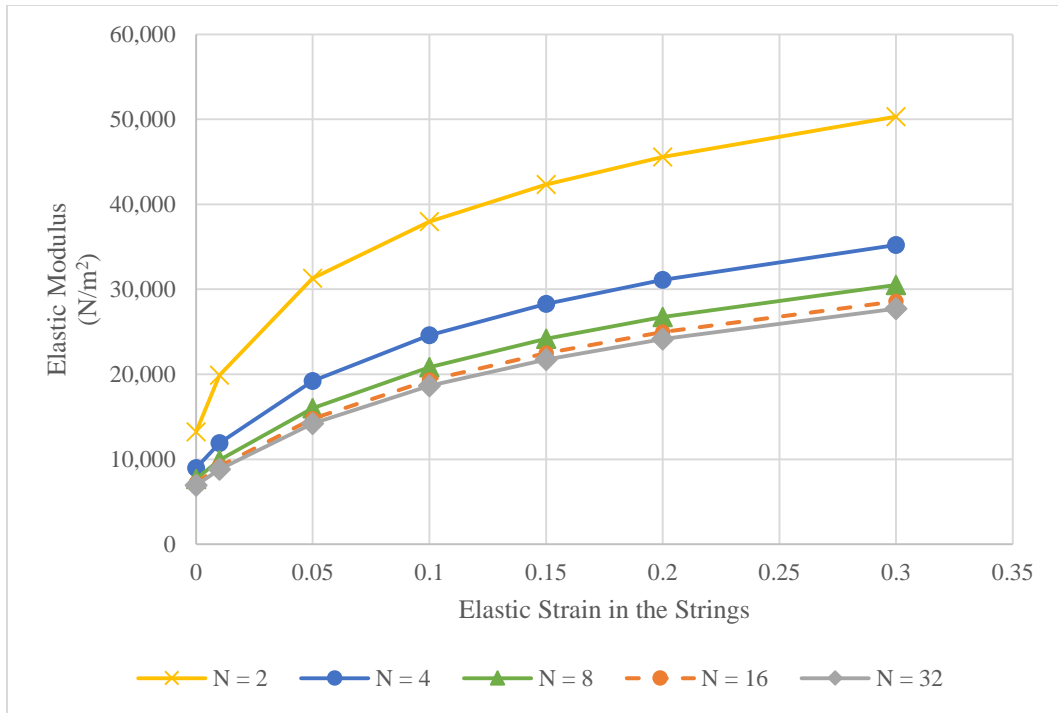


Figure 5.2 Elastic modulus of 1D, class-1 tensegrity array

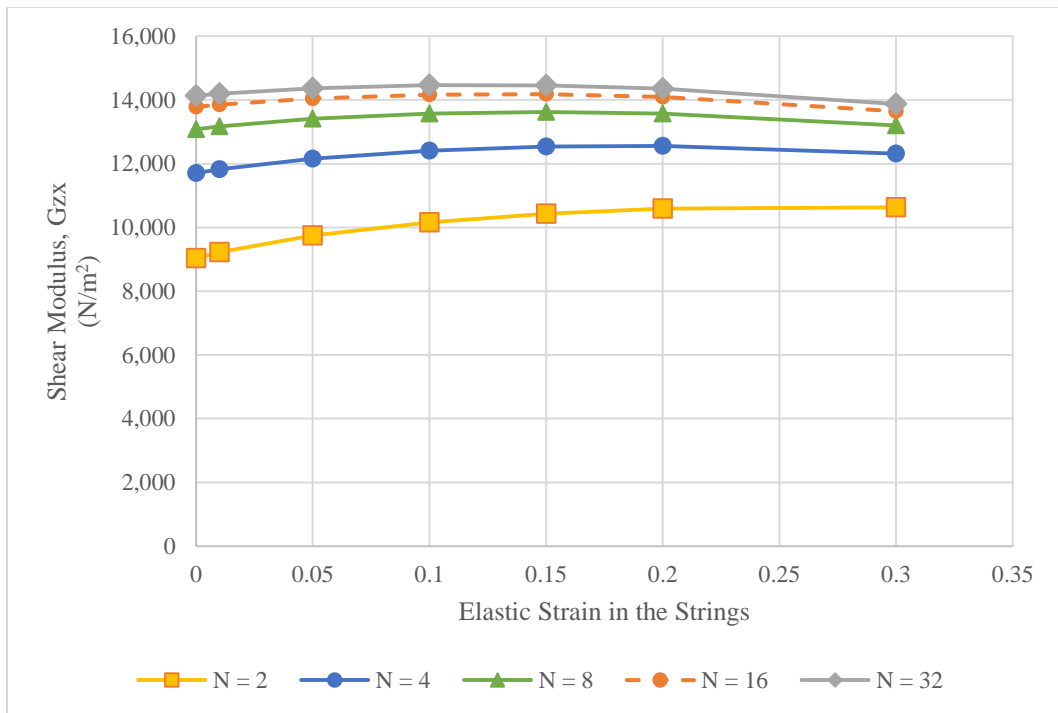


Figure 5.3 Shear modulus of 1D, class-1 tensegrity array



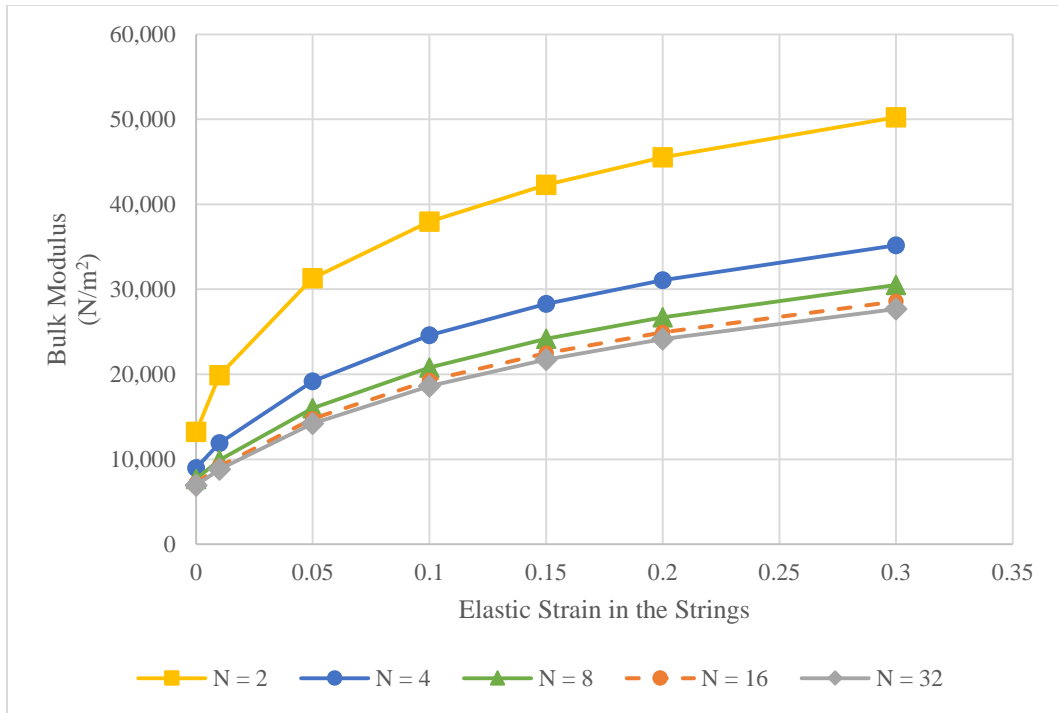


Figure 5.4 Bulk modulus of 1D, class-1 tensegrity array

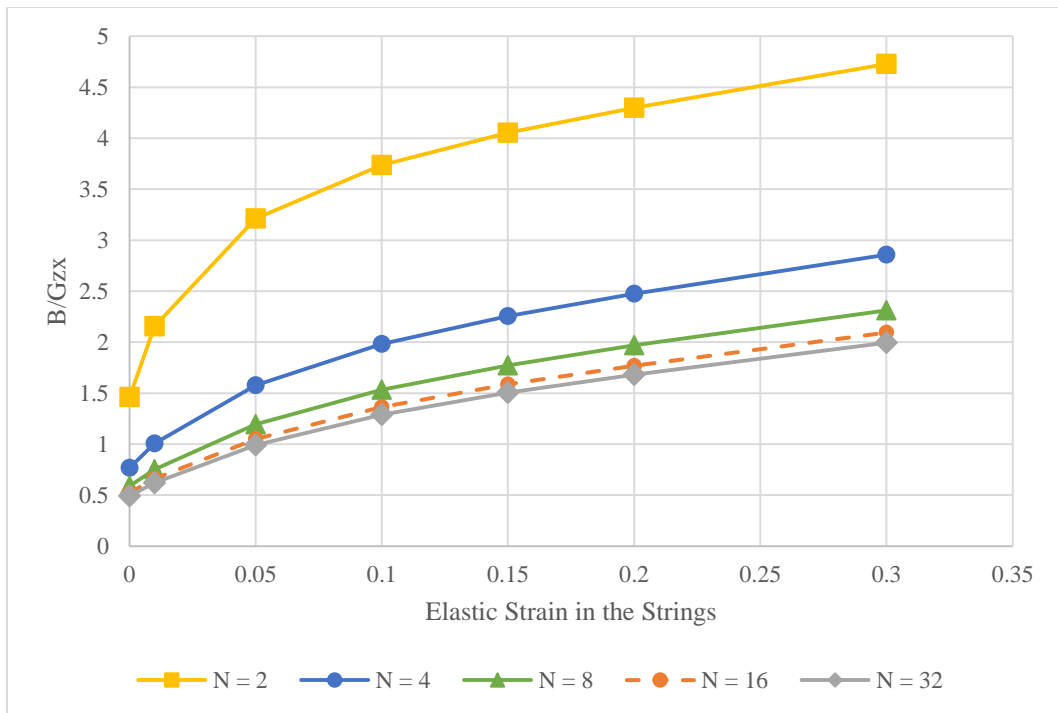


Figure 5.5 Bulk-to-shear ratio of 1D, class-1 tensegrity array

## 5.4 Dynamic Analysis

Following the procedure outlined in Chapter 4, we use Bloch's theorem to investigate the wave propagation and band structure of the infinite one-dimensional array. The unit cell chosen for the analysis is shown in Figure 5.6. It consists of two connected tensegrity cells in addition to the eight inter-cell connecting strings on the right hand side. The basis vector of the lattice is  $\vec{e} = 2(l_b - \Delta e)\hat{e}_x$  and the Floquet boundary conditions are:

$$\begin{aligned}
 \mathbf{q}_{25} &= \mathbf{q}_1 e^{\mu} = \mathbf{q}_1 e^{\alpha+i\beta} \\
 \mathbf{q}_{26} &= \mathbf{q}_2 e^{\mu} = \mathbf{q}_2 e^{\alpha+i\beta} \\
 \mathbf{q}_{27} &= \mathbf{q}_9 e^{\mu} = \mathbf{q}_9 e^{\alpha+i\beta} \\
 \mathbf{q}_{28} &= \mathbf{q}_{11} e^{\mu} = \mathbf{q}_{11} e^{\alpha+i\beta}
 \end{aligned} \tag{5.1}$$

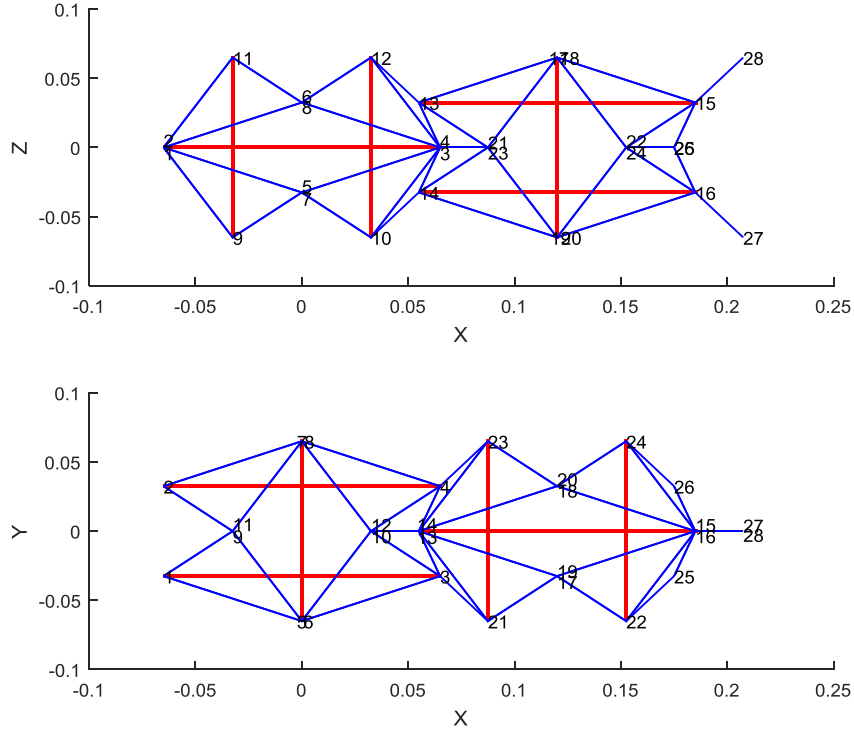


Figure 5.6 Unit cell for Bloch analysis of 1D, class-1 tensegrity array

Figure 5.7 shows the first 15 dispersion curves for the array. We can see that there are two frequency stop bands: a small one (2-Hz wide) around 101 Hz, and a larger one (11-Hz wide) around 190 Hz. Figure 5.8 shows the frequency-response plot obtained from a finite element model created in MATLAB for an array of forty cells excited harmonically from one end and the response calculated at one of the nodes on the opposite end. The simulation results are in agreement with the dispersion curves, showing very large attenuation (over 60 dB) in the frequency ranges corresponding to the stop bands.

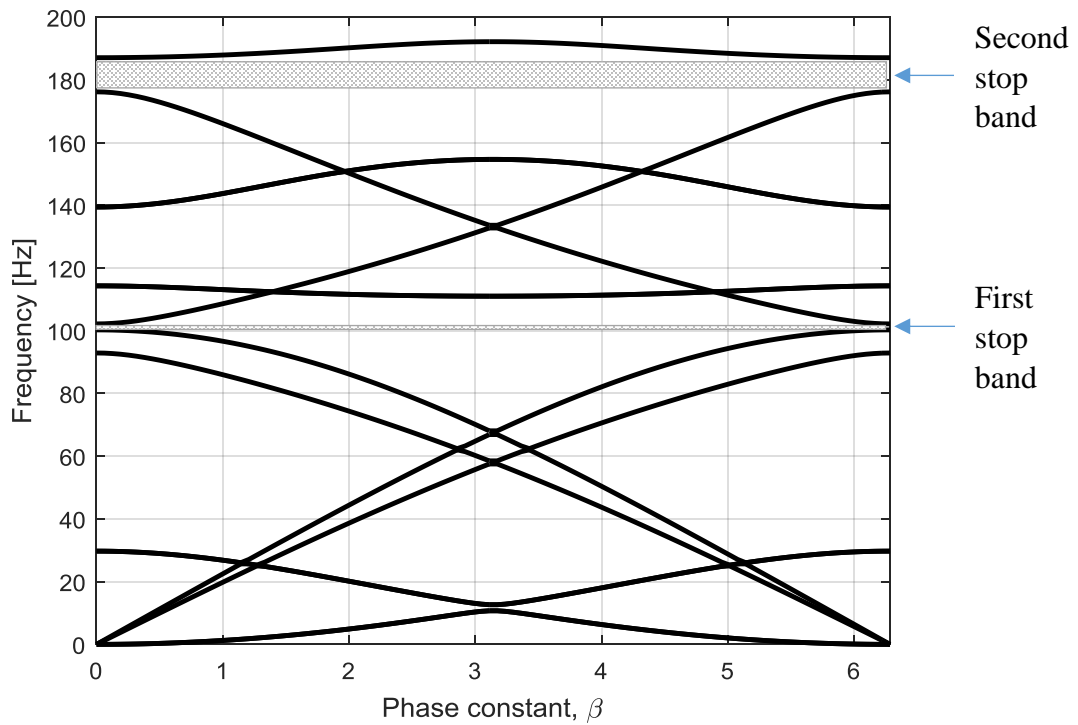


Figure 5.7 Dispersion curves for 1D, class-1 tensegrity array ( $K_c = 5000 \text{ N/m}$ )

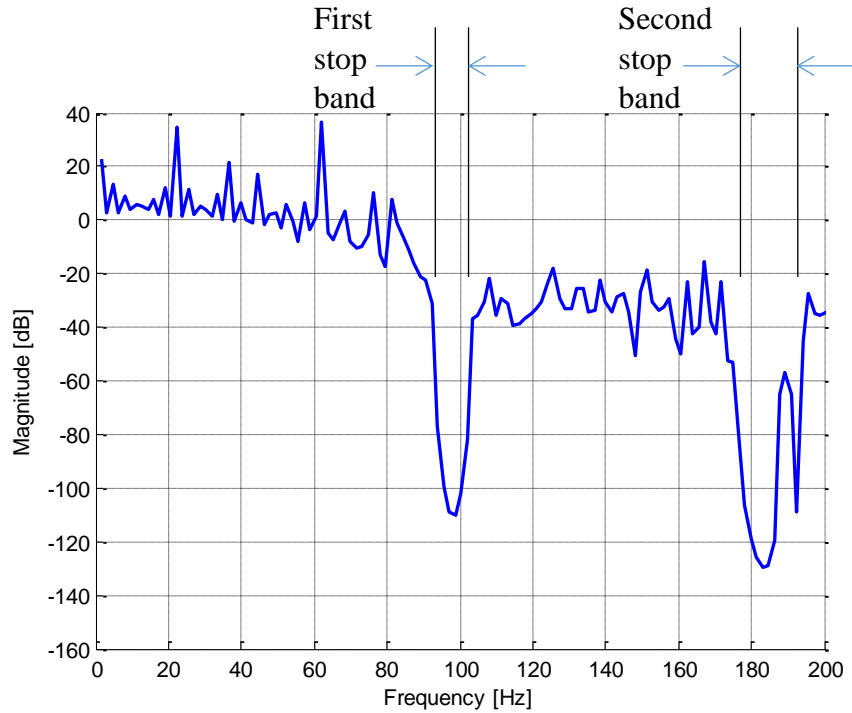


Figure 5.8 Frequency response of 1D, class-1 tensegrity array ( $K_c = 5000 \text{ N/m}$ )

#### 5.4.1 The Effect of Pre-stress

We investigate the effect of the magnitude of pre-stress, represented by the initial strain in the strings, on the presence and width of stop bands. Figure 5.9 shows the pass and stop bands corresponding to different levels of pre-stress. In the figure, the empty frequency intervals are complete stop bands, *i.e.*, no wave, regardless of its wave number, can propagate in these intervals. We conclude that changing the pre-stress can be used as a tool to tune the location and width of the stop bands to serve a given application.

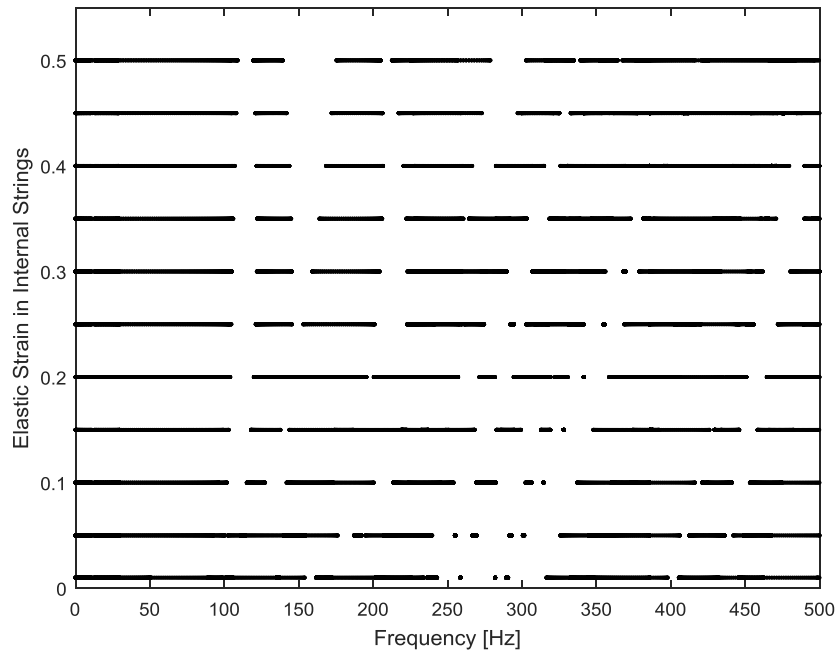


Figure 5.9 Effect of pre-stress on stop bands ( $K_c = 5000 \text{ N/m}$ )

#### 5.4.2 The Effect of Connecting Strings' Stiffness

We reduce the stiffness of the eight connecting strings to  $1000 \text{ N/m}$  while keeping everything else constant. We observe that the stop bands, shown in Figure 5.10, have widened significantly. Figure 5.11 shows the frequency-response plot obtained from numerical simulation of a one-dimensional array of forty tensegrity units subject to harmonic excitation. The attenuation zones are in agreement with the stop bands visible in Figure 5.10.

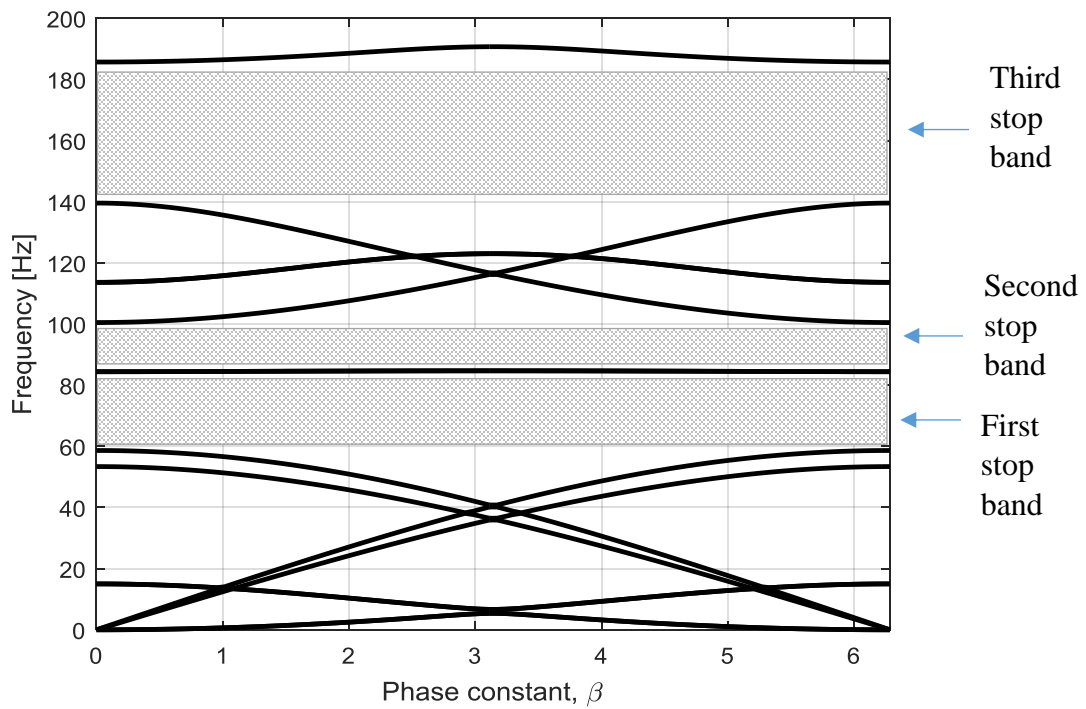


Figure 5.10 Dispersion curves for 1D, class-1 tensegrity array ( $K_c = 1000 \text{ N/m}$ )

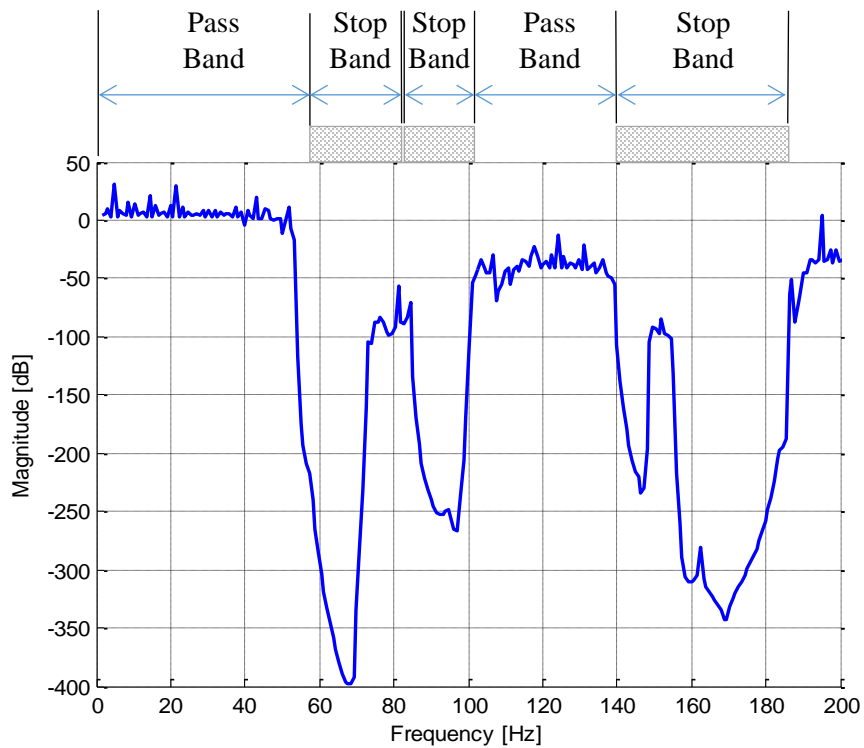


Figure 5.11 Frequency response for 1D, class-1 tensegrity array ( $K_c = 1000 \text{ N/m}$ )

## 5.5 Two-Dimensional Arrays

### 5.5.1 Description

We assume a two-dimensional array of tensegrity cells aligned with the global X and Y axes. The array consists of  $N_X$  ‘columns’ along the X axis and  $N_Y$  ‘rows’ along the Y axis. The center of the first cell lies at the origin of the coordinate system and has its local axes aligned with the global axes, satisfying cell configuration A. Each subsequent cell that has a neighbor with this configuration will assume configuration B, and vice versa.

Figure 5.12 shows the top view of a portion of such an array.

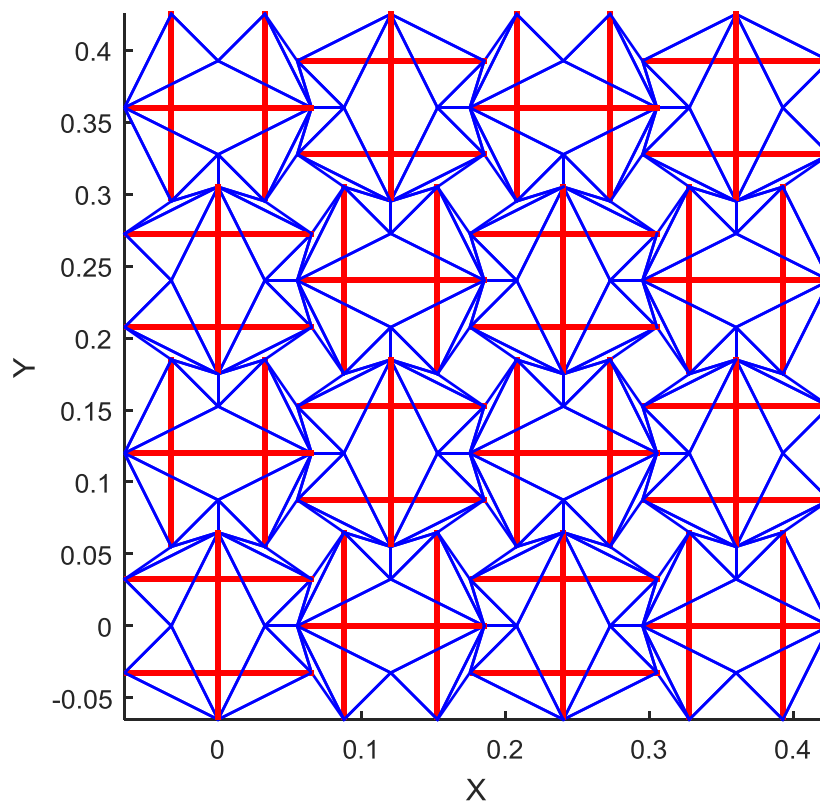


Figure 5.12 Top view of 2D, class-1 tensegrity array

### 5.5.2 Mechanisms and States of Self-stress

Investigation of the equilibrium matrix of two-dimensional arrays reveals that the number of states of self-stress (the nullity of the matrix) satisfies the empirical relationship

$$n_{SS} = 10 N_X N_Y - 8N_X - 8N_Y + 6 \quad (5.2)$$

where  $N_X, N_Y \geq 1$ . The basis for this null space includes  $N_X N_Y$  vectors, each corresponding to an individual cell of the array being stressed in accordance with  $\mathbf{S}_1$ , while all other cells and connecting strings unstressed.

The number of mechanisms (the nullity of the kinematic matrix) is always six for an unconstrained array, corresponding to the rigid body modes which are then eliminated with appropriate boundary conditions.

Similar to the one-dimensional case, investigation of the stiffness matrix shows that the constrained, unstressed structure is stable (all the eigenvalues are positive), and that introducing a pre-stress in each cell equal to a positive multiple of  $\mathbf{S}_1$  increases the overall stiffness of the array and ensures that all members are properly loaded. Therefore, we conclude that such pre-stressed structures are Class-1 tensegrity structures.

### 5.5.3 Static Analysis

We perform the numerical simulations to determine the array's elastic moduli, for different array sizes and magnitudes of pre-stress. All other properties are as given in Table 5.1 Geometric and material properties for class-1 tensegrity arrayTable 5.1, and the overlap between adjacent cells is  $10 \text{ mm}$  ( $\Delta e = -10\text{mm}$ ).



### 5.5.3.1 The Modulus of Elasticity

- Boundary Conditions

To calculate  $E_{xx}$ , the two leftmost nodes of every cell of the leftmost column of cells are constrained from moving along the X-axis. Additionally, all the top and bottom nodes of the same set of cells are completely constrained, simulating the effect of the grip of a universal testing machine clamping down on that first column of cells. A prescribed displacement along the positive X-direction is applied to the rightmost nodes of the rightmost column. All the other degrees of freedom are unconstrained.

To calculate  $E_{yy}$ , all the front nodes (smallest Y coordinate) of the first row of cells are constrained from moving along the Y-axis, and all the top and bottom nodes of the same row of cells are completely constrained. A prescribed displacement along the positive Y-direction is applied on the back nodes (largest Y coordinate) of the last row of cells.

- The Moduli

Figure 5.13 and Figure 5.14 show  $E_{xx}$  and  $E_{yy}$ , respectively. They indicate that the modulus of elasticity increases with the initial strain and decreases when the number of cells along the direction of the force increases. Both moduli are on the order of  $10^4 \text{ N/m}^2$ .

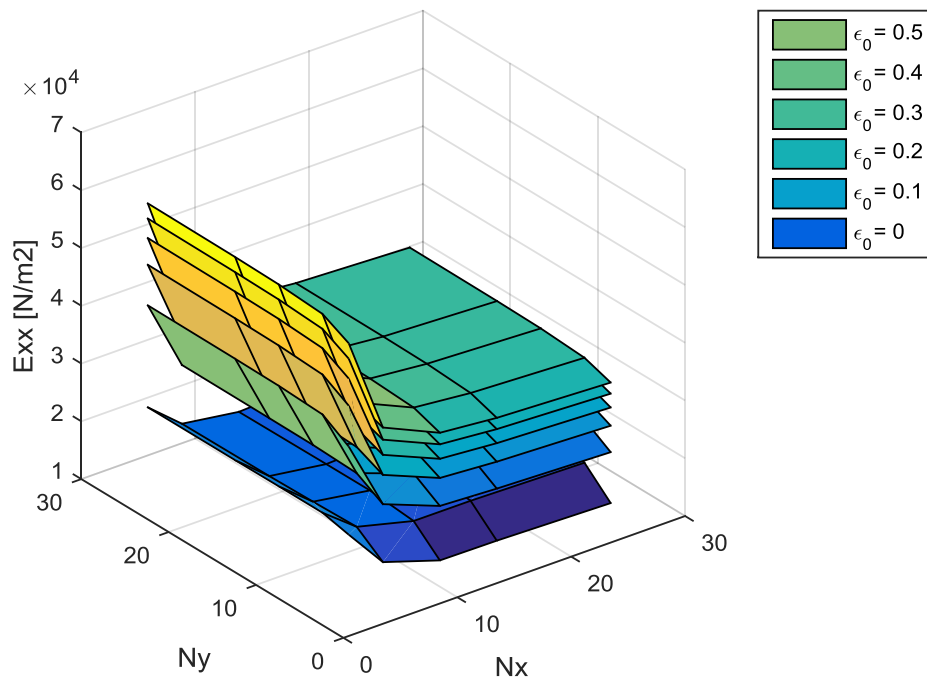


Figure 5.13 Elastic modulus  $E_{xx}$  of 2D, class-1 tensegrity array

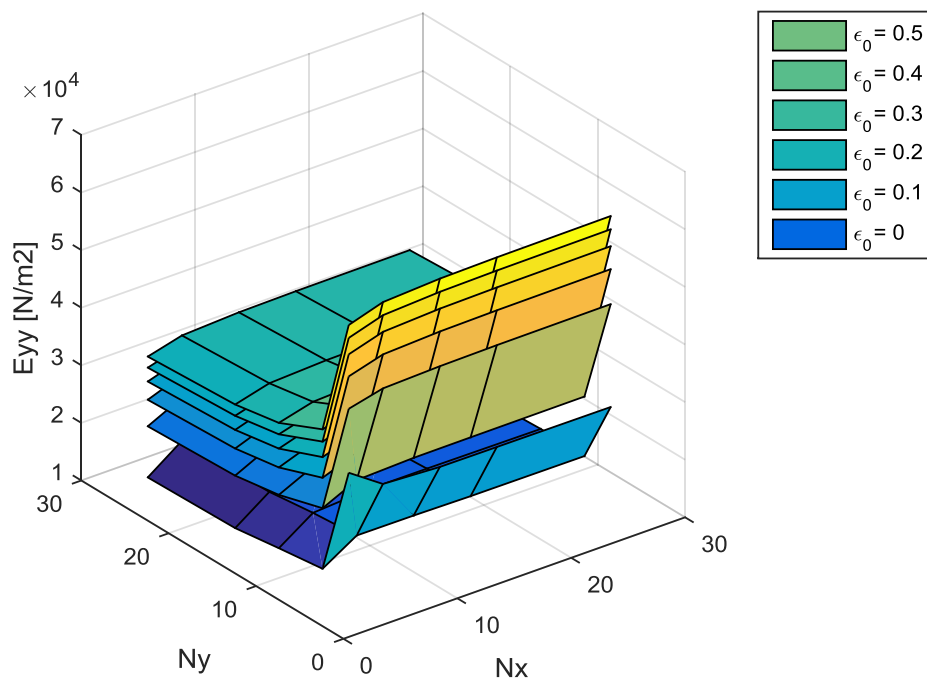


Figure 5.14 Elastic modulus  $E_{yy}$  of 2D, class-1 tensegrity array

### 5.5.3.2 The Shear Moduli

We investigate the shear moduli  $G_{zx}$  and  $G_{zy}$  by imposing a known displacement on the top nodes of the array, along the X and Y axes, respectively, and compute the resulting nodal forces and the moduli. Figure 5.15 and Figure 5.16 show  $G_{zx}$  and  $G_{zy}$ , respectively. They indicate that both shear moduli are on the order of  $10^4 N/m^2$  and increase as the number of cells increase. The effect of varying the pre-stress is consistent with previously-observed behavior: the shear modulus increases as the initial strain increases from 0 to 0.2 then decreases as the initial strain is increased further.

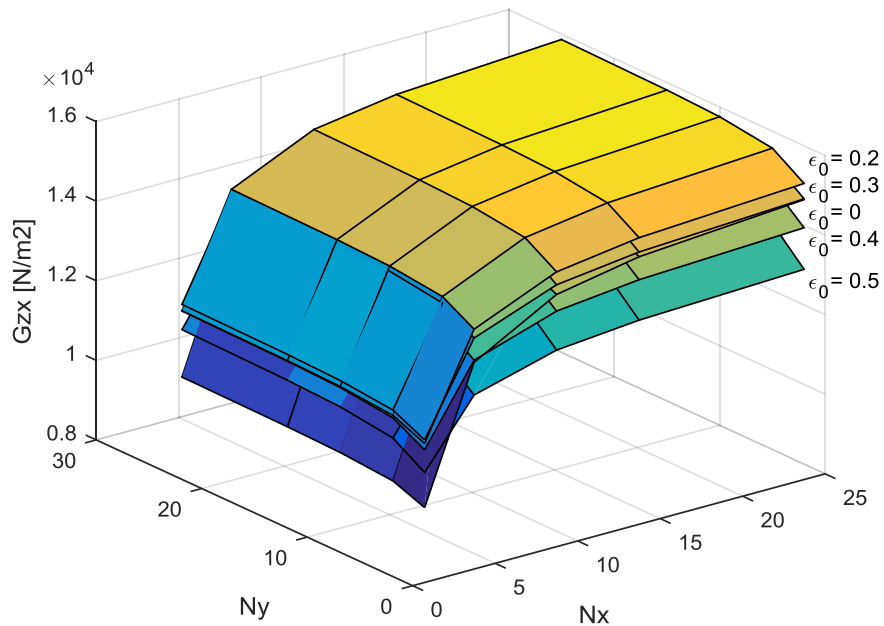


Figure 5.15 Shear modulus  $G_{zx}$  of 2D, class-1 tensegrity array

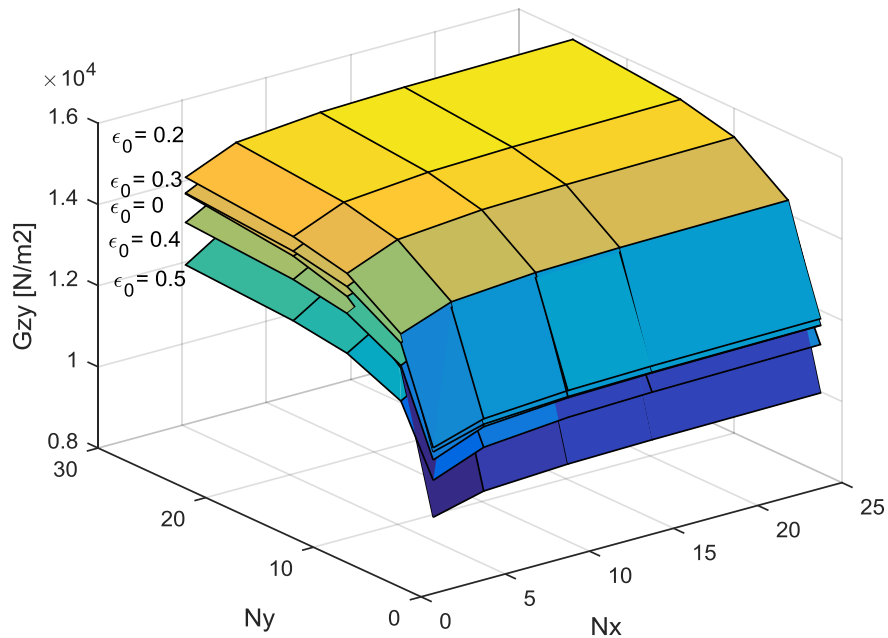


Figure 5.16 Shear modulus  $G_{zy}$  of 2D, class-1 tensegrity array

### 5.5.3.3 The Bulk Modulus

Figure 5.17 shows the bulk modulus for different array sizes and initial strain magnitudes. The bulk modulus is on the order of  $10^4 \text{N/m}^2$ , and decreases slightly as the array size increases but tends to stabilize for large arrays. The effect of the initial strain is evident: higher initial strain (hence, pre-stress) results in a higher bulk modulus.

The bulk-to-shear ratio is on the order of unity, similar to that of existing naturally-occurring materials, and suggesting that this configuration may not be suitable for the synthesis of pentamode metamaterials.

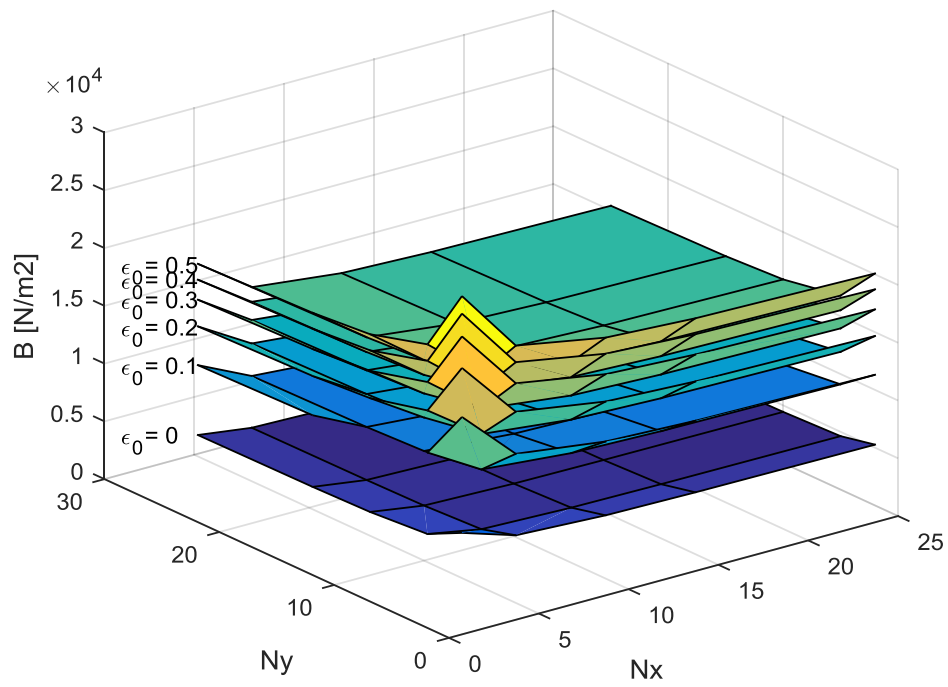


Figure 5.17 Bulk modulus of 2D, class-1 tensegrity array

### 5.5.4 Dynamic Analysis of 2D Array

We analyze the wave propagation characteristics of an infinite two-dimensional array using Bloch's theorem to identify the frequency band structure of the arrays.

The unit cell is shown in Figure 5.18. It consists of two individual cells, one of Type A and the other of Type B, along with their eight inter-cell connecting strings, the eight strings connecting them to their neighbor in the positive X direction, and the sixteen strings connecting each of the two cells to their respective neighbors in the positive Y direction. The unit cell therefore includes thirty-six nodes, each admitting three degrees of freedom. Figure 5.19 shows a schematic top view of the array, as obtained by tessellating the unit cell with its two constitutive cells: A (shown in gray) and B (shown in white) along the axes  $X_1$  and  $X_2$ . The basis vectors of the direct lattice are

$$\begin{aligned}\vec{e}_1 &= 2(l_b - \Delta e)\hat{e}_x \\ \vec{e}_2 &= (l_b - \Delta e)\hat{e}_x + (l_b - \Delta e)\hat{e}_y\end{aligned}\tag{5.3}$$

Each cell is associated with two integer indices  $(n_1, n_2)$  representing the number of translations along  $\vec{e}_1$  and  $\vec{e}_2$ , respectively, necessary to reach the cell from the reference cell at the origin. According to Bloch's theorem, a planar wave propagating through the structure will be associated with two independent propagation constants,  $\mu_1$  and  $\mu_2$ , such that:

$$W(\vec{\mathbf{R}}, t) = W(\vec{\mathbf{r}}, t) e^{N_1\mu_1 + N_2\mu_2}\tag{5.4}$$

where  $\mu_1 = \alpha_1 + i\beta_1$  and  $\mu_2 = \alpha_2 + i\beta_2$ .

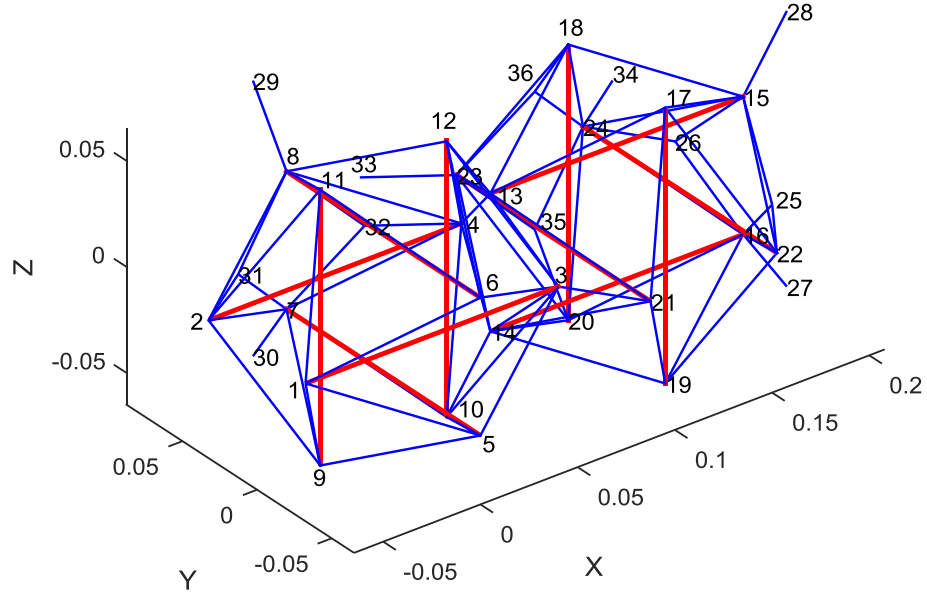


Figure 5.18 Unit cell for Bloch analysis of 2D class-1 tensegrity array

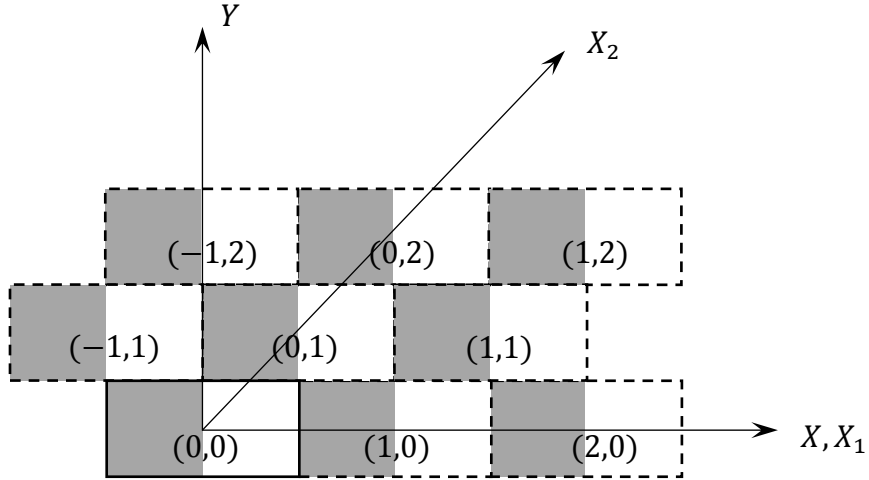


Figure 5.19 Layout of the 2D array

From the periodicity of the array, the Floquet boundary conditions are:

$$\begin{array}{lll}
 \mathbf{q}_{25} = \mathbf{q}_1 e^{\mu_1} & \mathbf{q}_{33} = \mathbf{q}_1 e^{\mu_2} & \mathbf{q}_{29} = \mathbf{q}_{17} e^{(\mu_2 - \mu_1)} \\
 \mathbf{q}_{26} = \mathbf{q}_2 e^{\mu_1} & \mathbf{q}_{34} = \mathbf{q}_3 e^{\mu_2} & \mathbf{q}_{30} = \mathbf{q}_{19} e^{(\mu_2 - \mu_1)} \\
 \mathbf{q}_{27} = \mathbf{q}_9 e^{\mu_1} & \mathbf{q}_{35} = \mathbf{q}_5 e^{\mu_2} & \mathbf{q}_{31} = \mathbf{q}_{21} e^{(\mu_2 - \mu_1)} \\
 \mathbf{q}_{28} = \mathbf{q}_{11} e^{\mu_1} & \mathbf{q}_{36} = \mathbf{q}_6 e^{\mu_2} & \mathbf{q}_{32} = \mathbf{q}_{22} e^{(\mu_2 - \mu_1)}
 \end{array}$$

Once the equations of motion have been cast in the form of eq. (4.13), we set the attenuation constants to zero ( $\alpha_1 = \alpha_2 = 0$ ), and allow the phase constants  $\beta_1$  and  $\beta_2$  to scan the range  $[0, 2\pi]$ . Solving the reduced equations of motion thus yields the frequencies of oscillation that can propagate unimpeded for each pair of phase constants, and the dispersion surfaces of the system can be plotted. Figure 5.20 shows the dispersion surfaces (up to 500 Hz) of an array with the properties shown in Table 5.1 and an initial strain of 0.05 in the internal strings. Three complete stop bands can be seen (between 300 and 362 Hz) where no oscillations can propagate. Several partial bandgaps (limited to specific directions of propagation) may exist at other frequencies. Figure 5.21 shows the effect of the initial strain on the location and width of the stop bands (shown for  $Kc = 2000$  N/m and  $e = -10$  mm), suggesting that adjusting the pre-stress may be used as a tuning parameter to adjust the location or width of the stop bands, e.g., to encompass a specific excitation frequency.

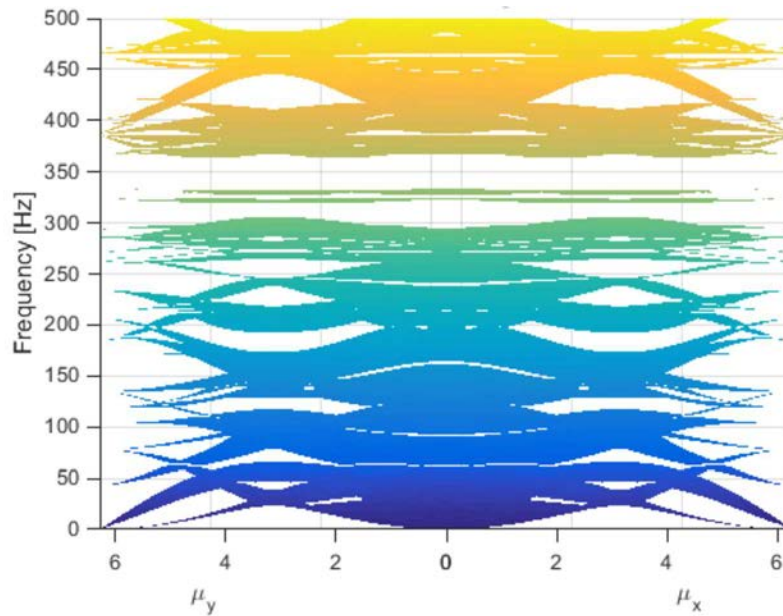


Figure 5.20 Dispersion surfaces of 2D, class-1 tensegrity array



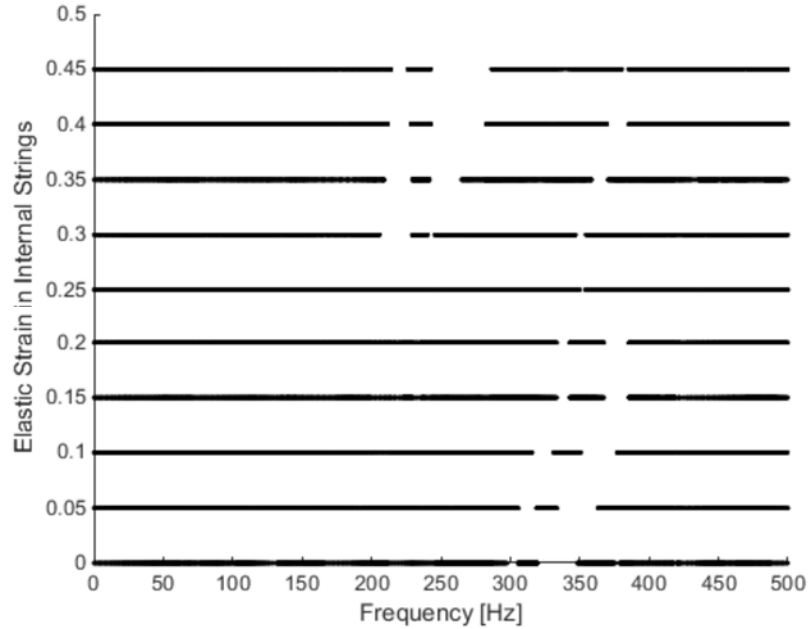


Figure 5.21 Effect of pre-stress on pass and stop bands

The pass and stop bands obtained from the Bloch analysis were verified numerically using MATLAB by simulating a  $30 \times 30$  rectangular tensegrity lattice with the same characteristics listed above, subjecting it to a uni-axial sinusoidal excitation from one side, and calculating the resulting displacement on the opposite side. Figure 5.22 shows the frequency-response plots for two cases: initial strain values of 0.1 and 0.3, for excitation along the X-axis. The plots show very high attenuation in the frequency ranges corresponding to the stop bands predicted by Bloch's theorem. We note that, in the case of  $\epsilon_0 = 0.3$ , the response features two additional attenuation bands (in the 380-480 Hz range) which may be due to partial stop bands. The results for excitation along the Y-axis (not shown) are very similar.

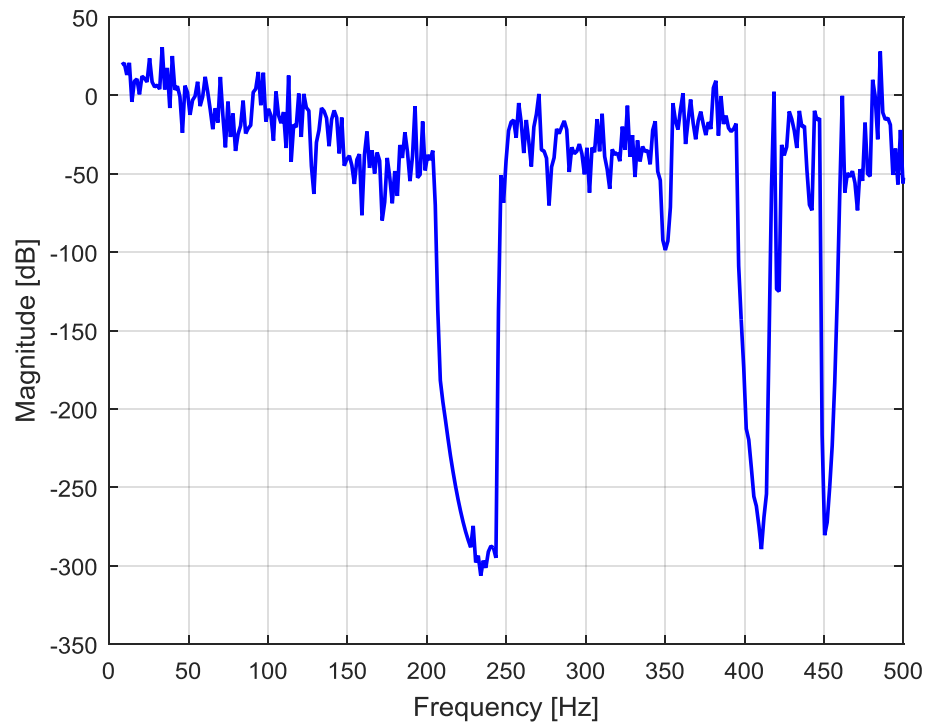
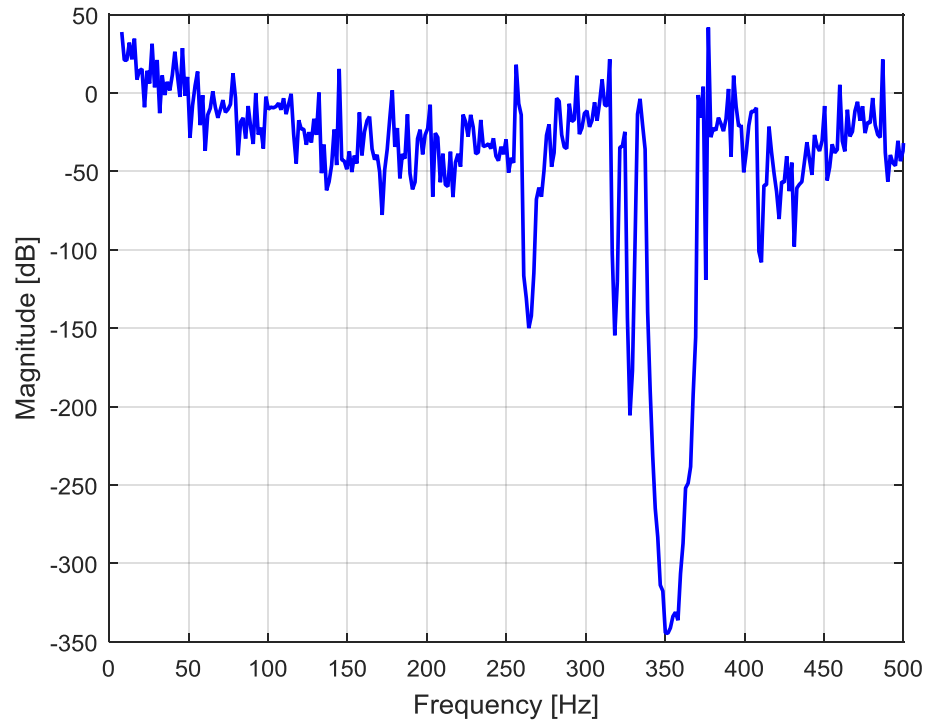


Figure 5.22 Frequency response of 2D, class-1 tensegrity array  
for initial strain 0.1 (top) and 0.3 (bottom)

## 5.6 Summary

In this chapter we conceived an alternative configuration for one- and two-dimensional periodic arrays of icosahedron tensegrity units. The array is found to be a Class-1 tensegrity structure. Bloch analysis of wave propagation characteristics of the structure showed the presence of frequency pass and stop bands, where the location and width of the bands depended on the parameters of the cell (*e.g.*, pre-stress and material properties), which could then be used to tune the bands.

Investigation of the elastic coefficients and the bulk-to-shear ratio of the structures revealed that they dropped drastically compared to the structures of the previous chapter, possibly undermining their use as structural elements or pentamode metamaterials.

## Chapter 6: Design and Testing of Tensegrity Damper

### 6.1 Introduction

In this chapter we propose, build, and test a tensegrity-based damper, able to attenuate vibration amplitudes – within certain frequency bands – by virtue of its periodicity. We first present the concept and develop the mathematical model of its constitutive unit cell, which is then generalized to the periodic array using Floquet-Bloch analysis to identify the frequency pass and stop bands. We build a prototype using 3D printing, perform material characterization on it and carry out testing and experimental validation of the static and dynamic predictions.

### 6.2 Description

The damper is shown schematically in Figure 6.1. It consists of repeating tensegrity cells where each cell consists of four flexible links forming the sides of a rhombus and one rigid link constituting one of the diagonals. Another rigid link, orthogonal to the first, connects each two consecutive cells.

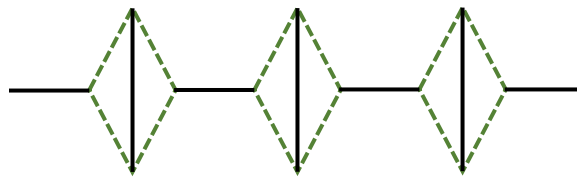


Figure 6.1 Schematic of periodic tensegrity damper  
(solid black lines are rigid links, dashed green lines are flexible links)

### 6.3 Derivation of Equations of Motion

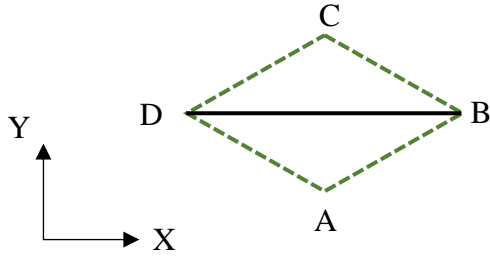


Figure 6.2 Tensegrity damper unit cell

We begin by deriving the equations of motion of one tensegrity unit cell, shown in Figure 6.2, under the following assumptions:

- All degrees of freedom in the horizontal (X-) direction are constrained
- The effect of gravity is ignored – the structure lies in a plane parallel to the ground
- Rigid elements are perfectly rigid while flexible elements could be elastic or viscoelastic

We note that by assuming a perfectly rigid link  $BD$  constrained to move only in the vertical (Y-) direction, then the following must be true:

$$y_B = y_D \quad (6.1)$$

We can therefore derive the equations of motion of the unit cell using Lagrangian mechanics, using the three generalized coordinates  $(y_A, y_B, y_C)$  which represent the positions of nodes  $(A, B, C)$ , respectively, along the Y-axis with respect to the inertial frame of reference. Each coordinate consists of an equilibrium position term  $(y_{A0}, y_{B0}, y_{C0})$  and a displacement term  $(w_A, w_B, w_C)$ .

$$\begin{aligned}
 y_A &= y_{A0} + w_A \\
 y_B &= y_{B0} + w_B \\
 y_C &= y_{C0} + w_C
 \end{aligned}
 \tag{6.2}$$

In order to derive the kinetic and potential energies of the flexible elements, we consider a general constrained one in Figure 6.3.  $w_M$  and  $w_N$  are the end-nodes' vertical displacements from their equilibrium positions, respectively. The undeformed and deformed element lengths are  $l_0$  and  $l$ , respectively, and the element has mass  $m_i$ , moment of inertia  $I$ , and stiffness  $K_i$ .

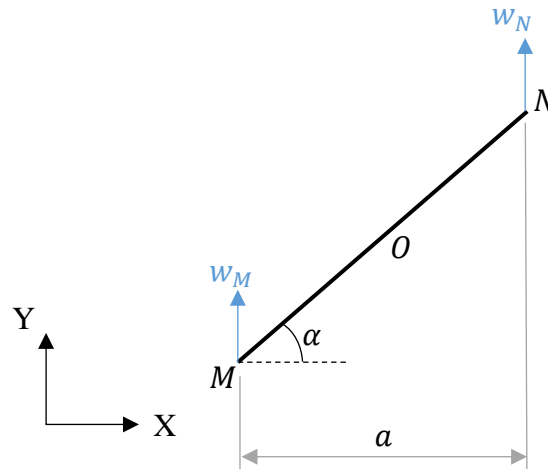


Figure 6.3 Representative flexible element

The acute angle,  $\alpha$ , that the element makes with the horizontal can be defined using:

$$\tan \alpha = \frac{y_N - y_M}{a}
 \tag{6.3}$$

the derivative of which with respect to time is:

$$\frac{1}{(\cos \alpha)^2} \dot{\alpha} = \frac{\dot{y}_N - \dot{y}_M}{a} \quad (6.4)$$

From the geometry, we can substitute:  $\cos \alpha = \frac{a}{l}$ , which results in:

$$\dot{\alpha} = \frac{\dot{y}_N - \dot{y}_M}{a} \left(\frac{a}{l}\right)^2 \quad (6.5)$$

Finally, we note that the length of the element is:

$$l = \sqrt{(y_N - y_M)^2 + a^2} \quad (6.6)$$

Therefore, the kinetic and potential energies of the constrained flexible element  $i$  can be given by equations (6.7) and (6.8), respectively:

$$\begin{aligned} T_i &= \frac{1}{2} m_i v_M^2 + \frac{1}{2} \omega \cdot I \cdot \omega + m_i v_M \cdot \dot{\rho}_{OM} \\ &= \frac{1}{2} m_i \dot{y}_M^2 + \frac{1}{2} \left(\frac{1}{3} m_i l^2\right) \dot{\alpha}^2 + m_i \dot{y}_M \left(\frac{\dot{y}_N - \dot{y}_M}{2}\right) \\ &= \frac{1}{2} m_i \dot{y}_M \dot{y}_N + \frac{1}{6} m_i \left(\frac{a}{l}\right)^2 (\dot{y}_N - \dot{y}_M)^2 \end{aligned} \quad (6.7)$$

$$V_i = \frac{1}{2} K_i (l - l_0)^2 = \frac{1}{2} \frac{E A_i}{l_0} (l - l_0)^2 \quad (6.8)$$

where  $A_i$  is the cross-section area of the element and  $E$  is the elastic modulus in the case of an elastic material or the complex modulus in the case of a viscoelastic material.

For a rigid, constrained element  $j$  of mass  $m_j$ , every point on the element will move with the same vertical velocity  $\dot{y}_j$ , yielding the kinetic and potential energies:

$$T_j = \frac{1}{2} m_j (\dot{y}_j)^2 \quad (6.9)$$

$$V_j = 0 \quad (6.10)$$

The kinetic and potential energies of each of the unit cell's members are therefore given by:

$$\begin{aligned}
T_{AB} &= \frac{1}{2}m_1\dot{y}_A\dot{y}_B + \frac{1}{6}m_1\left(\frac{a}{l_1}\right)^2(\dot{y}_B - \dot{y}_A)^2 & V_{AB} &= \frac{1}{2}K_1(l_1 - l_0)^2 \\
T_{AD} &= \frac{1}{2}m_2\dot{y}_A\dot{y}_B + \frac{1}{6}m_2\left(\frac{a}{l_2}\right)^2(\dot{y}_B - \dot{y}_A)^2 & V_{AD} &= \frac{1}{2}K_2(l_2 - l_0)^2 \\
T_{BC} &= \frac{1}{2}m_3\dot{y}_B\dot{y}_C + \frac{1}{6}m_3\left(\frac{a}{l_3}\right)^2(\dot{y}_C - \dot{y}_B)^2 & V_{BC} &= \frac{1}{2}K_3(l_3 - l_0)^2 \\
T_{CD} &= \frac{1}{2}m_4\dot{y}_B\dot{y}_C + \frac{1}{6}m_4\left(\frac{a}{l_4}\right)^2(\dot{y}_C - \dot{y}_B)^2 & V_{CD} &= \frac{1}{2}K_4(l_4 - l_0)^2 \\
T_{BD} &= \frac{1}{2}m_5\dot{y}_B^2 & V_{BD} &= 0 \\
T_{CE} &= \frac{1}{2}m_6\dot{y}_C^2 & V_{CE} &= 0
\end{aligned} \tag{6.11}$$

We also note that, due to the constraints,  $l_1 = l_2$  and  $l_3 = l_4$ . The Lagrangian of the unit cell is given by

$$\mathcal{L} = \Sigma T - \Sigma V \tag{6.12}$$

which is then substituted into Lagrange's equation

$$\frac{d}{dt}\left(\frac{\partial \mathcal{L}}{\partial \dot{q}}\right) - \frac{\partial \mathcal{L}}{\partial q} = F \tag{6.13}$$

and derivations are carried out for each of the three generalized coordinates  $(y_A, y_B, y_C)$ .

The detailed derivations and substitutions can be found in Appendix C and result in the three nonlinear equations of motion:



$$\begin{aligned}
& \frac{1}{3}(m_1 + m_2) \frac{a^2}{l_1^2} \ddot{y}_A + (m_1 + m_2) \left( \frac{1}{2} - \frac{1}{3} \frac{a^2}{l_1^2} \right) \ddot{y}_B \\
& \quad + \frac{1}{3} (m_1 + m_2) \frac{a^2}{l_1^4} (y_B - y_A) (\dot{y}_B - \dot{y}_A)^2 \\
& \quad - (K_1 + K_2) \frac{l_1 - l_0}{l_1} (y_B - y_A) = F_A \\
(m_1 + m_2) & \left( \frac{1}{2} - \frac{1}{3} \frac{a^2}{l_1^2} \right) \ddot{y}_A \\
& \quad + \left[ \frac{1}{3} (m_1 + m_2) \frac{a^2}{l_1^2} + \frac{1}{3} (m_3 + m_4) \frac{a^2}{l_3^2} + m_5 \right] \ddot{y}_B \\
& \quad + (m_3 + m_4) \left( \frac{1}{2} - \frac{1}{3} \frac{a^2}{l_3^2} \right) \ddot{y}_C \\
& \quad - \frac{1}{3} (m_1 + m_2) \frac{a^2}{l_1^4} (y_B - y_A) (\dot{y}_B - \dot{y}_A)^2 \\
& \quad + \frac{1}{3} (m_3 + m_4) \frac{a^2}{l_3^4} (y_C - y_B) (\dot{y}_C - \dot{y}_B)^2 \\
& \quad + (K_1 + K_2) \frac{l_1 - l_0}{l_1} (y_B - y_A) \\
& \quad - (K_3 + K_4) \frac{l_3 - l_0}{l_3} (y_C - y_B) = F_B + F_D \\
(m_3 + m_4) & \left( \frac{1}{2} - \frac{1}{3} \frac{a^2}{l_3^2} \right) \ddot{y}_B + \frac{1}{3} (m_3 + m_4) \frac{a^2}{l_3^2} \ddot{y}_C \\
& \quad - \frac{1}{3} (m_3 + m_4) \frac{a^2}{l_3^4} (y_C - y_B) (\dot{y}_C - \dot{y}_B)^2 \\
& \quad + (K_3 + K_4) \frac{l_3 - l_0}{l_3} (y_C - y_B) = F_C
\end{aligned} \tag{6.14}$$

The nonlinear equations of motion above are then linearized for small deviations  $(w_A, w_B, w_C)$  from the equilibrium position  $(y_{A0}, y_{B0}, y_{C0})$  using Taylor series expansion of the nonlinear terms followed by truncation of second and higher order terms. The detailed work can also be found in Appendix C, with the resulting linearized equations of motion expressed in the following matrix form:

$$\mathbf{M}\ddot{\mathbf{W}} + \mathbf{K}\mathbf{W} = \mathbf{F} \quad (6.15)$$

where  $\mathbf{W} = [w_A \ w_B \ w_C]^T$ ,  $\mathbf{F} = [F_A \ F_B + F_D \ F_C]^T$ ,

**M**

$$= \begin{bmatrix} \frac{1}{3}(m_1 + m_2)\frac{a^2}{l_0^2} & (m_1 + m_2)\left(\frac{1}{2} - \frac{1}{3}\frac{a^2}{l_0^2}\right) & 0 \\ (m_1 + m_2)\left(\frac{1}{2} - \frac{1}{3}\frac{a^2}{l_0^2}\right) & \frac{1}{3}(m_1 + m_2 + m_3 + m_4)\frac{a^2}{l_0^2} + m_5 & (m_3 + m_4)\left(\frac{1}{2} - \frac{1}{3}\frac{a^2}{l_0^2}\right) \\ 0 & (m_3 + m_4)\left(\frac{1}{2} - \frac{1}{3}\frac{a^2}{l_0^2}\right) & \frac{1}{3}(m_3 + m_4)\frac{a^2}{l_0^2} + m_6 \end{bmatrix}$$

$$\equiv \begin{bmatrix} M_{AA} & M_{AB} & 0 \\ M_{BA} & M_{BB} & M_{BC} \\ 0 & M_{CB} & M_{CC} \end{bmatrix}, \text{ and}$$

$$\mathbf{K} = (\sin \alpha_0)^2 \begin{bmatrix} K_1 + K_2 & -(K_1 + K_2) & 0 \\ -(K_1 + K_2) & K_1 + K_2 + K_3 + K_4 & -(K_3 + K_4) \\ 0 & -(K_3 + K_4) & K_3 + K_4 \end{bmatrix}$$

$$\equiv E \begin{bmatrix} \gamma & -\gamma & 0 \\ -\gamma & \gamma + \delta & -\delta \\ 0 & -\delta & \delta \end{bmatrix}$$

where  $\gamma = \frac{A_1 + A_2}{l_0} (\sin \alpha_0)^2$  and  $\delta = \frac{A_3 + A_4}{l_0} (\sin \alpha_0)^2$ .

We note that both the stiffness and mass matrices are symmetric and positive semi-definite, and that by constraining any of the degrees of freedom to eliminate the rigid body mode, the stiffness matrix becomes positive definite signifying that the structure is stable.

#### 6.4 Comparison of Linear and Nonlinear Equations of Motion

In order to validate our linearization and identify the limitations of the linear model, Figure 6.4 compares the responses obtained using the nonlinear and linear models, respectively, for a representative unit cell constrained at its top node (C) and subjected to

a vertical sinusoidal force at its bottom node (A). Assuming all flexible links have the same dimensions and material properties, we investigate the vertical deviation of node A from equilibrium ( $w_A$ ), which is obtained in the nonlinear case by numerical integration of the equations of motion (6.14) using MATLAB, while in the linear case it is obtained by assuming a harmonic response with a constant amplitude for (6.15), thus resulting in the following algebraic matrix equation (6.16), which can then be solved.

$$\mathbf{W} = (\mathbf{K} - \omega^2 \mathbf{M})^{-1} \mathbf{F} \quad (6.16)$$

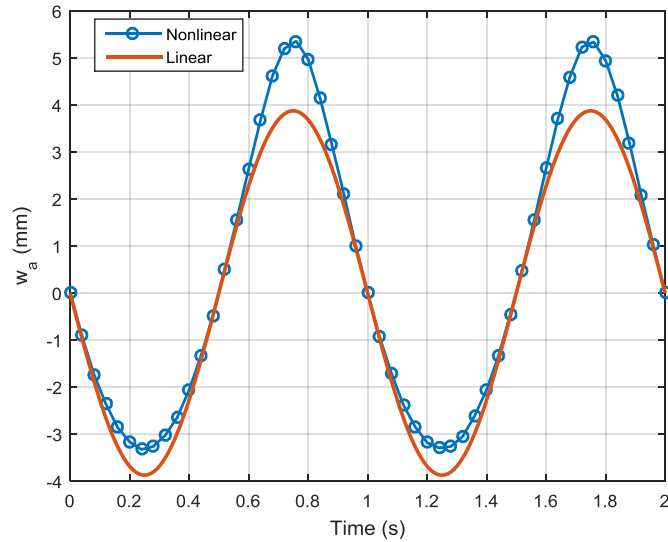


Figure 6.4 Linear vs nonlinear forced response of tensegrity damper unit cell

As would be expected, the linearized model's response is also sinusoidal and follows the input, while the nonlinear response diverges in the vicinity of the extrema. Noting that a negative value for  $w_A$  corresponds to the cell being extended, this deviation can be explained by the geometry effect: while the stiffness matrix of the linear system is evaluated once at the static equilibrium position (where  $\alpha = \alpha_0$ ), the flexible element's stiffness in the nonlinear model is in fact changing as the cell deforms. As the cell elongates,  $\alpha$  increases and so does the stiffness, thereby limiting the extension; and as the

cell is compressed,  $\alpha$  decreases and so does the stiffness leading to a larger deformation than predicted with the linear model.

From this observation, we can identify the limit value for the external compressive force that the cell can withstand, beyond which the combined stiffnesses of the flexible elements will not be able to balance the external force, leading to the collapse of the cell. For the given configuration, and assuming the same material properties for all flexible elements, the restoring force in the springs is given by

$$K \frac{l_1 - l_0}{l_1} y_A = F \quad (6.17)$$

The maximum value of which is found by finding its derivative with respect to  $y_A$ , setting it equal to zero, and finding the corresponding  $y_A$  as a function of the cell parameters:

$$y_{ACR} = 2 \left( \sqrt[3]{a^4 l_0^2} - a^2 \right)^{1/2} \quad (6.18)$$

which results in the following critical load:

$$F_{CR} = K \frac{\sqrt[3]{a^2 l_0} - l_0}{\sqrt[3]{a^2 l_0}} y_{ACR} \quad (6.19)$$

Therefore, for stable operation of the tensegrity cell in the assumed configuration, one must ensure that the applied compressive force will not exceed the critical load calculated above. As long as this condition is satisfied, the linearized model may be considered a reasonable approximation for the physical system.

## 6.5 Modeling Viscoelastic Flexible Elements

Viscoelastic materials are characterized by complex material moduli, *e.g.*, for the elastic modulus:

$$E = E' + i E'' = E'(1 + i\eta)$$

where the real part,  $E'$ , is the storage modulus and represents the elastic energy stored upon deformation, while the imaginary part,  $E''$ , is the loss modulus and represents the energy dissipated as heat.  $\eta$  is the loss factor, equal to the ratio of the loss modulus to the storage modulus, which provides a measure of the damping in the material. It is often expressed as the tangent of the phase angle,  $\delta$ , between the loss and storage moduli:

$$\eta = \tan \delta = \frac{E''}{E'}$$

The GHM model of viscoelasticity, introduced by Golla and Hughes [179] and McTavish and Hughes [180], describes the complex modulus of a viscoelastic material with a second order differential equation, expressed in the Laplace domain as

$$E = E_0 \left[ 1 + \sum_{i=1}^N \alpha_i \frac{s^2 + 2\zeta_i \omega_i s}{s^2 + 2\zeta_i \omega_i s + \omega_i^2} \right] \quad (6.20)$$

where  $s$  is the Laplace variable ( $s = i\omega$ ),  $E_0$  is the modulus at zero frequency, and  $\alpha_i$ ,  $\zeta_i$  and  $\omega_i$  are parameters obtained from curve fitting the experimental data obtained for a given viscoelastic material at a given temperature.

This formulation has been found to yield a dynamic mathematical model of the viscoelastic material analogous to that of a spring mounted in parallel with  $N$  *mini-oscillators*, each of which consisting of a mass, a spring and a damper mounted in series.

The number of mini-oscillators,  $N$ , determines the quality of the curve-fitting, with two mini-oscillators often providing a good approximation of the experimental data. Assuming that the chosen flexible material can indeed be modeled with two mini-oscillators, the modulus (6.20) will become:

$$E = E_0 \left[ 1 + \alpha_1 \frac{s^2 + 2\zeta_1 \omega_1 s}{s^2 + 2\zeta_1 \omega_1 s + \omega_1^2} + \alpha_2 \frac{s^2 + 2\zeta_2 \omega_2 s}{s^2 + 2\zeta_2 \omega_2 s + \omega_2^2} \right] \quad (6.21)$$

For each physical degree of freedom associated with a viscoelastic element we define a number of internal, or *dissipation*, degrees of freedom equal to the number of mini-oscillators in the model. In this case all three degrees of freedom are tethered to viscoelastic elements, resulting in a total of six internal degrees of freedom, defined as follows:

$$\mathbf{z}_I = \begin{bmatrix} z_1 \\ z_2 \\ z_3 \end{bmatrix} = \frac{\omega_1^2}{s^2 + 2\zeta_1 \omega_1 s + \omega_1^2} \begin{bmatrix} w_A \\ w_B \\ w_C \end{bmatrix} \quad (6.22)$$

$$\mathbf{z}_{II} = \begin{bmatrix} z_4 \\ z_5 \\ z_6 \end{bmatrix} = \frac{\omega_2^2}{s^2 + 2\zeta_2 \omega_2 s + \omega_2^2} \begin{bmatrix} w_A \\ w_B \\ w_C \end{bmatrix}$$

We note that we can rewrite the first of these definitions as

$$\frac{s^2 + 2\zeta_1 \omega_1 s}{s^2 + 2\zeta_1 \omega_1 s + \omega_1^2} w_A = w_A - z_1 \quad (6.23)$$

with similar expressions for the remaining internal degrees of freedom. Therefore, we can use the GHM model (6.21) to substitute for  $E$  in the set of linearized equations of motion (6.19), and subsequently use (6.23) and similar expressions to substitute for the appropriate terms, ultimately resulting in the following three equations:

$$\begin{aligned}
M_{AA}\ddot{w}_A + M_{AB}\ddot{w}_B + E_0\gamma[(1 + \alpha_1 + \alpha_2)w_A - \alpha_1z_1 - \alpha_2z_4] \\
- E_0\gamma[(1 + \alpha_1 + \alpha_2)w_B - \alpha_1z_2 - \alpha_2z_5] &= F_A \\
M_{BA}\ddot{w}_A + M_{BB}\ddot{w}_B + M_{BC}\ddot{w}_C - E_0\gamma[(1 + \alpha_1 + \alpha_2)w_A - \alpha_1z_1 - \alpha_2z_4] \\
+ E_0(\gamma + \delta)[(1 + \alpha_1 + \alpha_2)w_B - \alpha_1z_2 - \alpha_2z_5] \\
- E_0\delta[(1 + \alpha_1 + \alpha_2)w_C - \alpha_1z_3 - \alpha_2z_6] &= F_B + F_D \\
M_{CB}\ddot{w}_B + M_{CC}\ddot{w}_C - E_0\delta[(1 + \alpha_1 + \alpha_2)w_B - \alpha_1z_2 - \alpha_2z_5] \\
+ E_0\delta[(1 + \alpha_1 + \alpha_2)w_C - \alpha_1z_3 - \alpha_2z_6] &= F_C
\end{aligned} \tag{6.24}$$

This set of equations is complemented by the six equations that define the internal degrees of freedom (6.22), expressed in the time domain in matrix form as follows:

$$\begin{aligned}
\begin{bmatrix} \ddot{\mathbf{z}}_I \\ \ddot{\mathbf{z}}_{II} \end{bmatrix} + \begin{bmatrix} 2\zeta_1\omega_1\mathbf{I} & \mathbf{0} \\ \mathbf{0} & 2\zeta_2\omega_2\mathbf{I} \end{bmatrix} \begin{bmatrix} \dot{\mathbf{z}}_I \\ \dot{\mathbf{z}}_{II} \end{bmatrix} + \begin{bmatrix} \omega_1^2\mathbf{I} & \mathbf{0} \\ \mathbf{0} & \omega_2^2\mathbf{I} \end{bmatrix} \begin{bmatrix} \mathbf{z}_I \\ \mathbf{z}_{II} \end{bmatrix} \\
- \begin{bmatrix} \omega_1^2\mathbf{I} & \mathbf{0} \\ \mathbf{0} & \omega_2^2\mathbf{I} \end{bmatrix} \begin{bmatrix} \mathbf{W} \\ \mathbf{W} \end{bmatrix} = \mathbf{0}
\end{aligned} \tag{6.25}$$

The combined set of 9 differential equations in 9 unknowns represents the augmented system of equations of motion, which can be cast in the following block matrix form:

$$\begin{aligned}
\begin{bmatrix} \mathbf{M} & \mathbf{0} & \mathbf{0} \\ \mathbf{0} & \mathbf{I} & \mathbf{0} \\ \mathbf{0} & \mathbf{0} & \mathbf{I} \end{bmatrix} \begin{bmatrix} \ddot{\mathbf{W}} \\ \ddot{\mathbf{z}}_I \\ \ddot{\mathbf{z}}_{II} \end{bmatrix} + \begin{bmatrix} \mathbf{0} & \mathbf{0} & \mathbf{0} \\ \mathbf{0} & 2\zeta_1\omega_1\mathbf{I} & \mathbf{0} \\ \mathbf{0} & \mathbf{0} & 2\zeta_2\omega_2\mathbf{I} \end{bmatrix} \begin{bmatrix} \dot{\mathbf{W}} \\ \dot{\mathbf{z}}_I \\ \dot{\mathbf{z}}_{II} \end{bmatrix} \\
+ \begin{bmatrix} \mathbf{K}(1 + \alpha_1 + \alpha_2) & -\alpha_1\mathbf{K} & -\alpha_2\mathbf{K} \\ -\omega_1^2\mathbf{I} & \omega_1^2\mathbf{I} & \mathbf{0} \\ -\omega_2^2\mathbf{I} & \mathbf{0} & \omega_2^2\mathbf{I} \end{bmatrix} \begin{bmatrix} \mathbf{W} \\ \mathbf{z}_I \\ \mathbf{z}_{II} \end{bmatrix} = \begin{bmatrix} \mathbf{F} \\ \mathbf{0} \\ \mathbf{0} \end{bmatrix}
\end{aligned} \tag{6.26}$$

The procedure, outlined in [180], then calls for the decomposition of the physical system's stiffness matrix,  $\mathbf{K}$ , according to:

$$\mathbf{K} = \bar{\mathbf{R}}\bar{\boldsymbol{\Lambda}}\bar{\mathbf{R}}^T \tag{6.27}$$

where  $\mathbf{\Lambda}$  is the diagonal matrix of non-zero eigenvalues of the stiffness matrix, and  $\bar{\mathbf{R}}$  is the matrix whose columns are the corresponding eigenvectors, normalized such that:

$$\bar{\mathbf{R}}^T \bar{\mathbf{R}} = \mathbf{I} \quad (6.28)$$

An intermediate set of internal coordinates is also defined:

$$\begin{aligned} \mathbf{z}_A &= \bar{\mathbf{R}}^T \mathbf{z}_I \\ \mathbf{z}_B &= \bar{\mathbf{R}}^T \mathbf{z}_{II} \end{aligned} \quad (6.29)$$

Therefore, multiplying the second and third rows in equation (6.26) by  $\mathbf{K} \frac{\alpha_1}{\omega_1^2}$  and  $\mathbf{K} \frac{\alpha_2}{\omega_2^2}$ ,

respectively, and substituting for  $\mathbf{K}$  according to (6.27), we get:

$$\begin{aligned} & \begin{bmatrix} \mathbf{M} & \mathbf{0} & \mathbf{0} \\ \mathbf{0} & \frac{\alpha_1}{\omega_1^2} \bar{\mathbf{R}} \mathbf{\Lambda} & \mathbf{0} \\ \mathbf{0} & \mathbf{0} & \frac{\alpha_2}{\omega_2^2} \bar{\mathbf{R}} \mathbf{\Lambda} \end{bmatrix} \begin{bmatrix} \ddot{\mathbf{W}} \\ \ddot{\mathbf{z}}_A \\ \ddot{\mathbf{z}}_B \end{bmatrix} + \begin{bmatrix} \mathbf{0} & \mathbf{0} & \mathbf{0} \\ \mathbf{0} & 2\zeta_1 \frac{\alpha_1}{\omega_1} \bar{\mathbf{R}} \mathbf{\Lambda} & \mathbf{0} \\ \mathbf{0} & \mathbf{0} & 2\zeta_2 \frac{\alpha_2}{\omega_2} \bar{\mathbf{R}} \mathbf{\Lambda} \end{bmatrix} \begin{bmatrix} \dot{\mathbf{W}} \\ \dot{\mathbf{z}}_A \\ \dot{\mathbf{z}}_B \end{bmatrix} \\ & + \begin{bmatrix} \mathbf{K}(1 + \alpha_1 + \alpha_2) & -\alpha_1 \bar{\mathbf{R}} \mathbf{\Lambda} & -\alpha_2 \bar{\mathbf{R}} \mathbf{\Lambda} \\ -\alpha_1 \bar{\mathbf{R}} \mathbf{\Lambda} \bar{\mathbf{R}}^T & \alpha_1 \bar{\mathbf{R}} \mathbf{\Lambda} & \mathbf{0} \\ -\alpha_2 \bar{\mathbf{R}} \mathbf{\Lambda} \bar{\mathbf{R}}^T & \mathbf{0} & \alpha_2 \bar{\mathbf{R}} \mathbf{\Lambda} \end{bmatrix} \begin{bmatrix} \mathbf{W} \\ \mathbf{z}_A \\ \mathbf{z}_B \end{bmatrix} = \begin{bmatrix} \mathbf{F} \\ \mathbf{0} \\ \mathbf{0} \end{bmatrix} \end{aligned} \quad (6.30)$$

Pre-multiplying the second and third rows by  $\bar{\mathbf{R}}^T$ , and defining

$$\mathbf{R} = \bar{\mathbf{R}} \mathbf{\Lambda} \quad (6.31)$$

We can write:

$$\begin{aligned} & \begin{bmatrix} \mathbf{M} & \mathbf{0} & \mathbf{0} \\ \mathbf{0} & \frac{\alpha_1}{\omega_1^2} \mathbf{\Lambda} & \mathbf{0} \\ \mathbf{0} & \mathbf{0} & \frac{\alpha_2}{\omega_2^2} \mathbf{\Lambda} \end{bmatrix} \begin{bmatrix} \ddot{\mathbf{W}} \\ \ddot{\mathbf{z}}_A \\ \ddot{\mathbf{z}}_B \end{bmatrix} + \begin{bmatrix} \mathbf{0} & \mathbf{0} & \mathbf{0} \\ \mathbf{0} & 2\zeta_1 \frac{\alpha_1}{\omega_1} \mathbf{\Lambda} & \mathbf{0} \\ \mathbf{0} & \mathbf{0} & 2\zeta_2 \frac{\alpha_2}{\omega_2} \mathbf{\Lambda} \end{bmatrix} \begin{bmatrix} \dot{\mathbf{W}} \\ \dot{\mathbf{z}}_A \\ \dot{\mathbf{z}}_B \end{bmatrix} \\ & + \begin{bmatrix} \mathbf{K}(1 + \alpha_1 + \alpha_2) & -\alpha_1 \mathbf{R} & -\alpha_2 \mathbf{R} \\ -\alpha_1 \mathbf{R}^T & \alpha_1 \mathbf{\Lambda} & \mathbf{0} \\ -\alpha_2 \mathbf{R}^T & \mathbf{0} & \alpha_2 \mathbf{\Lambda} \end{bmatrix} \begin{bmatrix} \mathbf{W} \\ \mathbf{z}_A \\ \mathbf{z}_B \end{bmatrix} = \begin{bmatrix} \mathbf{F} \\ \mathbf{0} \\ \mathbf{0} \end{bmatrix} \end{aligned} \quad (6.32)$$



Or, in a more compact notation:

$$\mathbf{M}_{\text{aug}} \begin{bmatrix} \ddot{\mathbf{W}} \\ \ddot{\mathbf{z}}_{\mathbf{A}} \\ \ddot{\mathbf{z}}_{\mathbf{B}} \end{bmatrix} + \mathbf{C}_{\text{aug}} \begin{bmatrix} \dot{\mathbf{W}} \\ \dot{\mathbf{z}}_{\mathbf{A}} \\ \dot{\mathbf{z}}_{\mathbf{B}} \end{bmatrix} + \mathbf{K}_{\text{aug}} \begin{bmatrix} \mathbf{W} \\ \mathbf{z}_{\mathbf{A}} \\ \mathbf{z}_{\mathbf{B}} \end{bmatrix} = \begin{bmatrix} \mathbf{F} \\ \mathbf{0} \\ \mathbf{0} \end{bmatrix} \quad (6.33)$$

Equations (6.33) are the equations of motion for the tensegrity cell incorporating viscoelastic elements and include the internal degrees of freedom  $\mathbf{z}_{\mathbf{A}}$  and  $\mathbf{z}_{\mathbf{B}}$ , which account for the frequency dependence of the material's properties, while doing away with internal degrees of freedom associated with rigid body (zero stiffness) modes. The equations may be solved directly for a single cell, or alternatively, the augmented mass, damping and stiffness matrices can be computed for a given design and used as the element matrices in a finite element analysis. In the latter case, it is common practice to use one of the model reduction techniques, *e.g.*, Guyan reduction or static condensation, to eliminate the internal degrees of freedom and retain the structural ones, thereby reducing the system's order and improving computational efficiency [181]. However, since this is not a significant concern for the current study, and in order not to lose any of the dynamic information included in the model, we choose to keep and use the augmented system equations and ensuing element matrices.

## 6.6 Steady-state Response to Harmonic Excitation

We cast the equations of motion (6.33) in state-space formulation, by defining the state vector  $Q$ :

$$Q = [\mathbf{W} \quad \mathbf{z}_{\mathbf{A}} \quad \mathbf{z}_{\mathbf{B}} \quad \dot{\mathbf{W}} \quad \dot{\mathbf{z}}_{\mathbf{A}} \quad \dot{\mathbf{z}}_{\mathbf{B}}]^T,$$

which yields the matrix state equation:

$$\dot{Q} = \begin{bmatrix} 0 & I \\ -\mathbf{M}_{aug}^{-1}\mathbf{K}_{aug} & -\mathbf{M}_{aug}^{-1}\mathbf{C}_{aug} \end{bmatrix} Q + \begin{bmatrix} 0 \\ \mathbf{M}_{aug}^{-1}\mathbf{F} \end{bmatrix} \equiv A Q + B f \quad (6.34)$$

Next, we assume a harmonic force being applied at an angular velocity  $\omega$ , resulting in a harmonic displacement, *i.e.*,  $f = f_0 e^{i\omega t}$  and  $Q = Q_0 e^{i\omega t}$ , where  $Q_0$  will be complex, *i.e.*, phase-shifted with respect to the input, due to the damping matrix. Noting that  $\dot{Q} = i\omega Q$ , we can write

$$(i\omega I - A)Q = Bf$$

Therefore,

$$Q_0 = (i\omega I - A)^{-1} B f_0$$

In order to investigate the stiffness and damping of the unit cell, we apply a unit force at the top node ( $f_0 = [0 \ 0 \ 1]^T$ ), constrain the bottom node to eliminate the rigid body mode ( $w_A = \dot{w}_A = 0$ ) which will result in the elimination of the corresponding rows and vectors from the state matrix, and solve for the displacement of the top node.

## 6.7 Bloch Analysis of the Periodic Structure

Having derived the linear equations of motion of the unit cell (equations (6.33) for the case of viscoelastic flexible elements, or (6.19) for purely elastic ones), we can now investigate the dynamics of a periodic structure consisting of repeating cells along the vertical axis. Following Floquet-Bloch's method, we assume a wave propagating through the structure with a propagation constant  $\mu$  and an angular frequency  $\omega$ , which undergoes the same change in magnitude from one cell to the next. From the periodicity of the structure, we can write:

$$w_C e^{i\omega t} = w_A e^{\mu} e^{i\omega t} \quad (6.35)$$

For a wave propagating without attenuation, the propagation constant can be written as

$$\mu = i\beta, \beta \in [0, 2\pi]$$

where  $\beta$  is the phase constant.

Defining the vector of augmented degrees of freedom – for the viscoelastic case with 2 mini-oscillators – as:

$$\mathbf{p} = [\mathbf{W} \quad \mathbf{z}_A \quad \mathbf{z}_B]^T \quad (6.36)$$

We can then define the vector of reduced degrees of freedom

$$\mathbf{p}^R = [\mathbf{W}^R \quad \mathbf{z}_A \quad \mathbf{z}_B]^T \quad (6.37)$$

where  $\mathbf{W}^R = [w_A \quad w_B]^T$ , the two vectors being related by the transformation:

$$\mathbf{p} = \begin{bmatrix} 1 & 0 & & \\ 0 & 1 & \mathbf{0} & \mathbf{0} \\ e^{i\beta} & 0 & & \\ \mathbf{0} & & \mathbf{I} & \mathbf{0} \\ \mathbf{0} & & \mathbf{0} & \mathbf{I} \end{bmatrix} \mathbf{p}^R \equiv S \mathbf{p}^R \quad (6.38)$$

where  $S$  is the transformation matrix, itself a function of  $\beta$ . Substituting for  $\mathbf{p}$  in the original equations of motion (6.33), and pre-multiplying by  $S^H$  (where  $S^H$  is the conjugate transpose of  $S$ ). Defining the augmented force vector  $\mathbf{\Xi}$  as

$$\mathbf{\Xi} = [\mathbf{F} \quad \mathbf{0} \quad \mathbf{0}]^T \quad (6.39)$$

Equations (6.33) then become:

$$S^H \mathbf{M}_{\text{aug}} S \ddot{\mathbf{p}}^R + S^H \mathbf{C}_{\text{aug}} S \dot{\mathbf{p}}^R + S^H \mathbf{K}_{\text{aug}} S \mathbf{p}^R = S^H \mathbf{\Xi} \quad (6.40)$$

Or in a more compact notation:

$$M^P \ddot{\mathbf{p}}^R + C^P \dot{\mathbf{p}}^R + K^P \mathbf{p}^R = S^H \Xi \quad (6.41)$$

The right hand side evaluates to zero, and by casting the equations in state space formulation:

$$\frac{d}{dt} \begin{bmatrix} \mathbf{p}^R \\ \dot{\mathbf{p}}^R \end{bmatrix} = \begin{bmatrix} \mathbf{0} & \mathbf{I} \\ -M^{P-1} K^P & -M^{P-1} C^P \end{bmatrix} \begin{bmatrix} \mathbf{p}^R \\ \dot{\mathbf{p}}^R \end{bmatrix} \quad (6.42)$$

then making the substitutions

$$\begin{aligned} \dot{\mathbf{W}}^R &= i\omega \mathbf{W}^R \\ \ddot{\mathbf{W}}^R &= -\omega^2 \mathbf{W}^R \end{aligned} \quad (6.43)$$

The resulting eigenvalue problem can therefore be solved, for successive values of  $\beta$ , for the angular velocities of waves that will propagate without attenuation and, conversely, those that will be blocked.

## 6.8 Prototyping and Testing

### 6.8.1 Design and Assembly

Figure 6.5 shows a CAD model of the tensegrity damper unit cell. Since each of the four cylindrical joints must connect three elements (two flexible and one rigid), having all elements lie in the same plane would have significantly complicated the design, assembly and operation of the mechanism. A design decision was therefore made to break down each flexible element into two identical links, to be located symmetrically about the center plane of the cell. Therefore, looking at the cell from the side shows a rigid link located at the center, surrounded on each side by a flexible link representing “one half” of the first flexible element. Each of these links is, in turn, flanked by an identical link representing “one half” of the second flexible element. Each flexible half-link has a width equal to one half that of the rigid element.

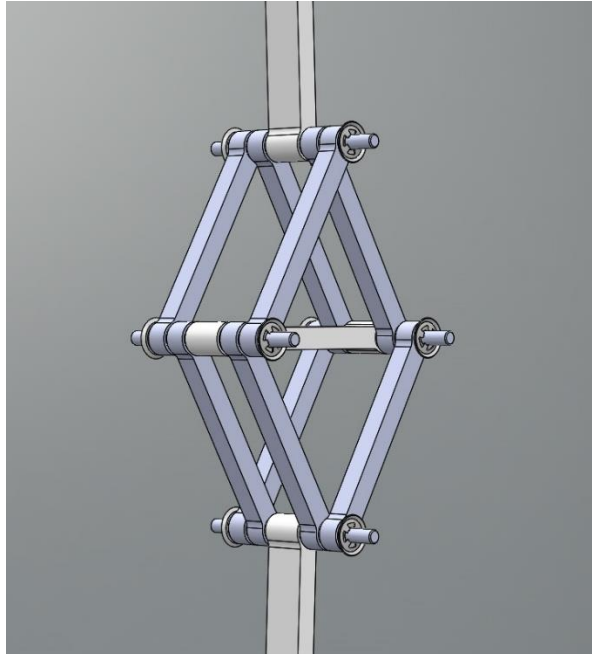


Figure 6.5 CAD model of tensegrity isolator cell

Several design iterations were explored, varying the dimensions and material properties and computing the resulting load-carrying capacity and vibration attenuation characteristics of the periodic array, while requiring that the overall size of both the unit cell and the array be suitable for testing purposes and keeping an eye on the available manufacturing methods and availability of standard parts. Ultimately the following design parameters were chosen:

- Length of rigid element =  $1.5 \text{ in}$
- Length of flexible element =  $0.866 \text{ in}$
- Cross section area of any element =  $0.4 \times 0.2 \text{ in}^2$
- Elastic modulus of the rigid elements' material should be approximately three orders of magnitude higher than that of the flexible elements' material.

## 6.8.2 Material Characterization and Selection

The rigid and flexible elements were 3D-printed from the CAD model on the 3D printer Objet 500® Connex3™ by Stratasys, which has the capability of printing rigid and rubber-like materials. A cylindrical rod (1/8" in diameter) was used as the joints' pivots on which the rigid and flexible elements are mounted with a clearance fit. Three PTFE washers (McMaster-Carr, item # 95630A235) were used as spacers between each two links at every joint. PTFE was chosen for its very low coefficient of friction, allowing for smooth relative motion between the various parts. Axial displacement along the joint was constrained using either a retaining ring or a nut.

### 6.8.2.1 Flexible members

Stratasys provides a number of rubber-like materials with the designations (Tango Black, FLX 9850-DM, FLX 9860-DM, FLX 9870-DM, FLX 9885-DM, FLX 9895-DM) ordered from the most to least flexible. With few material properties available from the manufacturer [176], we performed a dynamic mechanical thermal analysis to determine each flexible material's frequency dependent complex elastic modulus.

The characterization experiments were carried out using the DMTA system by Polymer Laboratories. Test specimens were rectangular strips  $60 \times 10 \times 2 \text{ mm}^3$ , 3D-printed from each of the five rubber-like materials. Each specimen was clamped in a single cantilever mode, flexural strain was applied isothermally over a range of frequencies, typically between 1 and 100 Hz, and the resulting force measured. Figure 6.6 shows a test specimen mounted on the DMTA device.

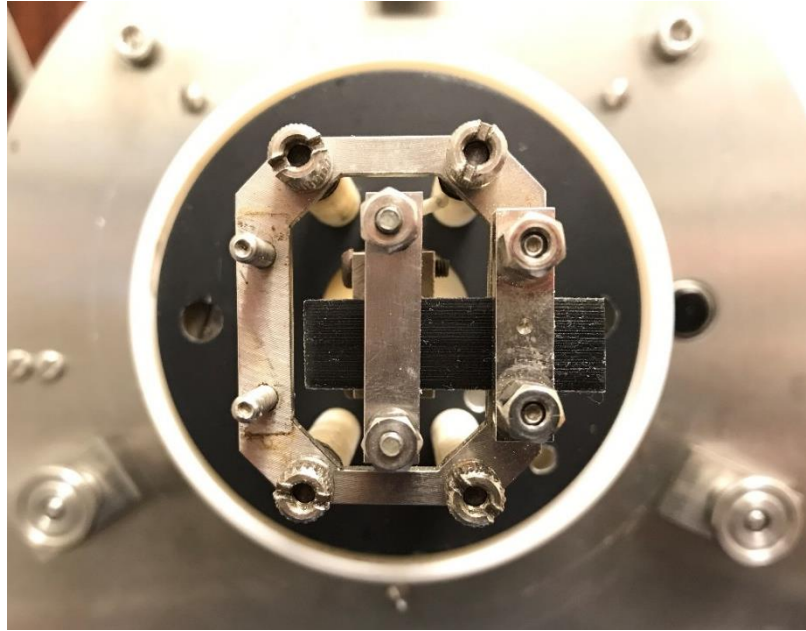


Figure 6.6 Viscoelastic sample mounted in DMTA holder

Samples made from the first three materials in the list above did not withstand testing and failed immediately. The storage modulus and loss factor of the three remaining materials, which we will refer to as samples C, D and E, respectively, are shown in Figure 6.7 and Figure 6.8, respectively, for tests conducted at 28°C, showing the frequency dependence of the storage modulus and loss factor.

Based on these results, we chose the sample C material (FLX 9870-DM) to create the flexible elements since it has the lowest measured storage modulus and the highest loss factor. The density of the material was also computed by measuring the mass and volume of the samples and was found to be  $1143 \text{ kg/m}^3$ .

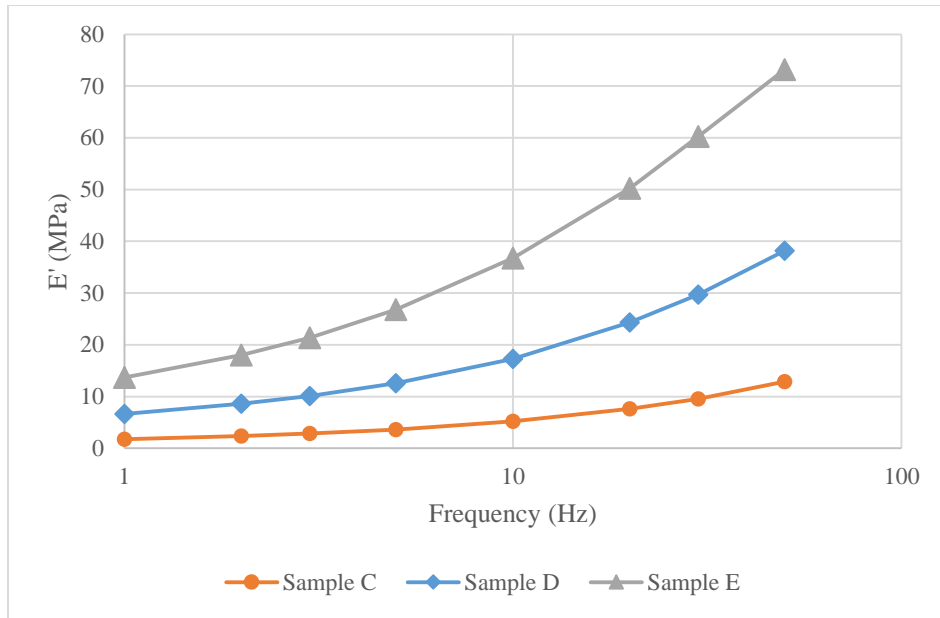


Figure 6.7 Storage modulus of rubber-like materials

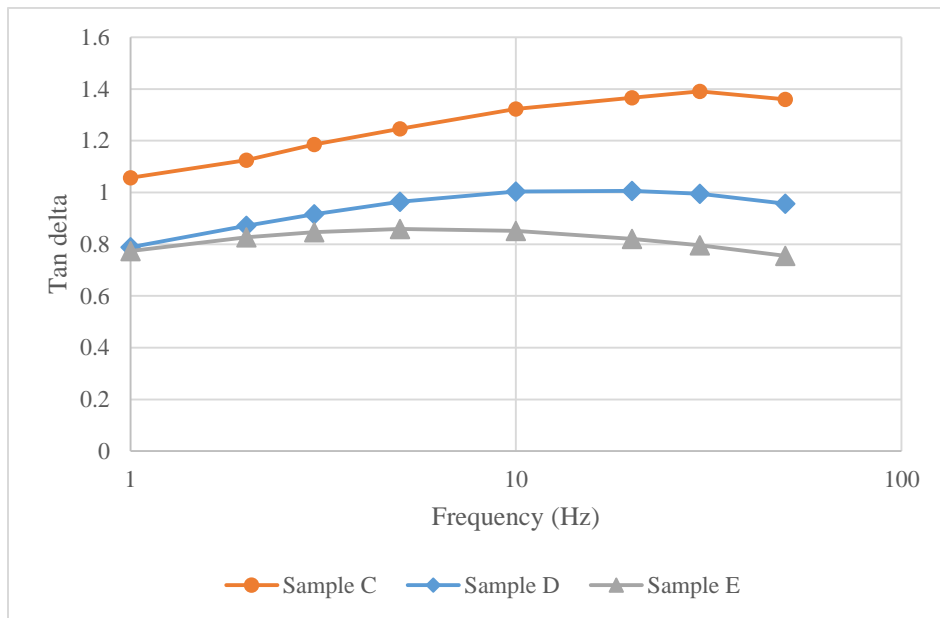


Figure 6.8 Loss modulus of rubber-like materials



### 6.8.2.2 Rigid Members

The rigid members were chosen to be made of the VeroWhite Plus material, which is reported to have a modulus of elasticity of 2500 MPa, a flexural modulus of 2700 MPa, a maximum elongation at break of 10%-25%, and a density of 1175 kg/m<sup>3</sup> [175].

We performed DMTA testing on material samples using the device and procedure described above, yielding the storage modulus and loss factor shown in Figure 6.9 for tests conducted at 28°C. We note that the storage modulus is less than half the value reported for the elastic modulus; this observation was corroborated with three other samples tested over a range of temperatures and frequencies, all yielding similar results. We hypothesize that this discrepancy may be due to material anisotropy and/or specific print settings. Noting that the rigid material’s storage modulus is almost three orders of magnitude higher than that of the flexible material, we are content with the “perfectly rigid” assumption made in the mathematical model earlier.

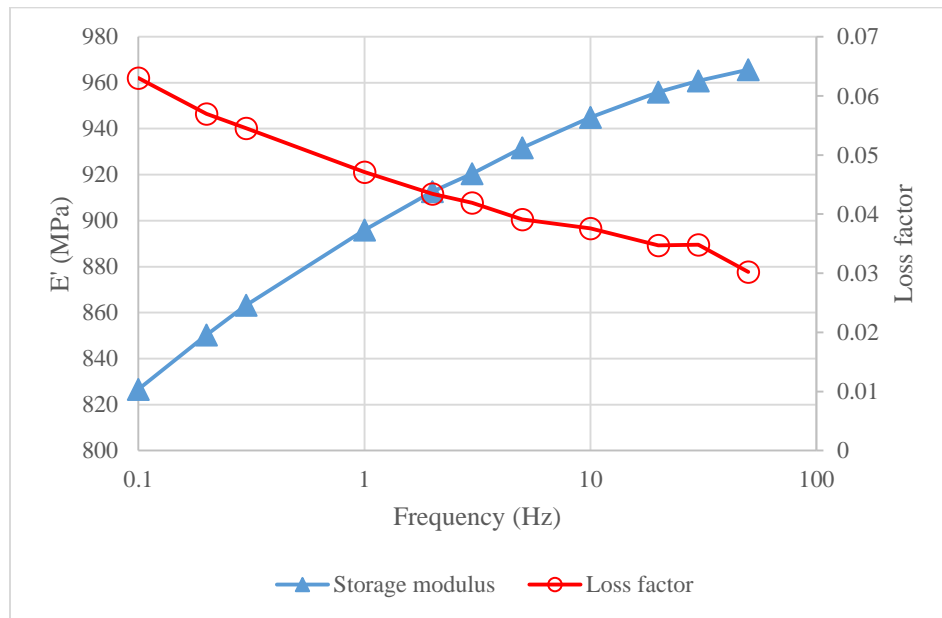


Figure 6.9 Storage modulus of rigid material

### 6.8.3 GHM Model Parameters

A MATLAB program was developed to select the GHM model parameters that would approximate the experimental results of the selected material by solving the multi-parameter optimization problem:

$$\begin{aligned} \text{minimize } F &= \sum_{\omega} \left\{ \left( \frac{E'}{E'_{exp}} - 1 \right)^2 + \left( \frac{\eta}{\eta_{exp}} - 1 \right)^2 \right\} \\ &\text{subject to } \alpha_i, \zeta_i, \omega_i > 0 \\ E(\omega \rightarrow \infty) &= E_0 \left( 1 + \sum_{i=1}^N \alpha_i \right) \\ &\text{where } E_0 = E(\omega = 0) \end{aligned}$$

The optimization problem was repeatedly solved with different initial guesses and with an increasing number of mini-oscillators and it was found that six mini-oscillators provided a very good approximation with a total error for the objective function of 0.07. The predicted data points are shown in Figure 6.10 against the experimental data, with the corresponding model given by:

$$E = E_0 \left[ 1 + \sum_{i=1}^6 \alpha_i \frac{s^2 + 2\zeta_i \omega_i s}{s^2 + 2\zeta_i \omega_i s + \omega_i^2} \right]$$

$$\begin{aligned} \alpha_1 &= 1.770 & \zeta_1 &= 81.4219 & \omega_1 &= 2939.5 \text{ rad/s} \\ \alpha_2 &= 7.282 & \zeta_2 &= 0.67670 & \omega_2 &= 152.44 \text{ rad/s} \\ \alpha_3 &= 0.0092 & \zeta_3 &= 0.00033 & \omega_3 &= 628.35 \text{ rad/s} \\ \alpha_4 &= 2.1646 & \zeta_4 &= 0.00135 & \omega_4 &= 161.85 \text{ rad/s} \\ \alpha_5 &= 0.0241 & \zeta_5 &= 0.00083 & \omega_5 &= 314.36 \text{ rad/s} \\ \alpha_6 &= 0.3813 & \zeta_6 &= 0.00342 & \omega_6 &= 190.93 \text{ rad/s} \end{aligned}$$

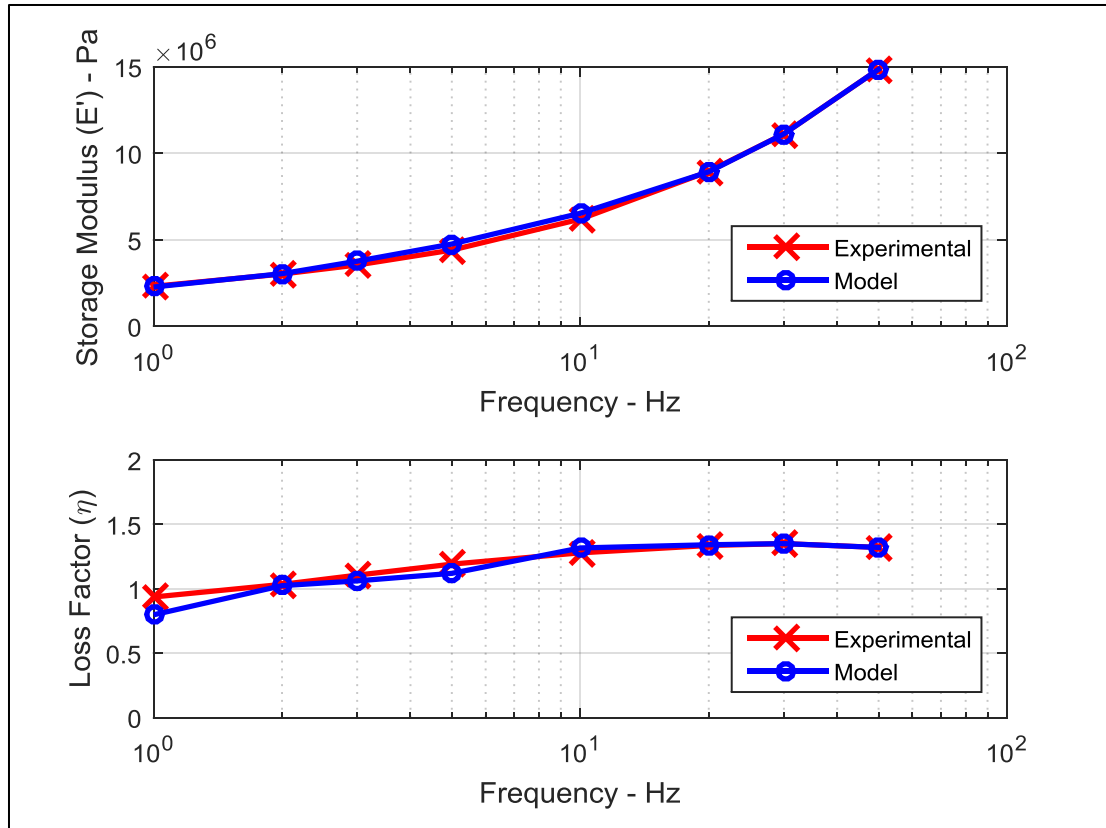


Figure 6.10 Storage modulus and loss factor – GHM model vs experiment

## 6.9 Unit Cell Testing and Characterization

Figure 6.11 shows a tensegrity damper unit cell mounted on a universal testing machine (Interlaken Series 3300) for the purpose of investigating its mechanical properties (equivalent stiffness and damping) and validating the mathematical model. Lateral motion of the cell is constrained by means of two acrylic blocks, one inch thick, located on both sides of the cell and oil-lubricated to allow for smooth vertical motion.

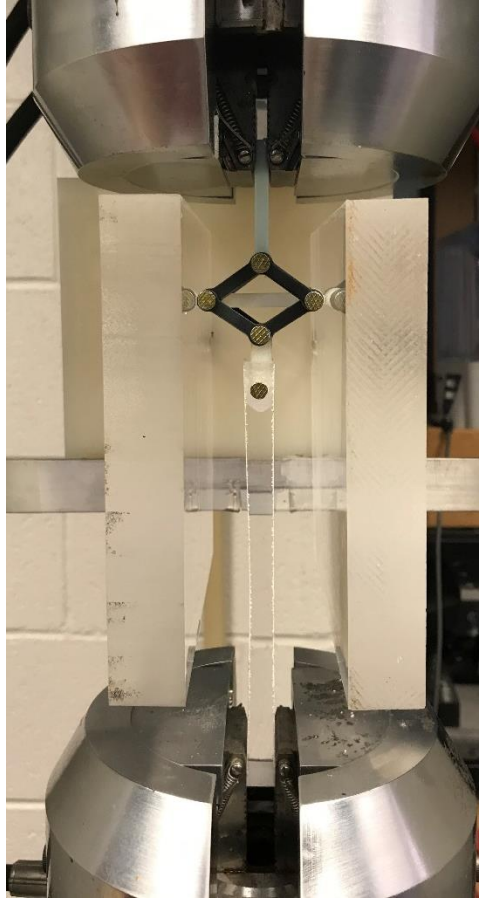


Figure 6.11 Tensegrity damper prototype on UTM machine

With the upper grip stationary, a prescribed displacement is applied on the specimen through the lower grip while a load cell (in the same grip) captures the force necessary to produce the displacement. The force-displacement plot thus obtained for a sinusoidal displacement function,  $2\text{ Hz}$  in frequency and  $0.1\text{ inch}$  in amplitude, is shown in Figure 6.12, overlaid on the one obtained from solving equations (6.34) for the given dimensions, material parameters and operating conditions, with the top node constrained ( $w_C = 0$ ) and the bottom node, C, at which the displacement is sought, loaded.

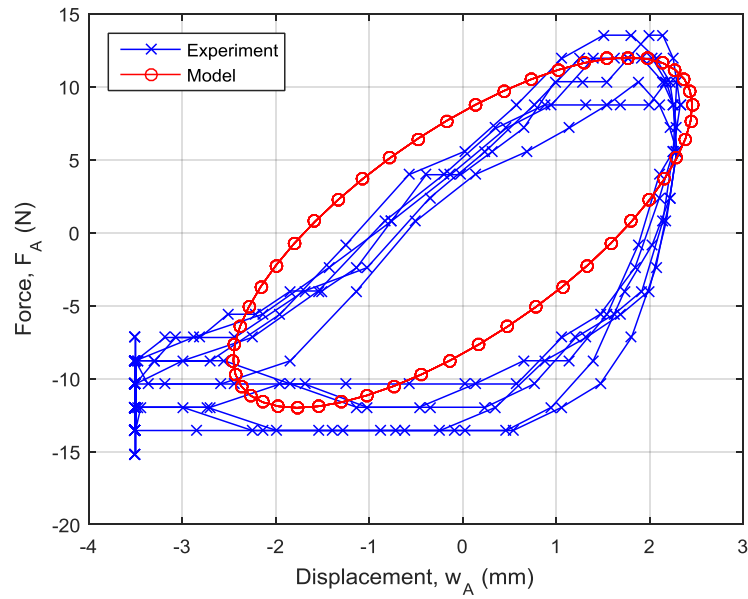


Figure 6.12 Experimental and predicted force-deflection plot

Looking closely at the plots, it can be seen that both curves, which appear similar, exhibit hysteresis which is representative of the energy dissipation that occurs in the viscoelastic elements. Moreover, it is possible to estimate from the experimental plot the equivalent stiffness and damping of the cell. The stiffness is equal to the slope of the force-displacement plot, which we take as the slope of the major axis of the hysteresis loop, estimated to be

$$K_{eq} = 4800 \text{ N/m}.$$

The area enclosed by the hysteresis loop in the plot is the energy dissipated in one cycle,  $D$ , which in turn is related to the equivalent damping coefficient of the system,  $C$ , by the equation

$$D = \pi C \omega X_0^2$$

where  $\omega$  is the angular velocity and  $X_0$  is the amplitude of the response [182]. For  $D \approx 55 \text{ N mm}$ ,  $\omega = 2 \times 2\pi \text{ rad/s}$ , and  $X_0 = 2.5 \text{ mm}$ , the equivalent damping coefficient of the system is estimated to be

$$C_{eq} = 223 \text{ Ns/m}$$

Comparing the experimentally-obtained stiffness and damping coefficient to those obtained from the numerical model, which are  $4500 \text{ N/m}$  and  $243 \text{ Ns/m}$ , respectively, we find the errors to be 6.7% and 8.2%, respectively, which – in our opinion – indicates a good agreement between the linearized mathematical model and the experiment. There is, however, one discrepancy between the two, namely the inability of the cell to resist compressive loads beyond a certain limit, found from Figure 6.12 to be approximately  $-13 \text{ N}$ . This was addressed in Section 6.4 as being the result of a geometric nonlinearity of the structure, and of which it is important to be mindful when designing or modeling such a damper.

## 6.10 Vibration Testing of Periodic Array

Figure 6.13 shows a periodic array of six tensegrity damper units, interconnected with rigid links, the whole driven by a shaker from one end, with the opposite end fixed to a massive block. Two Nylon bars located on either side of the array provide the sliding boundary conditions for the assembly. The array is excited using the shaker over a range of frequencies, and accelerometers (Kistler model 8616A500 and PCB Piezotronics model 352C68) are used to measure the acceleration at various points. The axial position of the massive block can be adjusted prior to the beginning of the experiment to adjust the pre-tension of the cells' elements.



Figure 6.13 Periodic tensegrity damper vibration test rig

Defining the transmissibility of the array as the ratio of the displacement of the last (rightmost) rigid cross-link,  $w_{out}$ , to the displacement of the shaker plate,  $w_{in}$ , Figure 6.14 shows a plot of the transmissibility over the frequency range, in which it is seen to undergo a large drop of more than 25 dB between 1700 Hz and 2200 Hz, and another, albeit smaller, drop between 3800 Hz and 4300 Hz.

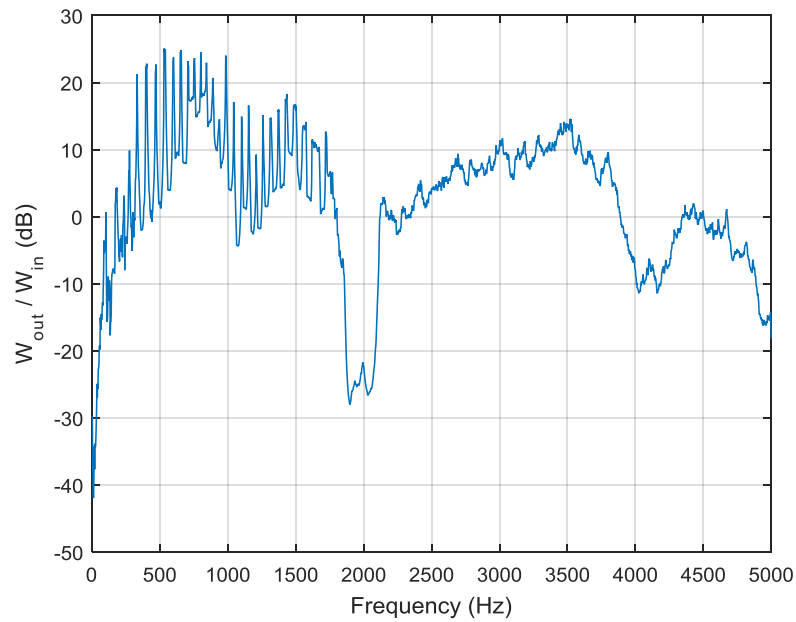


Figure 6.14 Experimental transmissibility of tensegrity damper array

Figure 6.15 shows the dispersion curves obtained by Bloch analysis of an infinite periodic array using the equations derived in Section 6.7, featuring a stop band in the range (1700-2200 Hz). Meanwhile, Figure 6.16 is a plot of the transmissibility as predicted by a finite element simulation for an array of six cells and shows a large drop in transmissibility within the same range. Comparison of the experimental results with the numerical data reveals that the first observed stop band is accurately predicted by both models, while the second stop band (3800-4300 Hz) does not show up in either simulation.

We believe that this second stop band is not the result of Bragg scattering (the primary mechanism responsible for the creation of stop bands in periodic structures and which can be predicted using Bloch's theorem), but is rather due to *localization* – the confinement of the disturbance to locations close to the source due to the presence of some disorder into the array (see, *e.g.*, [106, 116]). This deviation from perfect periodicity (which may be due to some cells being stretched more than others, some of the connecting links not being perfectly aligned, or the introduction of asymmetries during assembly, etc.) prevents the propagation of vibrations to the other end of the damper, resulting in the second observed stop band.



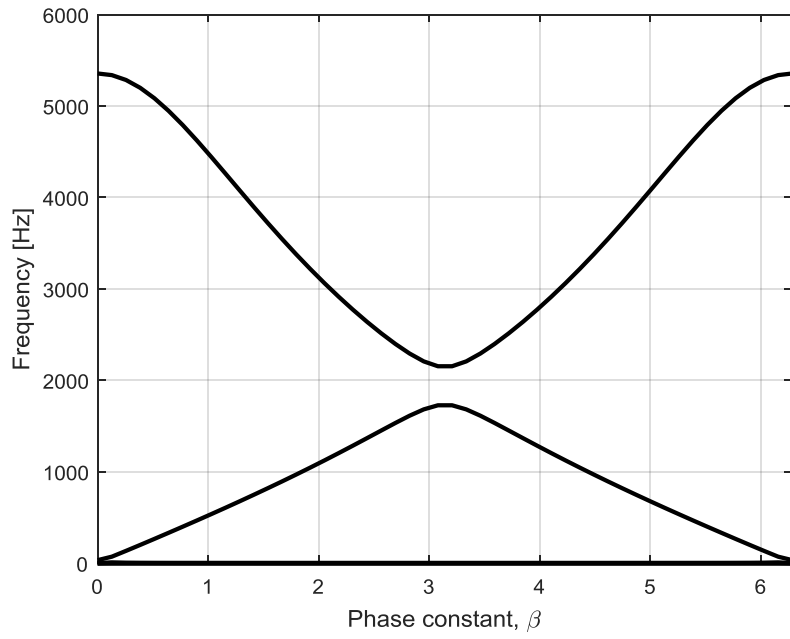


Figure 6.15 Dispersion curves for periodic tensegrity damper

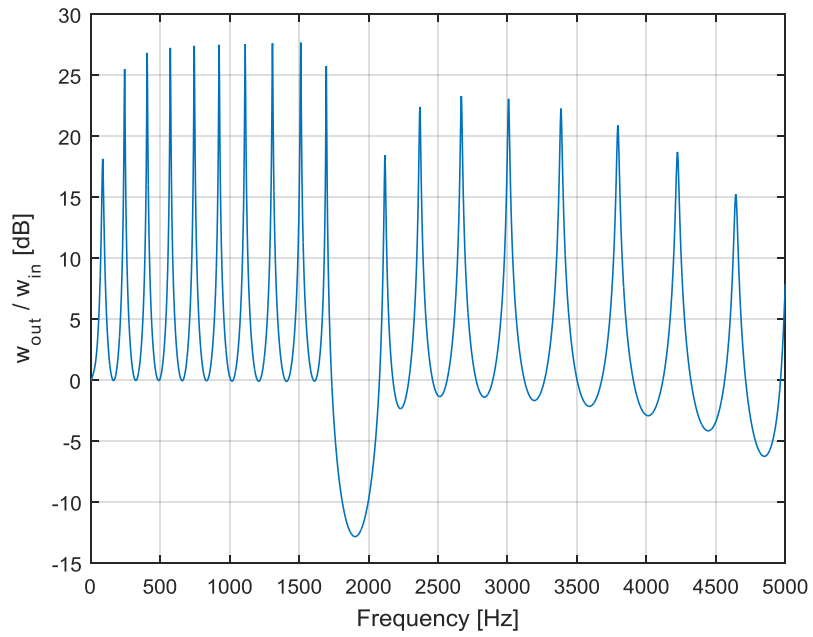


Figure 6.16 Finite element simulation

## 6.11 Summary

In this chapter, we proposed a design for a new tensegrity-based damper that demonstrates favorable load carrying, damping and wave attenuation characteristics. We developed an analytical model for the structure and performed static and dynamic simulations, including wave propagation using Bloch's method which predicted the presence of frequency stop bands.

The designs were manufactured by 3D-printing from rigid and viscoelastic materials, which were characterized using DMTA testing with the experimentally-obtained parameters incorporated into the mathematical models.

The resulting devices were tested – in tension/compression and under dynamic loading – and demonstrated good agreement with the numerical predictions, including the presence of stop bands, suggesting the promise of such devices as mechanical vibration isolators.

## **Chapter 7: Original Contributions and Future Work**

### **7.1 Overview**

This chapter summarizes the major contributions of the dissertation in relation to the current state-of-the-art, as well as provides some suggestions for future work.

### **7.2 Major Contributions of the Dissertation**

This dissertation has presented the concept of periodic tensegrity structures along with their performance characteristics.

The comprehensive presentation of the periodic tensegrity structures through mathematical modeling of the static, dynamic characteristics of these structures combined with experimental validation of some of these models emphasizes the following major contributions of the work to the current state-of-the-art of periodic structures:

1. The concept of periodic tensegrity structures as mechanical filters for controlling the wave propagation is original and has not been considered at all in the open-literature for application to tensegrity systems.
2. The comprehensive theoretical demonstration of the wave propagation and band gap characteristics of the concept of periodic/tensegrity structures is one of the major contributions of this dissertation.
3. The ability of the periodic tensegrity structures in the simultaneous control of wave propagation in multi-directional systems is another important contribution of the dissertation.

4. Demonstration of important and very interesting elastic properties of the periodic/tensegrity structures. Among these properties is the ratio of the bulk modulus to the shear modulus which are shown to be on the order of 1000. These values are two orders of magnitude higher than any naturally-occurring bulk material, suggesting that the viable potential of the periodic/tensegrity structures as suitable candidates for the synthesis of practical and realizable “*pentamode*” metamaterials, with many potential applications in the novel areas of acoustic and elastic cloaking where the proposed periodic/tensegrity structures act as liquids to ensure proper impedance matching.
5. The design, realization and testing of a tensegrity-based damper/vibration isolator is new; and the wave attenuation abilities which have been verified numerically and experimentally, show promise as mechanical filters, in addition to their ease of manufacturing and assembly.
6. Modeling of viscoelastic elements within the context of tensegrity structures has not been tackled before, which together with the analysis of periodic tensegrity structures using Bloch’s method represent an original contribution to the state-of-the-art.

### 7.3 Future Work

**a. The development of the homogenized properties of the periodic/tensegrity structures:**

Based on the work of Martinsson and co-workers [183-185], the continuum equivalent representation for the discrete periodic/tensegrity structure could be pursued with the objective of retaining information regarding the local properties of the unit cell, while condensing its global behavior. Following this approach, the continuum-homogenized model involves a significantly lower number of variables than those required for the detailed model of the assembly, which would enable the predictions of the propagation of vibration and acoustic waves in a computationally efficient manner.

**b. An in-depth understanding of the 3D printing process and characterization of the materials and structures:**

As was pointed out in Section 3.6.3, the materials used to prototype the cells may feature anisotropic elastic moduli leading to inconsistencies with the nominal/modelled material properties. Moreover, printing structures with more than one material will probably involve different curing temperatures and thermal expansion coefficients. Therefore, a deeper understanding of the material properties and the physics of the printing process will enable researchers to properly characterize the 3D-printed structures and adopt a robust manufacturing and design processes.

**c. Physical realization and testing of tunable wave-blocking tensegrity structure:**

Capitalizing on the presented 1D and 2D tensegrity arrays which feature wave attenuation characteristics, *e.g.*, in Chapters 5 and 6, further work could go into the design of tunable versions of these arrays, able to move their frequency stop bands to coincide with desired operating conditions. A recent paper [76] demonstrated the shape memory properties of some 3D printed polymers and their applicability to tensegrity structures, which could therefore be a mechanism to tune such structure. Other techniques include micro-actuators and pneumatic control.



## Appendix B: Finite Element Formulation of Pre-stressed Bar and Tendon Elements

The element stiffness matrix of a two-node, constant cross-section bar element in three dimensions, assuming the element is oriented along the X-axis and subject to pre-stress is (generalized from the two-dimensional case in [186]):

$$K = \begin{bmatrix} \frac{EA}{L} & 0 & 0 & -\frac{EA}{L} & 0 & 0 \\ 0 & \frac{P}{L} & 0 & 0 & -\frac{P}{L} & 0 \\ 0 & 0 & \frac{P}{L} & 0 & 0 & -\frac{P}{L} \\ -\frac{EA}{L} & 0 & 0 & \frac{EA}{L} & 0 & 0 \\ 0 & -\frac{P}{L} & 0 & 0 & \frac{P}{L} & 0 \\ 0 & 0 & -\frac{P}{L} & 0 & 0 & \frac{P}{L} \end{bmatrix}$$

where  $E$ ,  $A$ , and  $L$  are the element's Young's modulus, cross-section area, and length, respectively, and  $P$  is the pre-stress load on the element (positive for tension).

The Mass matrix is

$$M = \frac{m}{6} \begin{bmatrix} 2 & 0 & 0 & 1 & 0 & 0 \\ 0 & 2 & 0 & 0 & 1 & 0 \\ 0 & 0 & 2 & 0 & 0 & 1 \\ 1 & 0 & 0 & 2 & 0 & 0 \\ 0 & 1 & 0 & 0 & 2 & 0 \\ 0 & 0 & 1 & 0 & 0 & 2 \end{bmatrix}$$

where  $m$  is the element's mass.



## Appendix C: Derivation of Equations of Motion for Tensegrity Damper Unit Cell

Starting with the kinetic and potential energies of each element as derived in Section 6.3:

$$T_{AB} = \frac{1}{2} m_1 \dot{y}_A \dot{y}_B + \frac{1}{6} m_1 \left( \frac{a}{l_1} \right)^2 (\dot{y}_B - \dot{y}_A)^2 \quad V_{AB} = \frac{1}{2} K_1 (l_1 - l_0)^2$$

$$T_{AD} = \frac{1}{2} m_2 \dot{y}_A \dot{y}_B + \frac{1}{6} m_2 \left( \frac{a}{l_2} \right)^2 (\dot{y}_B - \dot{y}_A)^2 \quad V_{AD} = \frac{1}{2} K_2 (l_2 - l_0)^2$$

$$T_{BC} = \frac{1}{2} m_3 \dot{y}_B \dot{y}_C + \frac{1}{6} m_3 \left( \frac{a}{l_3} \right)^2 (\dot{y}_C - \dot{y}_B)^2 \quad V_{BC} = \frac{1}{2} K_3 (l_3 - l_0)^2$$

$$T_{CD} = \frac{1}{2} m_4 \dot{y}_B \dot{y}_C + \frac{1}{6} m_4 \left( \frac{a}{l_4} \right)^2 (\dot{y}_C - \dot{y}_B)^2 \quad V_{CD} = \frac{1}{2} K_4 (l_4 - l_0)^2$$

$$T_{BD} = \frac{1}{2} m_5 \dot{y}_B^2 \quad V_{BD} = 0$$

$$T_{CE} = \frac{1}{2} m_6 \dot{y}_C^2 \quad V_{CE} = 0$$

The Lagrangian of the unit cell is given by

$$\mathcal{L} = \Sigma T - \Sigma V$$

The resulting expression is substituted into Lagrange's equation and derivations are carried out for each of the three generalized coordinates  $(y_A, y_B, y_C)$ .

$$\frac{d}{dt} \left( \frac{\partial \mathcal{L}}{\partial \dot{q}} \right) - \frac{\partial \mathcal{L}}{\partial q} = F$$

Before delving into Lagrange's equations, we first note that for the representative flexible element shown in Figure 6.3:

$$l = \sqrt{(y_N - y_M)^2 + a^2}$$

$$\frac{\partial l}{\partial y_N} = -\frac{\partial l}{\partial y_M} = \frac{1}{2\sqrt{(y_N - y_M)^2 + a^2}} 2(y_N - y_M) = \frac{1}{l} (y_N - y_M)$$

$$\frac{\partial l}{\partial \dot{y}_N} = \frac{\partial l}{\partial \dot{y}_M} = 0$$

$$\frac{dl}{dt} = \frac{1}{2\sqrt{(y_N - y_M)^2 + a^2}} 2(y_N - y_M)(\dot{y}_N - \dot{y}_M) = \frac{1}{l}(y_N - y_M)(\dot{y}_N - \dot{y}_M)$$

**1. The first equation of motion ( $q_1 = y_A$ ):**

$$\frac{\partial \mathcal{L}}{\partial \dot{y}_A} = \frac{1}{2} m_1 \dot{y}_B - \frac{1}{3} m_1 \left(\frac{a}{l_1}\right)^2 (\dot{y}_B - \dot{y}_A) + \frac{1}{2} m_2 \dot{y}_B - \frac{1}{3} m_2 \left(\frac{a}{l_2}\right)^2 (\dot{y}_B - \dot{y}_A)$$

$$\begin{aligned} \frac{d}{dt} \left( \frac{\partial \mathcal{L}}{\partial \dot{y}_A} \right) &= \frac{1}{2} (m_1 + m_2) \ddot{y}_B - \frac{1}{3} m_1 \left(\frac{a}{l_1}\right)^2 (\ddot{y}_B - \ddot{y}_A) - \frac{1}{3} m_1 a^2 \left(\frac{-2}{l_1^3}\right) \frac{dl_1}{dt} (\dot{y}_B - \dot{y}_A) \\ &\quad - \frac{1}{3} m_2 \left(\frac{a}{l_2}\right)^2 (\ddot{y}_B - \ddot{y}_A) - \frac{1}{3} m_2 a^2 \left(\frac{-2}{l_2^3}\right) \frac{dl_2}{dt} (\dot{y}_B - \dot{y}_A) \\ &= \frac{1}{2} (m_1 + m_2) \ddot{y}_B - \frac{1}{3} m_1 \left(\frac{a}{l_1}\right)^2 (\ddot{y}_B - \ddot{y}_A) + \frac{2}{3} m_1 \frac{a^2}{l_1^4} (y_B - y_A) (\dot{y}_B - \dot{y}_A)^2 \\ &\quad - \frac{1}{3} m_2 \left(\frac{a}{l_2}\right)^2 (\ddot{y}_B - \ddot{y}_A) + \frac{2}{3} m_2 \frac{a^2}{l_2^4} (y_B - y_A) (\dot{y}_B - \dot{y}_A)^2 \end{aligned}$$

$$\begin{aligned} \frac{\partial \mathcal{L}}{\partial y_A} &= \frac{1}{6} m_1 a^2 \left(\frac{-2}{l_1^3}\right) \frac{\partial l_1}{\partial y_A} (\dot{y}_B - \dot{y}_A)^2 - K_1 (l_1 - l_0) \frac{\partial l_1}{\partial y_A} + \frac{1}{6} m_2 a^2 \left(\frac{-2}{l_2^3}\right) \frac{\partial l_2}{\partial y_A} (\dot{y}_B - \dot{y}_A)^2 \\ &\quad - K_2 (l_2 - l_0) \frac{\partial l_2}{\partial y_A} \\ &= \frac{1}{3} m_1 \frac{a^2}{l_1^4} (y_B - y_A) (\dot{y}_B - \dot{y}_A)^2 + K_1 \frac{l_1 - l_0}{l_1} (y_B - y_A) + \frac{1}{3} m_2 \frac{a^2}{l_2^4} (y_B - y_A) (\dot{y}_B - \dot{y}_A)^2 \\ &\quad + K_2 \frac{l_2 - l_0}{l_2} (y_B - y_A) \end{aligned}$$

Substituting into the first Lagrange equation, noting that  $l_1 = l_2$ , yields the nonlinear equation:

$$\boxed{\begin{aligned} \frac{1}{2} (m_1 + m_2) \ddot{y}_B - \frac{1}{3} (m_1 + m_2) \frac{a^2}{l_1^2} (\ddot{y}_B - \ddot{y}_A) + \frac{1}{3} (m_1 + m_2) \frac{a^2}{l_1^4} (y_B - y_A) (\dot{y}_B - \dot{y}_A)^2 \\ - (K_1 + K_2) \frac{l_1 - l_0}{l_1} (y_B - y_A) = F_A \end{aligned}}$$

We expand the nonlinear terms on the left hand side using Taylor series expansion for small perturbations from equilibrium:

$$\begin{aligned} \{y_A = y_{A0} + w_A, y_B = y_{B0} + w_B, y_C = y_{C0} + w_C, \dot{y}_A = \dot{w}_A, \dot{y}_B = \dot{w}_B, \dot{y}_C = \dot{w}_C, \ddot{y}_A \\ = \ddot{w}_A, \ddot{y}_B = \ddot{w}_B, \ddot{y}_C = \ddot{w}_C\} \end{aligned}$$

- $\left(\frac{a}{l_1}\right)^2 (\dot{y}_B - \dot{y}_A) \approx 0 + \left(\frac{a}{l_0}\right)^2 (\ddot{w}_B - \ddot{w}_A) + HOT$
- $\frac{a^2}{l_1^4} (y_B - y_A)(\dot{y}_B - \dot{y}_A)^2 \approx 0 + HOT$
- $\frac{a^2}{l_1^4} (y_B - y_A)(\dot{y}_B - \dot{y}_A)^2 \approx 0 + HOT$
- $\frac{1}{l_1} (y_B - y_A) \approx \frac{1}{l_0} (y_{B0} - y_{A0}) + \left[\frac{1}{l_0} - \frac{1}{l_0^3} (y_{B0} - y_{A0})^2\right] (w_B - w_A) + HOT$   

$$= \frac{1}{l_0} (y_B - y_A) - \frac{1}{l_0} (\sin \alpha_0)^2 (w_B - w_A) + HOT$$

The first Lagrange equation, linearized about the equilibrium, is therefore:

$$\boxed{\frac{1}{2} (m_1 + m_2) \ddot{w}_B - \frac{1}{3} (m_1 + m_2) \left(\frac{a}{l_0}\right)^2 (\ddot{w}_B - \ddot{w}_A) - (K_1 + K_2) (\sin \alpha_0)^2 (w_B - w_A) = F_A}$$

## 2. The second equation of motion ( $q_2 = y_B$ ):

$$\begin{aligned} \frac{\partial \mathcal{L}}{\partial \dot{y}_B} &= \frac{1}{2} (m_1 + m_2) \dot{y}_A + \frac{1}{2} (m_3 + m_4) \dot{y}_C + m_5 \dot{y}_B + \frac{1}{3} m_1 \left(\frac{a}{l_1}\right)^2 (\dot{y}_B - \dot{y}_A) \\ &\quad + \frac{1}{3} m_2 \left(\frac{a}{l_2}\right)^2 (\dot{y}_B - \dot{y}_A) - \frac{1}{3} m_3 \left(\frac{a}{l_3}\right)^2 (\dot{y}_C - \dot{y}_B) \\ &\quad - \frac{1}{3} m_4 \left(\frac{a}{l_4}\right)^2 (\dot{y}_C - \dot{y}_B) \end{aligned}$$

$$\begin{aligned} \frac{d}{dt} \left( \frac{\partial \mathcal{L}}{\partial \dot{y}_B} \right) &= \frac{1}{2} (m_1 + m_2) \ddot{y}_A + m_5 \ddot{y}_B + \frac{1}{2} (m_3 + m_4) \ddot{y}_C + \frac{1}{3} m_1 \left(\frac{a}{l_1}\right)^2 (\ddot{y}_B - \ddot{y}_A) \\ &\quad + \frac{1}{3} m_2 \left(\frac{a}{l_2}\right)^2 (\ddot{y}_B - \ddot{y}_A) - \frac{1}{3} m_3 \left(\frac{a}{l_3}\right)^2 (\ddot{y}_C - \ddot{y}_B) - \frac{1}{3} m_4 \left(\frac{a}{l_4}\right)^2 (\ddot{y}_C - \ddot{y}_B) \\ &\quad - \frac{2}{3} m_1 \left(\frac{a^2}{l_1^3}\right) \frac{dl_1}{dt} (\dot{y}_B - \dot{y}_A) - \frac{2}{3} m_2 \left(\frac{a^2}{l_2^3}\right) \frac{dl_2}{dt} (\dot{y}_B - \dot{y}_A) \\ &\quad + \frac{2}{3} m_3 \left(\frac{a^2}{l_3^3}\right) \frac{dl_3}{dt} (\dot{y}_C - \dot{y}_B) + \frac{2}{3} m_4 \left(\frac{a^2}{l_4^3}\right) \frac{dl_4}{dt} (\dot{y}_C - \dot{y}_B) \end{aligned}$$

$$\begin{aligned} &= \frac{1}{2} (m_1 + m_2) \ddot{y}_A + m_5 \ddot{y}_B + \frac{1}{2} (m_3 + m_4) \ddot{y}_C + \frac{1}{3} m_1 \left(\frac{a}{l_1}\right)^2 (\ddot{y}_B - \ddot{y}_A) \\ &\quad + \frac{1}{3} m_2 \left(\frac{a}{l_2}\right)^2 (\ddot{y}_B - \ddot{y}_A) - \frac{1}{3} m_3 \left(\frac{a}{l_3}\right)^2 (\ddot{y}_C - \ddot{y}_B) - \frac{1}{3} m_4 \left(\frac{a}{l_4}\right)^2 (\ddot{y}_C - \ddot{y}_B) \\ &\quad - \frac{2}{3} m_1 \frac{a^2}{l_1^4} (y_B - y_A) (\dot{y}_B - \dot{y}_A)^2 - \frac{2}{3} m_2 \frac{a^2}{l_2^4} (y_B - y_A) (\dot{y}_B - \dot{y}_A)^2 \\ &\quad + \frac{2}{3} m_3 \frac{a^2}{l_3^4} (y_C - y_B) (\dot{y}_C - \dot{y}_B)^2 + \frac{2}{3} m_4 \frac{a^2}{l_4^4} (y_C - y_B) (\dot{y}_C - \dot{y}_B)^2 \end{aligned}$$

$$\begin{aligned}
\frac{\partial \mathcal{L}}{\partial y_B} &= \frac{1}{6} m_1 a^2 \left( \frac{-2}{l_1^3} \right) \frac{\partial l_1}{\partial y_B} (\dot{y}_B - \dot{y}_A)^2 + \frac{1}{6} m_2 a^2 \left( \frac{-2}{l_2^3} \right) \frac{\partial l_2}{\partial y_B} (\dot{y}_B - \dot{y}_A)^2 \\
&+ \frac{1}{6} m_3 a^2 \left( \frac{-2}{l_3^3} \right) \frac{\partial l_3}{\partial y_B} (\dot{y}_C - \dot{y}_B)^2 + \frac{1}{6} m_4 a^2 \left( \frac{-2}{l_4^3} \right) \frac{\partial l_4}{\partial y_B} (\dot{y}_C - \dot{y}_B)^2 \\
&- K_1 (l_1 - l_0) \frac{\partial l_1}{\partial y_B} - K_2 (l_2 - l_0) \frac{\partial l_2}{\partial y_B} - K_3 (l_3 - l_0) \frac{\partial l_3}{\partial y_B} \\
&- K_4 (l_4 - l_0) \frac{\partial l_4}{\partial y_B} \\
&= -\frac{1}{3} m_1 \frac{a^2}{l_1^4} (y_B - y_A) (\dot{y}_B - \dot{y}_A)^2 - \frac{1}{3} m_2 \frac{a^2}{l_2^4} (y_B - y_A) (\dot{y}_B - \dot{y}_A)^2 \\
&+ \frac{1}{3} m_3 \frac{a^2}{l_3^4} (y_C - y_B) (\dot{y}_C - \dot{y}_B)^2 + \frac{1}{3} m_4 \frac{a^2}{l_4^4} (y_C - y_B) (\dot{y}_C - \dot{y}_B)^2 \\
&- K_1 \frac{l_1 - l_0}{l_1} (y_B - y_A) - K_2 \frac{l_2 - l_0}{l_2} (y_B - y_A) + K_3 \frac{l_3 - l_0}{l_3} (y_C - y_B) \\
&+ K_4 \frac{l_4 - l_0}{l_4} (y_C - y_B)
\end{aligned}$$

We substitute into the second Lagrange equation, noting that  $l_1 = l_2$  and  $l_3 = l_4$ , resulting in the second nonlinear equation of motion:

$$\begin{aligned}
(m_1 + m_2) \left( \frac{1}{2} - \frac{1}{3} \frac{a^2}{l_1^2} \right) \ddot{y}_A + \left[ \frac{1}{3} (m_1 + m_2) \frac{a^2}{l_1^2} + \frac{1}{3} (m_3 + m_4) \frac{a^2}{l_3^2} + m_5 \right] \ddot{y}_B \\
+ (m_3 + m_4) \left( \frac{1}{2} - \frac{1}{3} \frac{a^2}{l_3^2} \right) \ddot{y}_C - \frac{1}{3} (m_1 + m_2) \frac{a^2}{l_1^4} (y_B - y_A) (\dot{y}_B - \dot{y}_A)^2 \\
+ \frac{1}{3} (m_3 + m_4) \frac{a^2}{l_3^4} (y_C - y_B) (\dot{y}_C - \dot{y}_B)^2 + (K_1 + K_2) \frac{l_1 - l_0}{l_1} (y_B - y_A) \\
- (K_3 + K_4) \frac{l_3 - l_0}{l_3} (y_C - y_B) = F_B + F_D
\end{aligned}$$

where  $F_B$  and  $F_D$  are the external vertical forces applied at nodes B and D, respectively.

Performing a Taylor series expansion of the nonlinear terms and truncating second and higher order terms, we obtain the second linearized equation of motion:

$$\begin{aligned}
\frac{1}{2} (m_1 + m_2) \ddot{w}_A + m_5 \ddot{w}_B + \frac{1}{2} (m_3 + m_4) \ddot{w}_C + \frac{1}{3} (m_1 + m_2) \left( \frac{a}{l_0} \right)^2 (\ddot{w}_B - \ddot{w}_A) \\
- \frac{1}{3} (m_3 + m_4) \left( \frac{a}{l_0} \right)^2 (\ddot{w}_C - \ddot{w}_B) + (K_1 + K_2) (\sin \alpha_0)^2 (w_B - w_A) \\
- (K_3 + K_4) (\sin \alpha_0)^2 (w_C - w_B) = F_B + F_D
\end{aligned}$$

**3. The third equation of motion ( $q_3 = y_C$ ):**

$$\frac{\partial \mathcal{L}}{\partial \dot{y}_C} = \frac{1}{2} m_3 \dot{y}_B + \frac{1}{3} m_3 \left( \frac{a}{l_3} \right)^2 (\dot{y}_C - \dot{y}_B) + \frac{1}{2} m_4 \dot{y}_B + \frac{1}{3} m_4 \left( \frac{a}{l_4} \right)^2 (\dot{y}_C - \dot{y}_B) + m_6 \dot{y}_C$$

$$\begin{aligned} \frac{d}{dt} \left( \frac{\partial \mathcal{L}}{\partial \dot{y}_C} \right) &= \frac{1}{2} (m_3 + m_4) \ddot{y}_B + m_6 \ddot{y}_C + \frac{1}{3} m_3 \left( \frac{a}{l_3} \right)^2 (\ddot{y}_C - \ddot{y}_B) \\ &\quad + \frac{1}{3} m_3 a^2 \left( \frac{-2}{l_3^3} \right) \frac{dl_3}{dt} (\dot{y}_C - \dot{y}_B) + \frac{1}{3} m_4 \left( \frac{a}{l_4} \right)^2 (\ddot{y}_C - \ddot{y}_B) \\ &\quad + \frac{1}{3} m_4 a^2 \left( \frac{-2}{l_4^3} \right) \frac{dl_4}{dt} (\dot{y}_C - \dot{y}_B) \\ &= \frac{1}{2} (m_3 + m_4) \ddot{y}_B + m_6 \ddot{y}_C + \frac{1}{3} m_3 \left( \frac{a}{l_3} \right)^2 (\ddot{y}_C - \ddot{y}_B) \\ &\quad - \frac{2}{3} m_3 \frac{a^2}{l_3^4} (y_C - y_B) (\dot{y}_C - \dot{y}_B)^2 + \frac{1}{3} m_4 \left( \frac{a}{l_4} \right)^2 (\ddot{y}_C - \ddot{y}_B) \\ &\quad - \frac{2}{3} m_4 \frac{a^2}{l_4^4} (y_C - y_B) (\dot{y}_C - \dot{y}_B)^2 \end{aligned}$$

$$\begin{aligned} \frac{\partial \mathcal{L}}{\partial y_C} &= \frac{1}{6} m_3 a^2 \left( \frac{-2}{l_3^3} \right) \frac{\partial l_3}{\partial y_C} (\dot{y}_C - \dot{y}_B)^2 - K_3 (l_3 - l_0) \frac{\partial l_3}{\partial y_C} + \frac{1}{6} m_4 a^2 \left( \frac{-2}{l_4^3} \right) \frac{\partial l_4}{\partial y_C} (\dot{y}_C - \dot{y}_B)^2 \\ &\quad - K_4 (l_4 - l_0) \frac{\partial l_4}{\partial y_C} \\ &= -\frac{1}{3} m_3 \frac{a^2}{l_3^4} (y_C - y_B) (\dot{y}_C - \dot{y}_B)^2 - K_3 \frac{l_3 - l_0}{l_3} (y_C - y_B) \\ &\quad - \frac{1}{3} m_4 \frac{a^2}{l_4^4} (y_C - y_B) (\dot{y}_C - \dot{y}_B)^2 - K_4 \frac{l_4 - l_0}{l_4} (y_C - y_B) \end{aligned}$$

We substitute into the third Lagrange equation, noting that  $l_3 = l_4$ , which yields the third equation of motion:

$$\begin{aligned} (m_3 + m_4) \left( \frac{1}{2} - \frac{1}{3} \frac{a^2}{l_3^2} \right) \ddot{y}_B + \frac{1}{3} (m_3 + m_4) \frac{a^2}{l_3^2} \ddot{y}_C \\ - \frac{1}{3} (m_3 + m_4) \frac{a^2}{l_3^4} (y_C - y_B) (\dot{y}_C - \dot{y}_B)^2 + (K_3 + K_4) \frac{l_3 - l_0}{l_3} (y_C - y_B) \\ = F_C \end{aligned}$$

where  $F_C$  is the external force applied vertically at node C.

Performing a Taylor series expansion of the nonlinear terms about the state of equilibrium and truncating second and higher order terms, we obtain the third equation of motion, linearized for small displacements:

$$\frac{1}{2}(m_3 + m_4)\ddot{w}_B + m_6\ddot{w}_C + \frac{1}{3}(m_3 + m_4)\left(\frac{a}{l_0}\right)^2(\ddot{w}_C - \ddot{w}_B) + (K_3 + K_4)(\sin \alpha_0)^2(w_C - w_B) = F_C$$

## Bibliography

1. Fuller, R.B., *Tensegrity*. Portfolio and Art News Annual, 1961. **4**.
2. Emmerich, D.G., *Structures tendues et autotendantes*. 1988: Ecole d'Architecture de Paris La Villette.
3. Gough, M., *In the laboratory of constructivism: Karl Ioganson's cold structures*. October, 1998: p. 91-117.
4. Nagy, L., *Von Materiel zu Architektur*. 1929: Bauhausbuecher.
5. Motro, R., *Tensegrity: structural systems for the future*. 2003: Elsevier.
6. Fuller, R.B., *Designing a new industry; a composite of a series of talks by R. Buckminster Fuller, 1945-1946*. 1946, Wichita, Kan.: Fuller Research Institute.
7. Snelson, K., *Snelson on the tensegrity invention*. International Journal of Space Structures, 1996. **11**(1-2): p. 43-48.
8. Snelson, K., *The art of tensegrity*. International Journal of Space Structures, 2012. **27**(2): p. 71-80.
9. Fuller, R.B., *Tensegrity*. Creative Science and Technology, 1981. **4**(3): p. 11.
10. Gough, M., *Backyard landing: three structures by Buckminster Fuller*, in *New Views on R. Buckminster Fuller*, C. Hsiao-Yun and G.T. Roberto, Editors. 2009, Stanford University Press: Stanford. p. 125-145.
11. Snelson, K., *Letter from Kenneth Snelson to R. Motro*. International Journal of Space Structures, 1990. **7**: p. N2.
12. Fuller, R.B., *Tensile-integrity structures*. 1962: United States. Patent No. 3063521.
13. Emmerich, D.G., *Construction de réseaux autotendants*. 1964: France. Patent No. 1.377.290.
14. Snelson, K., *Continuous tension, discontinuous compression structures*. 1965: United States. Patent No. 3169611.
15. Motro, R., *Tensegrity systems: the state of the art*. International Journal of Space Structures, 1992. **7**(2): p. 75-83.
16. Skelton, R.E. and de Oliveira, M.C., *Tensegrity systems*. 2009: Springer.
17. Pugh, A., *An introduction to tensegrity*. 1976: University of California Press.
18. Calladine, C., *Buckminster Fuller's "tensegrity" structures and Clerk Maxwell's rules for the construction of stiff frames*. International Journal of Solids and Structures, 1978. **14**(2): p. 161-172.
19. Tarnai, T., *Simultaneous static and kinematic indeterminacy of space trusses with cyclic symmetry*. International Journal of Solids and Structures, 1980. **16**(4): p. 347-359.
20. Pellegrino, S. and Calladine, C.R., *Matrix analysis of statically and kinematically indeterminate frameworks*. International Journal of Solids and Structures, 1986. **22**(4): p. 409-428.
21. Hanaor, A., *Prestressed pin-jointed structures—flexibility analysis and prestress design*. Computers & Structures, 1988. **28**(6): p. 757-769.
22. Williamson, D., Skelton, R.E., and Han, J., *Equilibrium conditions of a tensegrity structure*. International Journal of Solids and Structures, 2003. **40**(23): p. 6347-6367.

23. de Jager, B. and Skelton, R.E., *Stiffness of planar tensegrity truss topologies*. International Journal of Solids and Structures, 2006. **43**(5): p. 1308-1330.
24. Vassart, N., *Recherche de forme et stabilité des systèmes réticulés spatiaux autocontraints: application aux systèmes de tensegrité*. 1997, Université Montpellier II.
25. Djouadi, S., Motro, R., *et al.*, *Active control of tensegrity systems*. Journal of Aerospace Engineering, 1998. **11**(2): p. 37-44.
26. Murakami, H., *Static and dynamic analyses of tensegrity structures. Part II. Quasi-static analysis*. International Journal of Solids and Structures, 2001. **38**(20): p. 3615-3629.
27. Maxwell, J.C., *L. on the calculation of the equilibrium and stiffness of frames*. The London, Edinburgh, and Dublin Philosophical Magazine and Journal of Science, 1864. **27**(182): p. 294-299.
28. Calladine, C. and Pellegrino, S., *First-order infinitesimal mechanisms*. International Journal of Solids and Structures, 1991. **27**(4): p. 505-515.
29. Oppenheim, I.J. and Williams, W.O., *Geometric effects in an elastic tensegrity structure*. Journal of Elasticity, 2000. **59**: p. 51-65.
30. Guest, S., *The stiffness of prestressed frameworks: A unifying approach*. International Journal of Solids and Structures, 2006. **43**(3-4): p. 842-854.
31. Guest, S., *The stiffness of tensegrity structures*. IMA Journal of Applied Mathematics, 2011. **76**(1): p. 57-66.
32. Tibert, A.G. and Pellegrino, S., *Review of form-finding methods for tensegrity structures*. International Journal of Space Structures, 2003. **18**(4): p. 209-223.
33. Juan, S.H. and Mirats Tur, J.M., *Tensegrity frameworks: static analysis review*. Mechanism and Machine Theory, 2008. **43**(7): p. 859-881.
34. Connelly, R. and Terrell, M., *Globally rigid symmetric tensegrities*. Structural Topology, 1995. **21**.
35. Burkhardt, R., *The application of nonlinear programming to the design and validation of tensegrity structures with special attention to skew prisms*. Journal of the International Association for Shell and Spatial Structures, 2006. **47**(1): p. 3-15.
36. Pellegrino, S., *Mechanics of kinematically indeterminate structures*. 1986, University of Cambridge.
37. Vassart, N. and Motro, R., *Multiparametered formfinding method: application to tensegrity systems*. International Journal of Space Structures, 1999. **14**(2): p. 147-154.
38. Kenner, H., *Geodesic math and how to use it*. 1976: University of California Press.
39. Sultan, C., *Modeling, design, and control of tensegrity structures with applications*. 1999, Purdue University: West Lafayette.
40. Pagitz, M. and Mirats Tur, J.M., *Finite element based form-finding algorithm for tensegrity structures*. International Journal of Solids and Structures, 2009. **46**(17): p. 3235-3240.
41. Li, Y., Feng, X.-Q., *et al.*, *A Monte Carlo form-finding method for large scale regular and irregular tensegrity structures*. International Journal of Solids and Structures, 2010. **47**(14): p. 1888-1898.



42. Paul, C., Lipson, H., and Cuevas, F.J.V. *Evolutionary form-finding of tensegrity structures*. in *Proceedings of the 7th annual conference on Genetic and evolutionary computation*. 2005. ACM.
43. Koohestani, K., *Form-finding of tensegrity structures via genetic algorithm*. International Journal of Solids and Structures, 2012. **49**(5): p. 739-747.
44. de Jager, B. and Skelton, R.E., *Symbolic stiffness optimization of planar tensegrity structures*. Journal of Intelligent Material Systems and Structures, 2004. **15**(3): p. 181-193.
45. Masic, M., Skelton, R.E., and Gill, P.E., *Optimization of tensegrity structures*. International Journal of Solids and Structures, 2006. **43**(16): p. 4687-4703.
46. Motro, R., Najari, S., and Jouanna, P., *Static and dynamic analysis of tensegrity systems*, in *Shell and Spatial Structures: Computational Aspects*. 1987, Springer. p. 270-279.
47. Furuya, H., *Concept of deployable tensegrity structures in space applications*. International Journal of Space Structures, 1992. **7**(2): p. 143-151.
48. Murakami, H., *Static and dynamic analyses of tensegrity structures. Part 1. Nonlinear equations of motion*. International Journal of Solids and Structures, 2001. **38**(20): p. 3599-3613.
49. Oppenheim, I.J. and Williams, W.O., *Vibration and damping in three-bar tensegrity structure*. Journal of Aerospace Engineering, 2001. **14**(3): p. 85-91.
50. Oppenheim, I.J. and Williams, W.O., *Vibration of an elastic tensegrity structure*. European Journal of Mechanics – A/Solids, 2001. **20**(6): p. 1023-1031.
51. Sultan, C., Corless, M., and Skelton, R.E., *Linear dynamics of tensegrity structures*. Engineering Structures, 2002. **24**(6): p. 671-685.
52. Skelton, R.E., Pinaud, J.P., and Mingori, D., *Dynamics of the shell class of tensegrity structures*. Journal of the Franklin Institute, 2001. **338**(2): p. 255-320.
53. Skelton, R. *Dynamics of tensegrity systems: Compact forms*. in *45th IEEE Conference on Decision and Control*. 2006. San Diego, CA.
54. Arsenault, M. and Gosselin, C.M., *Kinematic, static, and dynamic analysis of a planar one-degree-of-freedom tensegrity mechanism*. Journal of Mechanical Design, 2005. **127**: p. 1152-1160.
55. Arsenault, M. and Gosselin, C.M., *Kinematic, static and dynamic analysis of a planar 2-DOF tensegrity mechanism*. Mechanism and Machine Theory, 2006. **41**(9): p. 1072-1089.
56. Arsenault, M. and Gosselin, C.M., *Kinematic, static, and dynamic analysis of a spatial three-degree-of-freedom tensegrity mechanism*. Journal of Mechanical Design, 2006. **128**: p. 1061-1069.
57. Sultan, C. and Skelton, R.E., *Integrated design of controllable tensegrity structures*. Adaptive structures and material systems, 1997. **54**: p. 27-35.
58. Chan, W.L., Arbelaez, D., *et al.* *Active vibration control of a three-stage tensegrity structure*. in *Smart Structures and Materials*. 2004. International Society for Optics and Photonics.
59. de Jager, B. and Skelton, R.E., *Input-output selection for planar tensegrity models*. IEEE Transactions on Control Systems Technology, 2005. **13**(5): p. 778-785.

60. Bel Hadj Ali, N. and Smith, I.F.C., *Dynamic behavior and vibration control of a tensegrity structure*. International Journal of Solids and Structures, 2010. **47**(9): p. 1285-1296.
61. Fest, E., Shea, K., and Smith, I.F.C., *Active tensegrity structure*. Journal of Structural Engineering, 2004. **130**(10): p. 1454-1465.
62. Adam, B. and Smith, I.F., *Tensegrity active control: Multiobjective approach*. Journal of Computing in Civil Engineering, 2007. **21**(1): p. 3-10.
63. Sultan, C. and Skelton, R.T. *Tendon control deployment of tensegrity structures*. in *5th Annual International Symposium on Smart Structures and Materials*. 1998. International Society for Optics and Photonics.
64. Knight, B., Duffy, J., et al. *Innovative deployable antenna developments using tensegrity design*. in *41st AIAA/ASME/ASCE/AHS/ASC Structures, Structural Dynamics, and Materials Conference and Exhibit, Atlanta, GA*. 2000.
65. Tibert, A. and Pellegrino, S., *Deployable tensegrity reflectors for small satellites*. Journal of Spacecraft and Rockets, 2002. **39**(5): p. 701-709.
66. Tibert, A.G. and Pellegrino, S. *Deployable tensegrity masts*. in *Proc. 44th AIAA/ASME/ASCE/AHS Structures, Structural Dynamics, and Materials Conference*. 2003. Norfolk, VA.
67. Moored, K.W. and Bart-Smith, H., *The analysis of tensegrity structures for the design of a morphing wing*. Journal of Applied Mechanics, 2006. **74**(4): p. 668-676.
68. Moored, K.W., Kemp, T.H., et al., *Analytical predictions, optimization, and design of a tensegrity-based artificial pectoral fin*. International Journal of Solids and Structures, 2011. **48**(22): p. 3142-3159.
69. Henrickson, J.V., Skelton, R.E., and Valasek, J. *Shape control of tensegrity airfoils*. in *AIAA Guidance, Navigation, and Control Conference*. 2016. San Diego, CA.
70. Aldrich, J.B. and Skelton, R.E. *Backlash-free motion control of robotic manipulators driven by tensegrity motor networks*. in *45th IEEE Conference on Decision and Control*. 2006. San Diego, CA.
71. Paul, C., Valero-Cuevas, F.J., and Lipson, H., *Design and control of tensegrity robots for locomotion*. IEEE Transactions on Robotics, 2006. **22**(5): p. 944-957.
72. Shibata, M., Saijyo, F., and Hirai, S. *Crawling by body deformation of tensegrity structure robots*. in *IEEE International Conference on Robotics and Automation*. 2009. Kobe, Japan.
73. Mirats-Tur, J.M. and Camps, J., *A three-DoF actuated robot*. IEEE Robotics & Automation Magazine, 2011. **18**(3): p. 96-103.
74. Caluwaerts, K., Despraz, J., et al., *Design and control of compliant tensegrity robots through simulation and hardware validation*. Journal of The Royal Society Interface, 2014. **11**(98).
75. Amendola, A., Hernández-Nava, E., et al., *On the additive manufacturing, post-tensioning and testing of bi-material tensegrity structures*. Composite Structures, 2015. **131**: p. 66-71.
76. Liu, K., Wu, J., et al., *Programmable deployment of tensegrity structures by stimulus-responsive polymers*. Scientific Reports, 2017. **7**(1): p. 3511.
77. Morgan, G.J., *Historical review: viruses, crystals and geodesic domes*. Trends in Biochemical Sciences, 2003. **28**(2): p. 86-90.

78. Ingber, D.E., *Cellular tensegrity: defining new rules of biological design that govern the cytoskeleton*. Journal of Cell Science, 1993. **104**: p. 613-627.
79. Levin, S.M., *The tensegrity-truss as a model for spine mechanics: biotensegrity*. Journal of Mechanics in Medicine and Biology, 2002. **2**(03n04): p. 375-388.
80. Ananthanarayanan, A., Azadi, M., and Kim, S., *Towards a bio-inspired leg design for high-speed running*. Bioinspiration & Biomimetics, 2012. **7**(4): p. 046005.
81. Ingber, D.E., *Tensegrity and mechanotransduction*. Journal of Bodywork and Movement Therapies, 2008. **12**(3): p. 198-200.
82. Liu, D., Wang, M., et al., *Tensegrity: construction of rigid DNA triangles with flexible four-arm DNA junctions*. Journal of the American Chemical Society, 2004. **126**(8): p. 2324-2325.
83. Zheng, J., Birktoft, J.J., et al., *From molecular to macroscopic via the rational design of a self-assembled 3D DNA crystal*. Nature, 2009. **461**(7260): p. 74-77.
84. Simmel, S.S., Nickels, P.C., and Liedl, T., *Wireframe and tensegrity DNA nanostructures*. Accounts of chemical research, 2014. **47**(6): p. 1691-1699.
85. Gibson, L.J. and Ashby, M.F., *Cellular solids: structure and properties*. 1999: Cambridge University Press.
86. Farzod, F. and Leamy, M.J., *Analysis of Bloch's method and the propagation technique in periodic structures*. Journal of Vibration and Acoustics, 2011. **133**(3): p. 031010.
87. Brillouin, L., *Wave propagation in periodic structures: electric filters and crystal lattices*. Second ed. 1953, New York: Dover Publications, Inc.
88. Vincent, J., *On the construction of a mechanical model to illustrate Helmholtz's theory of dispersion*. The London, Edinburgh, and Dublin Philosophical Magazine and Journal of Science, 1898. **46**(283): p. 557-563.
89. Pupin, M.I., *Wave transmission over non-uniform cables and long-distance air-lines*. Transactions of the American Institute of Electrical Engineers, 1900. **XVII**: p. 445-512.
90. Espenschied, L., *The electric wave filter*. IEEE Spectrum, 1966. **3**(8): p. 162.
91. Brittain, J.E., *The introduction of the loading coil: George A. Campbell and Michael I. Pupin*. Technology and Culture, 1970. **11**(1): p. 36-57.
92. Born, M. and von Karman, T., *Über Schwingungen in Raumgittern (On vibrations in space gratings)*. Physikalische Zeitschrift, 1912. **13**: p. 297-309.
93. Bloch, F., *Über die Quantenmechanik der Elektronen in Kristallgittern*. Zeitschrift für Physik, 1928. **52**(7): p. 555-600.
94. Wigner, E. and Seitz, F., *On the constitution of metallic sodium*. Physical Review, 1933. **43**(10): p. 804-810.
95. Cremer, L. and Leilich, H.O., *Zur Theorie der Biegekettenteiler (On theory of flexural periodic systems)*. Arch. Elektr. Uebertrag, 1953. **7**: p. 261-270.
96. Kittel, C., *Introduction to solid state physics*. Eighth ed. 2005: Wiley.
97. Miles, J.W., *Vibrations of beams on many supports*. Journal of the Engineering Mechanics Division, 1956. **82**(1): p. 1-9.
98. Lin, Y.K., *Free vibration of continuous skin-stringer panels*. Journal of Applied Mechanics, 1960. **27**(4): p. 669-676.
99. Lin, Y.-K. and McDaniel, T., *Dynamics of beam-type periodic structures*. Journal of Engineering for Industry, 1969. **91**(4): p. 1133-1141.

100. Heckl, M.A., *Investigations on the vibrations of grillages and other simple beam structures*. The Journal of the Acoustical Society of America, 1964. **36**(7): p. 1335-1343.
101. Mead, D.J., *Wave propagation in continuous periodic structures: research contributions from Southampton, 1964–1995*. Journal of Sound and Vibration, 1996. **190**(3): p. 495-524.
102. Sen Gupta, G., *Natural flexural waves and the normal modes of periodically-supported beams and plates*. Journal of Sound and Vibration, 1970. **13**(1): p. 89-101.
103. Sen Gupta, G., *Natural frequencies of periodic skin-stringer structures using a wave approach*. Journal of Sound and Vibration, 1971. **16**(4): p. 567-580.
104. Mead, D.J., *A general theory of harmonic wave propagation in linear periodic systems with multiple coupling*. Journal of Sound and Vibration, 1973. **27**(2): p. 235-260.
105. Orris, R.M. and Petyt, M., *A finite element study of harmonic wave propagation in periodic structures*. Journal of Sound and Vibration, 1974. **33**(2): p. 223-236.
106. Hodges, C., *Confinement of vibration by structural irregularity*. Journal of Sound and Vibration, 1982. **82**(3): p. 411-424.
107. Anderson, P.W., *Absence of diffusion in certain random lattices*. Physical Review, 1958. **109**(5): p. 1492-1505.
108. Hodges, C. and Woodhouse, J., *Vibration isolation from irregularity in a nearly periodic structure: theory and measurements*. The Journal of the Acoustical Society of America, 1983. **74**(3): p. 894-905.
109. Pierre, C., *Mode localization and eigenvalue loci veering phenomena in disordered structures*. Journal of Sound and Vibration, 1988. **126**(3): p. 485-502.
110. Cai, G. and Lin, Y., *Localization of wave propagation in disordered periodic structures*. AIAA Journal, 1991. **29**(3): p. 450-456.
111. Gei, M., *Wave propagation in quasiperiodic structures: stop/pass band distribution and prestress effects*. International Journal of Solids and Structures, 2010. **47**(22): p. 3067-3075.
112. Sigalas, M. and Economou, E., *Elastic and acoustic wave band structure*. Journal of Sound and Vibration, 1992. **158**(2): p. 377-382.
113. Kushwaha, M.S., Halevi, P., *et al.*, *Acoustic band structure of periodic elastic composites*. Physical Review Letters, 1993. **71**(13): p. 2022-2025.
114. Langley, R., *The response of two-dimensional periodic structures to point harmonic forcing*. Journal of Sound and Vibration, 1996. **197**(4): p. 447-469.
115. Ruzzene, M. and Baz, A., *Control of wave propagation in periodic composite rods using shape memory inserts*. Journal of Vibration and Acoustics, 2000. **122**(2): p. 151-159.
116. Thorp, O., Ruzzene, M., and Baz, A., *Attenuation and localization of wave propagation in rods with periodic shunted piezoelectric patches*. Smart Materials and Structures, 2001. **10**(5): p. 979-989.
117. Baz, A., *Active control of periodic structures*. Journal of Vibration and Acoustics, 2001. **123**(4): p. 472-479.
118. Ruzzene, M., Scarpa, F., and Soranna, F., *Wave beaming effects in two-dimensional cellular structures*. Smart Materials and Structures, 2003. **12**(3): p. 363-372.

119. Phani, A.S., Woodhouse, J., and Fleck, N., *Wave propagation in two-dimensional periodic lattices*. The Journal of the Acoustical Society of America, 2006. **119**: p. 1995-2005.
120. Spadoni, A., Ruzzene, M., *et al.*, *Phononic properties of hexagonal chiral lattices*. Wave Motion, 2009. **46**(7): p. 435-450.
121. Hutchinson, R. and Fleck, N., *The structural performance of the periodic truss*. Journal of the Mechanics and Physics of Solids, 2006. **54**(4): p. 756-782.
122. Hussein, M.I., *Theory of damped Bloch waves in elastic media*. Physical Review B, 2009. **80**(21): p. 212301.
123. Hussein, M.I. and Frazier, M.J., *Band structure of phononic crystals with general damping*. Journal of Applied Physics, 2010. **108**(9): p. 093506.
124. Farzbod, F. and Leamy, M.J., *The treatment of forces in Bloch analysis*. Journal of Sound and Vibration, 2009. **325**(3): p. 545-551.
125. Farzbod, F. and Leamy, M.J., *Analysis of Bloch's method in structures with energy dissipation*. Journal of Vibration and Acoustics, 2011. **133**(5): p. 051010.
126. Liu, Z., Zhang, X., *et al.*, *Locally resonant sonic materials*. Science, 2000. **289**(5485): p. 1734-1736.
127. Wang, G., Yu, D., *et al.*, *One-dimensional phononic crystals with locally resonant structures*. Physics Letters A, 2004. **327**(5-6): p. 512-521.
128. Yu, D., Liu, Y., *et al.*, *Flexural vibration band gaps in Euler-Bernoulli beams with locally resonant structures with two degrees of freedom*. Physical Review B, 2006. **73**(6): p. 064301.
129. Nouh, M., Aldraihem, O., and Baz, A., *Vibration characteristics of metamaterial beams with periodic local resonances*. Journal of Vibration and Acoustics, 2014. **136**(6): p. 061012.
130. Nouh, M., Aldraihem, O., and Baz, A., *Wave propagation in metamaterial plates with periodic local resonances*. Journal of Sound and Vibration, 2015. **341**: p. 53-73.
131. Pennec, Y., Djafari-Rouhani, B., *et al.*, *Low-frequency gaps in a phononic crystal constituted of cylindrical dots deposited on a thin homogeneous plate*. Physical Review B, 2008. **78**(10): p. 104105.
132. Wang, G., Wen, X., *et al.*, *Two-dimensional locally resonant phononic crystals with binary structures*. Physical review letters, 2004. **93**(15): p. 154302.
133. Sainidou, R., Djafari-Rouhani, B., *et al.*, *Locally resonant phononic crystals made of hollow spheres or cylinders*. Physical Review B, 2006. **73**(2): p. 024302.
134. Gonella, S., To, A.C., and Liu, W.K., *Interplay between phononic bandgaps and piezoelectric microstructures for energy harvesting*. Journal of the Mechanics and Physics of Solids, 2009. **57**(3): p. 621-633.
135. Liu, Z., Chan, C.T., and Sheng, P., *Three-component elastic wave band-gap material*. Physical Review B, 2002. **65**(16): p. 165116.
136. Liu, Z., Chan, C.T., and Sheng, P., *Analytic model of phononic crystals with local resonances*. Physical Review B, 2005. **71**(1): p. 014103.
137. Liu, L. and Hussein, M.I., *Wave motion in periodic flexural beams and characterization of the transition between Bragg scattering and local resonance*. Journal of Applied Mechanics, 2011. **79**(1): p. 011003.

138. Sigmund, O. and Jensen, J.S., *Systematic design of phononic band-gap materials and structures by topology optimization*. Philosophical Transactions of the Royal Society of London. Series A: Mathematical, Physical and Engineering Sciences, 2003. **361**(1806): p. 1001-1019.
139. Diaz, A.R., Haddow, A.G., and Ma, L., *Design of band-gap grid structures*. Structural and Multidisciplinary Optimization, 2005. **29**(6): p. 418-431.
140. Gazonas, G.A., Weile, D.S., *et al.*, *Genetic algorithm optimization of phononic bandgap structures*. International Journal of Solids and Structures, 2006. **43**(18–19): p. 5851-5866.
141. Hussein, M.I., Hamza, K., *et al.*, *Multiobjective evolutionary optimization of periodic layered materials for desired wave dispersion characteristics*. Structural and Multidisciplinary Optimization, 2006. **31**(1): p. 60-75.
142. Hussein, M.I., Hamza, K., *et al.*, *Optimal synthesis of 2D phononic crystals for broadband frequency isolation*. Waves in Random and Complex Media, 2007. **17**(4): p. 491-510.
143. Yang, W.-P. and Chen, L.-W., *The tunable acoustic band gaps of two-dimensional phononic crystals with a dielectric elastomer cylindrical actuator*. Smart materials and structures, 2008. **17**(1): p. 015011.
144. Robillard, J.-F., Matar, O.B., *et al.*, *Tunable magnetoelastic phononic crystals*. Applied Physics Letters, 2009. **95**(12): p. 124104.
145. Pichard, H., Richoux, O., and Groby, J.-P., *Experimental demonstrations in audible frequency range of band gap tunability and negative refraction in two-dimensional sonic crystal*. The Journal of the Acoustical Society of America, 2012. **132**(4): p. 2816-2822.
146. Bertoldi, K. and Boyce, M.C., *Mechanically triggered transformations of phononic band gaps in periodic elastomeric structures*. Physical Review B, 2008. **77**(5): p. 052105.
147. Casadei, F., Delpero, T., *et al.*, *Piezoelectric resonator arrays for tunable acoustic waveguides and metamaterials*. Journal of Applied Physics, 2012. **112**(6): p. 064902.
148. Nouh, M.A., Aldraihem, O.J., and Baz, A., *Periodic metamaterial plates with smart tunable local resonators*. Journal of Intelligent Material Systems and Structures, 2015.
149. Martinez-Sala, R., Sancho, J., *et al.*, *Sound attenuation by sculpture*. Nature, 1995. **378**(6554): p. 241-241.
150. Sánchez-Pérez, J.V., Caballero, D., *et al.*, *Sound attenuation by a two-dimensional array of rigid cylinders*. Physical Review Letters, 1998. **80**(24): p. 5325-5328.
151. Montero de Espinosa, F.R., Jiménez, E., and Torres, M., *Ultrasonic band gap in a periodic two-dimensional composite*. Physical Review Letters, 1998. **80**(6): p. 1208-1211.
152. Sigalas, M.M. and Economou, E.N., *Elastic waves in plates with periodically placed inclusions*. Journal of Applied Physics, 1994. **75**(6): p. 2845-2850.
153. Toyokatsu, M., *Sonic crystals and sonic wave-guides*. Measurement Science and Technology, 2005. **16**(5): p. R47-R63.
154. Richards, D. and Pines, D.J., *Passive reduction of gear mesh vibration using a periodic drive shaft*. Journal of Sound and Vibration, 2003. **264**(2): p. 317-342.

155. Hussein, M.I., Hulbert, G.M., and Scott, R.A., *Dispersive elastodynamics of 1D banded materials and structures: Design*. Journal of Sound and Vibration, 2007. **307**(3–5): p. 865-893.
156. Bao, J., Shi, Z., and Xiang, H., *Dynamic responses of a structure with periodic foundations*. Journal of Engineering Mechanics, 2012. **138**(7): p. 761-769.
157. Brun, M., Movchan, A.B., and Jones, I.S., *Phononic band gap systems in structural mechanics: finite slender elastic structures and infinite periodic waveguides*. Journal of Vibration and Acoustics, 2013. **135**(4): p. 041013.
158. Fang, N., Xi, D., *et al.*, *Ultrasonic metamaterials with negative modulus*. Nature materials, 2006. **5**(6): p. 452-456.
159. Yang, Z., Mei, J., *et al.*, *Membrane-type acoustic metamaterial with negative dynamic mass*. Physical review letters, 2008. **101**(20): p. 204301.
160. Baz, A.M., *An active acoustic metamaterial with tunable effective density*. Journal of Vibration and Acoustics, 2010. **132**(4): p. 041011.
161. Akl, W. and Baz, A., *Analysis and experimental demonstration of an active acoustic metamaterial cell*. Journal of Applied Physics, 2012. **111**(4): p. 044505.
162. Zhang, S., Xia, C., and Fang, N., *Broadband acoustic cloak for ultrasound waves*. Physical Review Letters, 2011. **106**(2): p. 024301.
163. Cervera, F., Sanchis, L., *et al.*, *Refractive acoustic devices for airborne sound*. Physical Review Letters, 2001. **88**(2): p. 023902.
164. Yang, S., Page, J., *et al.*, *Focusing of sound in a 3D phononic crystal*. Physical review letters, 2004. **93**(2): p. 024301.
165. Morvan, B., Tinel, A., *et al.*, *Experimental demonstration of the negative refraction of a transverse elastic wave in a two-dimensional solid phononic crystal*. Applied Physics Letters, 2010. **96**(10): p. 101905.
166. Ambati, M., Fang, N., *et al.*, *Surface resonant states and superlensing in acoustic metamaterials*. Physical Review B, 2007. **75**(19): p. 195447.
167. Li, J., Fok, L., *et al.*, *Experimental demonstration of an acoustic magnifying hyperlens*. Nature Materials, 2009. **8**(12): p. 931-934.
168. Spadoni, A., Daraio, C., and Freund, L.B., *Generation and control of sound bullets with a nonlinear acoustic lens*. Proceedings of the National Academy of Sciences of the United States of America, 2010. **107**(16): p. 7230-7234.
169. Olsson, R.H., III and El-Kady, I., *Microfabricated phononic crystal devices and applications*. Measurement Science and Technology, 2009. **20**(1): p. 012002.
170. Fuller, R.B., *Synergetics: explorations in the geometry of thinking*. 1975, New York: Pacific Tape Library.
171. Fuller, R.B., *Synergetics: explorations in the geometry of thinking*. Vol. 2. 1979, New York: Pacific Tape Library.
172. Milton, G.W. and Cherkaev, A.V., *Which elasticity tensors are realizable?* Journal of Engineering Materials and Technology, 1995. **117**(4): p. 483-493.
173. Kadic, M., Bückmann, T., *et al.*, *On the practicability of pentamode mechanical metamaterials*. Applied Physics Letters, 2012. **100**(19): p. 191901.
174. Schittny, R., Bückmann, T., *et al.*, *Elastic measurements on macroscopic three-dimensional pentamode metamaterials*. Applied Physics Letters, 2013. **103**(23): p. 231905.
175. Stratasys VeroWhitePlus - Polyjet technology material specifications.

176. Stratasys *PolyJet materials data sheet*.
177. Song, B.H. and Bolton, J.S., *A transfer-matrix approach for estimating the characteristic impedance and wave numbers of limp and rigid porous materials*. The Journal of the Acoustical Society of America, 2000. **107**(3): p. 1131-1152.
178. *Standard test method for normal incidence determination of porous material acoustical properties based on the transfer matrix method*, in ASTM E2611-17. 2017, ASTM International: West Conshohocken, PA.
179. Golla, D.F. and Hughes, P., *Dynamics of viscoelastic structures—a time-domain, finite element formulation*. ASME J. Appl. Mech, 1985. **52**(4): p. 897-906.
180. McTavish, D. and Hughes, P., *Modeling of linear viscoelastic space structures*. Journal of Vibration and Acoustics, 1993. **115**(1): p. 103-110.
181. Park, C.H., Inman, D.J., and Lam, M.J., *Model reduction of viscoelastic finite element models*. Journal of Sound and Vibration, 1999. **219**(4): p. 619-637.
182. Meirovitch, L., *Elements of vibration analysis*. 1986, Singapore: McGraw-Hill.
183. Martinsson, P.-G.J., *Fast multiscale methods for lattice equations*, in *Computational and Applied Mathematics*. 2002, The University of Texas at Austin.
184. Martinsson, P.-G. and Babuška, I., *Mechanics of materials with periodic truss or frame micro-structures*. Archive for rational mechanics and analysis, 2007. **185**(2): p. 201-234.
185. Martinsson, P.G. and Babuška, I., *Homogenization of materials with periodic truss or frame micro-structures*. Mathematical Models and Methods in Applied Sciences, 2007. **17**(05): p. 805-832.
186. Cook, R.D., *Concepts and applications of finite element analysis*. 2007: John Wiley & Sons.